AGU PUBLICATIONS

JGR

Journal of Geophysical Research: Solid Earth

RESEARCH ARTICLE
10.1002/2013JB010891

Key Points:
- Neogene tectonic model of the Bhutan Himalaya
- Neogene upper-crustal exhumation history of the Bhutan Himalaya
- Numerical modeling of low-temperature thermochronological data

Supporting Information:
- Readme
- Data Set S1
- Figure S1
- Figure S2
- Table S1
- Table S2

Correspondence to:
I. Coutand,
icoutand@dal.ca

Citation:
Coutand, I., D. M. Whipp Jr., D. Grujic, M. Bernet, M. G. Fellin, B. Bookhagen, K. R. Landry, S. K. Ghalley, and C. Duncan (2014), Geometry and kinematics of the Main Himalayan Thrust and Neogene crustal exhumation in the Bhutanese Himalaya derived from inversion of multithermochronologic data, *J. Geophys. Res. Solid Earth*, *119*, doi:10.1002/2013JB010891.

Received 2 DEC 2013
Accepted 24 JAN 2014
Accepted article online 3 FEB 2014

Geometry and kinematics of the Main Himalayan Thrust and Neogene crustal exhumation in the Bhutanese Himalaya derived from inversion of multithermochronologic data

Isabelle Coutand[1], David M. Whipp Jr.[2], Djordje Grujic[1], Matthias Bernet[3], Maria Giuditta Fellin[4], Bodo Bookhagen[5], Kyle R. Landry[1], S. K. Ghalley[6], and Chris Duncan[7]

[1]Department of Earth Sciences, Dalhousie University, Halifax, Nova Scotia, Canada, [2]Institute of Seismology, Department of Geosciences and Geography, University of Helsinki, Helsinki, Finland, [3]Institut des Sciences de la Terre, Université Joseph Fourier, Grenoble, France, [4]Institute for Geochemistry and Petrology, ETH Zürich, Zürich, Switzerland, [5]Department of Geography, University of California, Santa Barbara, California, USA, [6]Department of Geology and Mines, Ministry of Economic Affairs, Thimphu, Bhutan, [7]Department of Geosciences, University of Massachusetts Amherst, Amherst, Massachusetts, USA

Abstract Both climatic and tectonic processes affect bedrock erosion and exhumation in convergent orogens, but determining their respective influence is difficult. A requisite first step is to quantify long-term (~10^6 year) erosion rates within an orogen. In the Himalaya, past studies suggest long-term erosion rates varied in space and time along the range front, resulting in numerous tectonic models to explain the observed erosion rate distribution. Here, we invert a large data set of new and existing thermochronological ages to determine both long-term exhumation rates and the kinematics of Neogene tectonic activity in the eastern Himalaya in Bhutan. New data include 31 apatite and five zircon (U-Th)/He ages, and 49 apatite and 16 zircon fission-track ages along two north-south oriented transects across the orogen in western and eastern Bhutan. Data inversion was performed using a modified version of the 3-D thermokinematic model Pecube, with parameter ranges defined by available geochronologic, metamorphic, structural, and geophysical data. Among several important observations, our three main conclusions are as follows: (1) Thermochronologic ages do not spatially correlate with surface traces of major fault zones but appear to reflect the geometry of the underlying Main Himalayan Thrust; (2) our data are compatible with a strong tectonic influence, involving a variably dipping Main Himalayan Thrust geometry and steady state topography; and (3) erosion rates have remained constant in western Bhutan over the last ~10 Ma, while a significant decrease occurred at ~6 Ma in eastern Bhutan, which we partially attribute to convergence partitioning into uplift of the Shillong Plateau.

1. Introduction

The topography of convergent orogens results from the balance between tectonic processes accreting crustal material by thrust faulting and processes eroding rocks. It has been suggested that climate-induced erosion drives deformation along the Himalayan orogenic front [e.g., *Beaumont et al.*, 2001; *Grujic et al.*, 2002, 2006; *Hodges et al.*, 2004; *Thiede et al.*, 2004], but there is little consensus about the respective impact of tectonic and climate-related surface processes on the upper crustal exhumation of the orogenic wedge [e.g., *Burbank et al.*, 2003; *Reiners et al.*, 2003; *Whipple*, 2009]. A first step toward unraveling this problem is to carefully quantify long-term (~10^6 year) erosion rates along the orogen using low-temperature thermochronology data. Past studies yielded complex temporally and spatially variable results from the western [*Thiede et al.*, 2009], central [e.g., *Blythe et al.*, 2007; *Robert et al.*, 2009; *Streule et al.*, 2012; *Whipp et al.*, 2007], and eastern [*Grujic et al.*, 2006; *Long et al.*, 2012; *Adlakha et al.*, 2013; *Chirouze et al.*, 2013] parts of the Himalayan orogen. Furthermore, while some studies suggest Himalayan erosion rates have either accelerated [*Huntington et al.*, 2006; *Wobus et al.*, 2008] or decelerated [*Grujic et al.*, 2006; *Long et al.*, 2012] over the last 10 Ma, others advocate near-constant rates over the last 12 Ma [*Bernet et al.*, 2006; *Galy et al.*, 2010]. These dissimilar results suggest that Himalayan erosion likely varies in space and time along the strike of the range front.

To put these results into a tectonic framework, three distinct tectonic models prevail: (a) Out-of-sequence thrusting and possible reactivation of the Main Central Thrust, driven by climatically enhanced exhumation of the Himalayan front [e.g., *Hodges et al.*, 2004; *Thiede et al.*, 2005; *Wobus et al.*, 2003], (b) steady slip on the Main

Himalayan Thrust and growth of the Himalayan wedge via underplating and the development of a duplex at midcrustal depth [e.g., *Avouac*, 2003; *Bollinger et al*., 2006], and (c) crustal overthrusting on a laterally geometrically variable Main Himalayan Thrust [e.g., *Gansser*, 1964; *Robert et al*., 2009, 2011]. Discriminating between these tectonic models is critical to the understanding of Himalayan mountain building and can be only achieved through thermokinematic modeling of thermochronologic data [e.g., *Herman et al*., 2010; *Robert et al*., 2011].

In active convergent orogens, the upper crustal thermal field is strongly affected by thrusting on crustal-scale faults and by the resulting thermal advection [e.g., *Bollinger et al*., 2004; *Célérier et al*., 2009; *Herman et al*., 2010; *Whipp et al*., 2007]. Low-temperature thermochronologic data record cooling of rocks through the upper crust, from depths of up to ~10 km. Hence, they also record the perturbations of the subsurface thermal field and can thus be used to extract not only a record of rock exhumation, but also the geometry and slip rate on active major faults driving exhumation [e.g., *Ehlers*, 2005; *Robert et al*., 2011].

Originally named the Main Detachment Thrust by *Schelling and Arita* [1991], the Main Himalayan Thrust (MHT) is a crustal-scale detachment that marks the underthrusting of the Indian subcontinent beneath the Himalayan orogenic wedge. Major shear zones that have accommodated the Indo-Tibetan convergence branch off the MHT [*Makovsky et al*., 1996, 1999; *Nelson et al*., 1996; *Zhao et al*., 1993]. From the surface at the toe of the Himalayan range front down to midcrustal depths beneath the southern Tibetan Plateau, geophysical studies based on seismic reflection profiles (International Deep Profiling of Tibet and the Himalaya (INDEPTH)) [*Alsdorf et al*., 1998a, 1998b; *Hauck et al*., 1998; *Hirn et al*., 1984; *Makovsky et al*., 1996; *Nelson et al*., 1996; *Zhao et al*., 1993] and on receiver functions [*Acton et al*., 2011; *Caldwell et al*., 2013; *Nábělek et al*., 2009; *Schulte-Pelkum et al*., 2005] have imaged portions of the MHT in Garhwal, Eastern Nepal, Sikkim, and southern Tibet. Surface geological structures have also been used in balanced cross sections to infer the subsurface geometry of the basal detachment of the Himalayan fold-and-thrust belt from Pakistan in the west to Indian Arunachal Pradesh (India) in the east [*Bhattacharyya and Mitra*, 2009; *Coward and Butler*, 1985; *DeCelles et al*., 1998, 2001; *Long et al*., 2011a; *McQuarrie et al*., 2008; *Mitra et al*., 2010; *Schelling and Arita*, 1991; *Srivastava and Mitra*, 1994; *Tobgay et al*., 2012; *Yin et al*., 2010]. In addition, forward [*Adlakha et al*., 2013; *Bollinger et al*., 2006; *Célérier et al*., 2009; *Whipp et al*., 2007] and inverse [*Herman et al*., 2010; *Robert et al*., 2011] thermokinematic modeling of the crustal thermal field and low-temperature thermochronologic data have been used to constrain the late Miocene to present tectonic evolution of the Himalayan range as well as variations of the MHT geometry along strike from western (Garhwal) to eastern India (Arunashal Pradesh). In the eastern Himalaya, however, the MHT geometry derived from balanced cross sections and inversion of low-temperature thermochronometer data generally shows a poor fit to the geological and geophysical data; it also fails to both reproduce the distribution of low-temperature thermochronologic ages and to explain the exhumation of lower crustal material (from depths of ~70 km) as documented in NW Bhutan [*Grujic et al*., 2011] (Figures 1 and 2).

To address these questions, we focus our study on the Bhutanese Himalaya. A new multithermochronologic data set comprising 101 new apatite and zircon (U-Th)/He and fission-track cooling ages combined with published data sets by *Grujic et al*. [2006], *Long et al*. [2012], and *McQuarrie et al*. [2014] (Table S1 in the supporting information) are inverted using parameter ranges defined by available geochronologic, metamorphic, structural, and geophysical data. Data inversions are performed using a modified version of the 3-D thermokinematic model Pecube [*Braun*, 2003; *Braun et al*., 2012] that uses the neighborhood algorithm [*Rickwood and Sambridge*, 2006; *Sambridge*, 1999a, 1999b], allowing us to test an adequate tectonic model for Bhutan, define permissible geometry and kinematics of the MHT, constrain the overall thermal structure and properties of the middle-to-upper crust, and determine the rates and spatial distribution of upper crustal exhumation in the Bhutan Himalaya over the last 10 Ma.

2. Geologic Setting

The continuity of the principal lithotectonic units and structures along the 2500 km long range front [e.g., *Gansser*, 1964; *Hodges*, 2000] is a remarkable feature of the Himalaya, and in this respect Bhutan does not differ from the rest of the orogen. From north to south, major shear zones include (Figures 1 and 2) the South Tibetan Detachment System (STDS), the Main Central Thrust (MCT), the Main Boundary Thrust (MBT), and the Main Frontal Thrust (MFT) [e.g., *Hodges*, 2000; *Le Fort*, 1975], all but the last having been active during the Miocene.

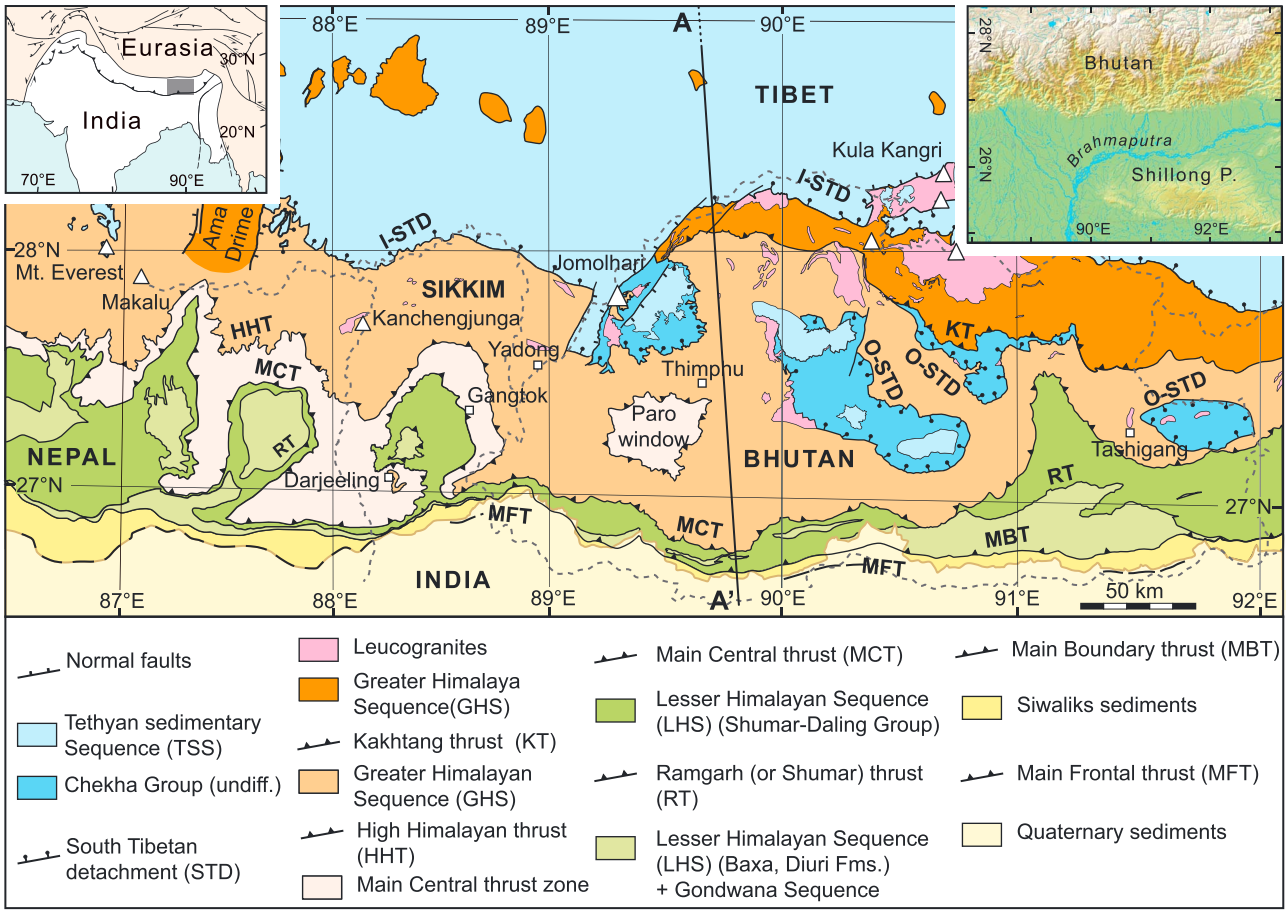

Figure 1. Geological map of the Eastern Himalaya [after *Grujic et al.*, 2011, and references therein]. Dark grey frame on map in inset shows location of Figure 1. Abbreviations are: MFT, Main Frontal Thrust; MBT, Main Boundary Thrust; RT, Ramgarh Thrust; MCT, Main Central Thrust; HHT, High Himalayan Thrust; KT, Kakhtang Thrust; O-STD, Outer South Tibetan Detachment; I-STD, Inner South Tibetan Detachment.

Respectively, these structures separate the very low-grade metamorphic Tethyan Sedimentary Sequence (TSS), the amphibolite to granulite/eclogite facies rocks of the Greater Himalayan Sequence (GHS), the greenschist facies rocks of the Lesser Himalaya Sequence (LHS), and the Mio-Pliocene synorogenic sub-Himalaya foreland sediments, which are thrust over the modern Ganges-Brahmaputra foreland basin along the active MFT. Aspects of the geology and geomorphology in the Bhutan Himalaya, however, suggest a unique tectonic history likely owing to its pre-Neogene tectonometamorphic and exhumation history [*Grujic et al.*, 1996, 2002, 2006; *Hollister and Grujic*, 2006; *Kellett et al.*, 2009; *Swapp and Hollister*, 1991; *Warren et al.*, 2011b]. In the sections below, we summarize the results of previous geological and geophysical studies that will serve as key constraints for the parameter range of the thermokinematic models. We emphasize that we are not intending to give a full account of the thermokinematic evolution of the Himalayan orogeny, but we focus on the Bhutanese part only.

2.1. Geology of Bhutan

2.1.1. The Tethyan Sedimentary Sequence (TSS) and the South Tibetan Detachment System (STDS)

The TSS in Bhutan comprises deformed sedimentary cover from the northern margin of the Indian Plate separated from the underlying high-grade metamorphic rocks of the GHS by the two structurally distinct segments of the STDS [*Burchfiel and Royden*, 1985; *Burg and Chen*, 1984; *Hollister and Grujic*, 2006]. The TSS is exposed between the Indus-Tsangpo suture and the trace of the STDS as well as in a string of klippen atop the GHS (Figures 1 and 2). Preserved at the base of klippen, the Outer South Tibetan Detachment shear zone (O-STD) [*Kellett et al.*, 2009] is characterized by top-down-to-the-north shearing with a strong component of vertical shortening and was active between circa 24–22 Ma and circa 16 Ma [*Chambers et al.*, 2011; *Corrie et al.*,

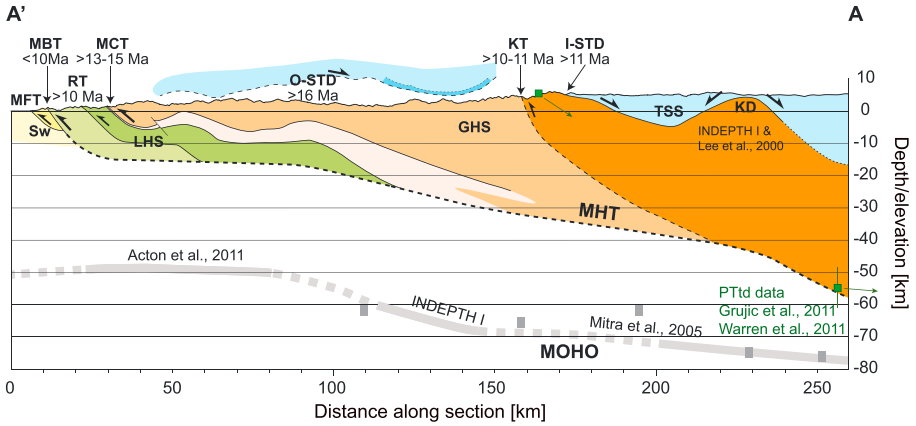

Figure 2. North-south geological cross section across western Bhutan (modified after *Grujic et al.* [2011]). For location, see Figure 1, line A-A'. Ages indicate the onset (<) or termination (>) of ductile shearing and brittle faulting on the main structures. The green squares indicate the outcrop location in northwestern Bhutan of granulitized eclogites and their estimated minimum burial depth at the time of peak pressure metamorphism in the late Miocene [*Grujic et al.*, 2011; *Warren et al.*, 2011b]. Abbreviations are as follows: KD, Kangmar dome; TSS, Tethyan Sedimentary Sequence; GHS, Greater Himalayan Sequence; LHS, Lesser Himalayan Sequence; Sw, Siwaliks sediments; MHT, Main Himalayan Thrust. Abbreviations of other structures are as in Figure 1.

2012; *Grujic et al.*, 2002; *Kellett et al.*, 2009, 2010; *Tobgay et al.*, 2012]. Straddling the Bhutan-Tibet border, the Inner South Tibetan Detachment (I-STD) was active until circa 11 Ma as a ductile shear zone [*Edwards et al.*, 1996, 1999; *Kellett et al.*, 2009; *Wu et al.*, 1998] and is crosscut by steep brittle normal and strike-slip faults of minor magnitude, which offset Quaternary moraines [*Meyer et al.*, 2006; *Wiesmayr et al.*, 2002].

2.1.2. The Greater Himalayan Sequence, Kakhtang Thrust (KT), and Main Central Thrust

In Bhutan, the Greater Himalayan Sequence (GHS) comprises amphibolite- to granulite-grade rocks including migmatitic orthogneisses and paragneisses and granulitized mafic eclogites [*Daniel et al.*, 2003; *Davidson et al.*, 1997; *Gansser*, 1983; *Grujic et al.*, 2002, 2011; *Swapp and Hollister*, 1991; *Warren et al.*, 2011b] that lie between the STDS and the MCT. The unit is characterized by widespread leucogranites with crystallization ages of circa 24–11 Ma [*Carosi et al.*, 2006; *Daniel et al.*, 2003; *Edwards and Harrison*, 1997; *Kellett et al.*, 2009] and is duplicated along the out-of-sequence Kakhtang Thrust (Figures 1 and 2) [*Davidson et al.*, 1997; *Edwards et al.*, 1996; *Gansser*, 1983; *Grujic et al.*, 2002], which cuts both penetrative ductile fabrics associated with the south directed shearing and metamorphic isograds [*Davidson et al.*, 1997]. The maximum age for KT's activation is circa 14–15 Ma [*Daniel et al.*, 2003; *Grujic et al.*, 2002, 2011], while thermochronological data indicate the two KT blocks experienced a common cooling history after circa 11–10 Ma [*Warren et al.*, 2011a]. The MCT (Figures 1 and 2) is a north dipping, top-to-the-south shear zone up to 2 km wide [*Grujic et al.*, 1996, 2002] containing a protolith boundary separating the LHS- and GHS-derived mylonites and protomylonites [*Davidson et al.*, 1997]. In Eastern and western Bhutan, (Figure 1), monazite and xenotime ages [*Daniel et al.*, 2003; *Tobgay et al.*, 2012] indicate that prograde metamorphism accompanied by partial melting and deformation was underway by circa 23 Ma and 20 Ma, respectively, and suggest that deformation related to the MCT lasted until at least 13 Ma.

2.1.3. The Lesser Himalayan Sequence, Main Boundary Thrust, and Main Frontal Thrust

The LHS contains metasediments deposited on the northern margin of the Indian Plate during Paleo-Proterozoic to Paleozoic [e.g., *Schelling and Arita*, 1991] and deformed during the Tertiary under greenschist facies conditions in a fold-and-thrust belt partly located underneath the southern parts of the GHS nappe and partly exposed at the toe of the modern range front (Figure 1) [*Gansser*, 1983; *Long et al.*, 2011a, 2011b; *McQuarrie et al.*, 2008]. The LHS is interpreted to comprise two superposed duplexes separated by the northward dipping Ramgarh (locally Shumar) Thrust (RT) (for details, see *Long et al.* [2011a]). In their structural and lithological differences, the two blocks separated by the RT correspond to the "Outer" and "Inner" LHS of the western Himalaya. In eastern Bhutan, the deformation of the outer LHS is interpreted to have occurred between 14.9 and 10.5 Ma and was completed when displacement along the Ramgarh Thrust stopped by circa 10.5 Ma [*Long et al.*, 2012]. In western Bhutan, duplexing of the outer LHS is interpreted to have developed between 12 and 9 Ma [*McQuarrie et al.*, 2014].

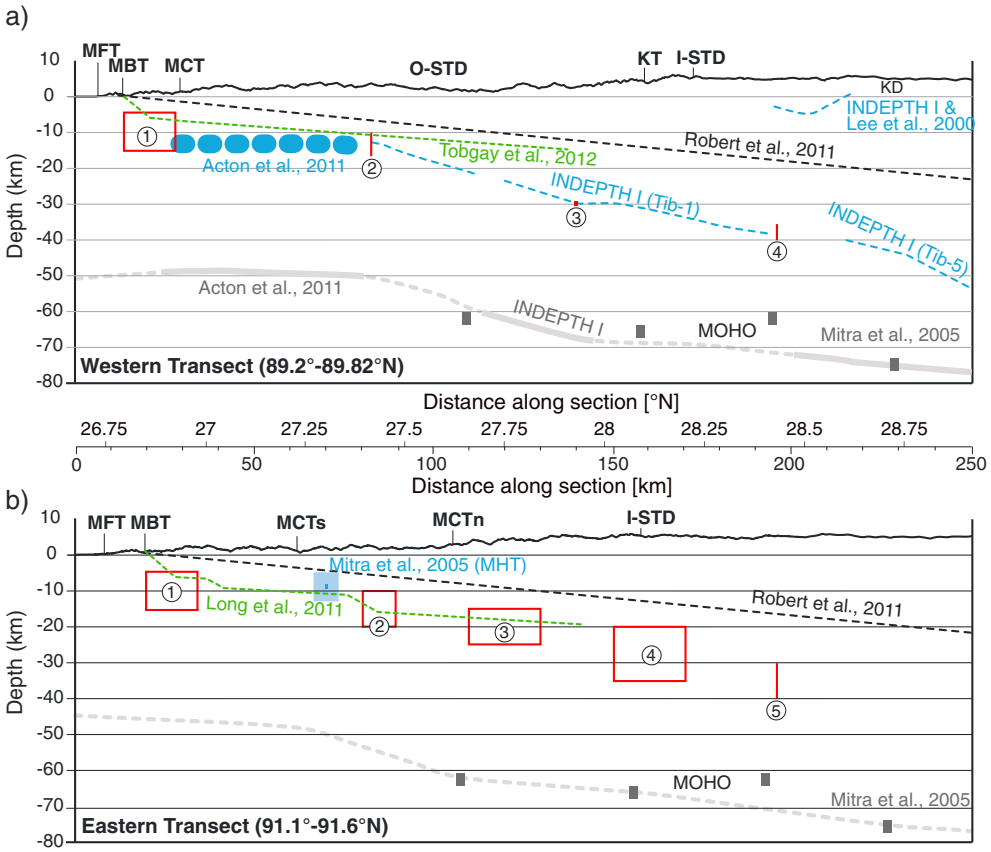

Figure 3. Geological and geophysical constraints on the Main Himalayan Thrust geometry for (a) western and (b) eastern Bhutan. Dashed lines in blue are from geophysical data from *Acton et al.* [2011], *Lee et al.* [2000], *Mitra et al.* [2005], and INDEPTH I; lines in green are from balanced cross sections from *Long et al.* [2011a] and *Tobgay et al.* [2012]; the line in black is from 3-D thermokinematic modeling [*Robert et al.*, 2011]. Red bars and boxes labeled 1 to 5 represent the geometric parameters that are free search parameters in our inversions. Abbreviations are as in Figures 1 and 2.

The MBT places the upper units of the LHS atop the Siwaliks Group (Figures 1 and 2) and the MFT forms the southern boundary of the Himalaya. The MBT in Bhutan appears to have been activated after cessation of the ductile shearing on the MCT, the KT, and the RT, about 10 Ma ago. The timing of activation of the MFT is poorly constrained; two detrital samples from the Siwaliks sediments yield discordant single grain-age apatite fission-track (AFT) distributions (Coutand, unpublished data, 2013), suggesting both the burial depth required to reset apatite fission tracks and the magnitude of erosion necessary to expose reset rocks were not reached.

2.2. Constraints on the Main Himalayan Thrust Geometry

Here we summarize the results of previous geophysical and structural studies on the geometry of the MHT along two transects across western and eastern Bhutan (Figure 3) that will serve as the key geometric constraints for the parameter range of the thermokinematic models. Previous inversion of the Bhutanese AFT data from [*Grujic et al.*, 2006] using thermokinematic modeling [*Robert et al.*, 2011] suggests the MHT is essentially planar extending from the surface trace of the MBT northward at a constant dip of 5–7° beneath all of the Bhutan Himalaya and southern Tibet, but several studies suggest that the MHT geometry is more complex.

2.2.1. Geometric Constraints Along the Western Transect (Figure 3a)

Projected receiver function data from Sikkim [*Acton et al.*, 2011] suggest the MHT is horizontal at a depth of ~10–15 km from 26.9°N to 27.45°N, where it starts to dip northward at 15–20°, connecting at 27.75°N with the MHT imaged at a depth of ~ 38 km on INDEPTH profile Tib-1 (For location of INDEPTH profiles, see *Hauck et al.* [1998, Figure 1]). Further north, below the Kangmar dome, the MHT is interpreted to dip northward at 35°–40° from ~42 to 45 km down to 70 km depth (Figure 3a) [*Hauck et al.*, 1998, profile Tib-5]. A balanced cross section at 89.55°E longitude suggests the MBT branches off the MHT at ~7 km depth and the MHT dips uniformly

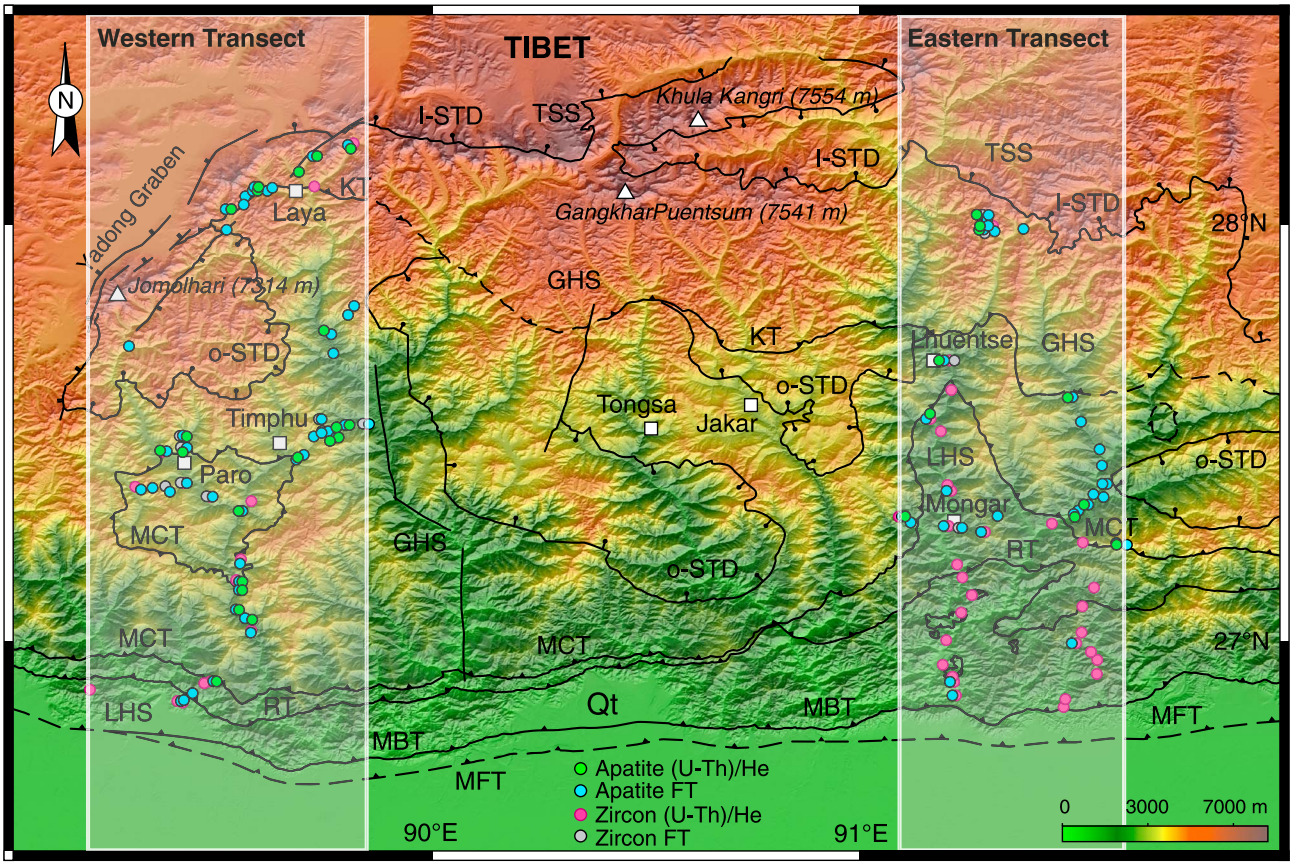

Figure 4. Digital Elevation Model with the main shear zones and tectonic units (modified after *Grujic et al*. [2006]) showing the location of both transects in shaded grey. The circles represent the distribution of in situ cooling ages used in the numerical models. Ages are from this study, *Grujic et al*. [2006], *Long et al*. [2012], *Tobgay et al*. [2012] and *McQuarrie et al*. [2014] (see Table S1 for details). Color coding: green, Apatite (U-Th)/He ages; blue, Apatite fission-track ages; pink, Zircon (U-Th)/He ages and grey, Zircon fission track ages.

northward at 4–5° until circa 28°N [*Tobgay et al*., 2012] (Figure 3a). Similarly, in the neighboring Darjeeling-Sikkim Himalaya at circa 88°20′E, the MHT is interpreted to dip 4° north (although separated in three flats and ramps) at a depth of 8–12 km beneath the Tista-Rangit double window [*Bhattacharyya and Mitra*, 2009].

2.2.2. Geometric Constraints Along the Eastern Bhutan (Figure 3b)

Data are sparse across eastern Bhutan, providing fewer constraints on the MHT geometry (Figure 3b) than for the western transect. Receiver function data [*Mitra et al*., 2005] at one site located between the MCT and the MBT in neighboring Arunachal Pradesh, about 90 km to the east of the study transect, suggest the MHT is at circa 8 km depth at 27.3°N (Figure 3b). Other geophysical data displayed by *Mitra et al*. [2005] along the same transect were projected along a same latitude (i.e., not along strike of the structures) from the INDEPTH stations previously described. Two balanced cross sections at the longitude of Tashigang and along the Kuru Chu Valley (Figure 1) suggest the MBT branches off the MHT at 6–7 km depth [*Long et al*., 2011a]. The MHT is marked by two ramps dipping northward at 30° separated by subhorizontal segments; north of 27.5°N, the MHT dips northward at a constant angle of about 3° (Figure 3b) [*Long et al*., 2011a].

2.2.3. Geometric Inconsistencies and Their Geologic Implications

Beyond the variable geometries obtained from these different methods (Figures 3a and 3b), some results simply do not reproduce important geologic observations. The details of the discrepancies themselves are beyond the scope of this paper. However, on the first order, previous results from the inversion of thermochronologic data [*Robert et al*., 2011] and, to a lesser extent, balanced cross sections, yield MHT depths that are far shallower than those interpreted from the INDEPTH data (Figure 3). This is important because these MHT depths and slopes are far too shallow (10–20 km below sea level beneath the surface trace of I-STD and slopes dipping to the north at 5–10°) to allow (1) isothermal decompression of widespread exposed GHS gneisses and migmatites from crustal depths of 37–45 km (average pressures at peak temperature of 10–12 kbar) to 22–15 km in the middle Miocene

(18–23 Ma ago) [*Chakungal*, 2006; *Corrie et al*., 2012; *Daniel et al*., 2003; *Davidson et al*., 1997], and (2) the exhumation of 15–14 Ma granutilized eclogites found in the hanging wall of the Kakhtang Thrust, exhumed from crustal depths of ~70 km to midcrustal levels (20–30 km) in ~2 Ma (see Figure 2, green square) [*Grujic et al*., 2011; *Warren et al*., 2011b]. In northern Bhutan, we therefore favor the MHT geometry imaged by geophysical data along the western transect because these data are in agreement with the tectonic, metamorphic, and geochronologic data presented in the previous sections. Further south, the geometry of the MHT between the traces of MBT and MCT as inferred by geophysical data in Sikkim [*Acton et al*., 2011] and by cross-section balancing in Darjeeling-Sikkim [*Bhattacharyya and Mitra*, 2009], western [*Tobgay et al*., 2012], and eastern Bhutan [*Long et al*., 2011a] are mutually compatible and in agreement with other geological data.

In summary, we base the geometric constraints and bounds for the search parameters of our thermokinematic models (Figures 3a and 3b, red boxes and bars) on geophysical data. For the eastern Bhutan, the lack of geophysical data requires a larger number of free geometric model parameters, and we used most constraints from geophysical data from the western transect.

3. Thermochronologic Data

3.1. Data Collection

We performed a formal inversion of a data set comprising four different low-temperature thermochronologic systems including apatite and zircon (U-Th)/He and fission-track analysis, subsequently referred to as AHe, ZHe, AFT, and ZFT, respectively. These thermochronometers were chosen due to their ability to record cooling and exhumation through the upper 5 to 10 km of the crust. Typical effective closure temperatures [e.g., *Reiners and Brandon*, 2006], which vary with chemical composition of the crystals, concentration of alpha radiation damage, grain size, and cooling rate among other factors, are 240 ± 30°C (ZFT) [e.g., *Bernet*, 2009; *Brandon et al*., 1998], 170 ± 20°C (ZHe) [e.g., *Reiners*, 2005], 120 ± 20°C (AFT) [e.g., *Donelick et al*., 2005; *Green et al*., 1985; *Ketcham et al*., 1999] and 60 ± 10°C (AHe) [e.g., *Farley and Stockli*, 2002; *Reiners and Brandon*, 2006; *Shuster et al*., 2006]. Details of the analytical techniques used for data acquisition are reported in the Data Set S1 (Appendices B to E).

Samples were collected along two north-south transects, oriented perpendicular to the strike of the main structures (i.e., subparallel to the dip-slip motion on the MHT), traversing both the LHS and the GHS in western (89.2–89.8°E and 26.5–28.5°N) and eastern (91.1–91.6°E and 26.5–28.5°N) Bhutan (Figure 4). Previously published data from *Grujic et al*. [2006], *Long et al*. [2012], and *McQuarrie et al*. [2014] located within the two transects are also included in the data inversion.

It is worth noting that the data reported in this study are restricted to samples north of the MBT (Figures 4 and 5). This choice is motivated by either the absence of datable outcrop south of the MBT along the western transect (Figure 4) or by the occurrence of unreset AFT ages from the Siwaliks in eastern Bhutan (Coutand, unpublished data, 2013). In the north, data are restricted to the footwall of the I-STD due to inaccessibility of the hanging wall. For details about the location of samples, see Table S1 and Figures 4 and 5.

3.2. Results

3.2.1. Apatite (U-Th)/He (Table 1)

Out of 39 samples that were processed for (U-Th)/He dating, seven samples yielded ages that were, within errors, older than the AFT ages for the corresponding samples, and one sample could not be dated due to low concentrations of uranium, thorium, and helium. Of the 31 datable samples displayed in Table 1, 21 are located along the western, and 10 along the eastern transects (Figures 4 and 5). The vast majority of the data are derived from the GHS, in part due to the poor quality of LHS apatite, limiting available inclusion- and crack-free euhedral crystals suitable for (U-Th)/He thermochronology. AHe ages range from 2.6 ± 0.3 Ma from sample BH287 located in northwestern Bhutan, north of Laya to 6.8 ± 0.6 Ma for sample BH101 located east of Mongar (Figure 4).

3.2.2. Apatite Fission Track (Table 2)

A total of 66 samples were collected and analyzed along both transects in leucogranites, gneisses, and migmatites from the GHS and four samples from granitic gneisses in the LHS (for samples location, see Table S1). Only 49 samples yielded results because of low sample quality due to low U concentrations, U zoning, cracks, inclusions or absence of apatite; only those samples are reported in this paper (Table 2). Between 7 and 30 grains were dated per sample, and all passed the χ^2 test indicating that the single-grain ages are consistent with a common age for each sample. The ages are between 2.2 ± 0.4 Ma and 6.9 ± 0.5 Ma (Table 2).

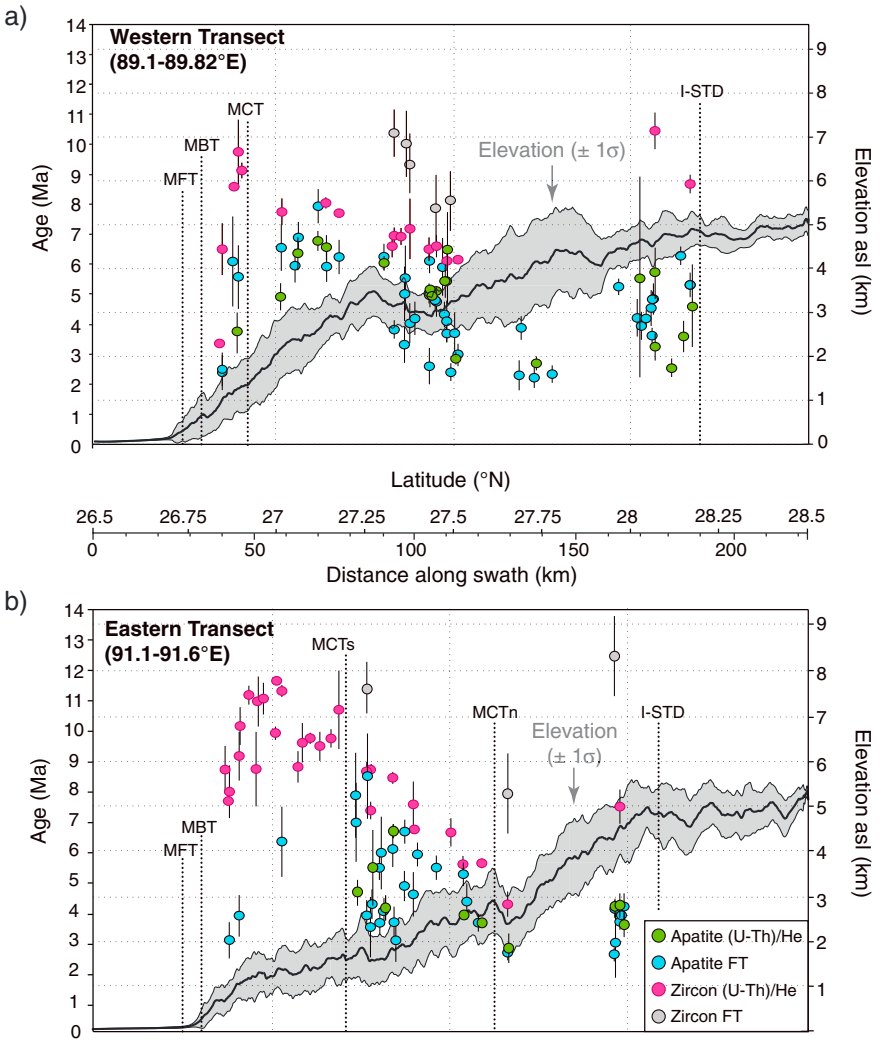

Figure 5. North-south distribution of cooling ages along (a) western and (b) eastern (b) Bhutan. Mean topographic profile for each transect is represented by the bold black line and minimum/maximum elevations by the thin black lines. The location of the main shear zones are represented by vertical dotted lines. Abbreviations are as in Figure 1. Color coding is as in Figure 4.

Due to their critical location along the western transect, their low uranium content and a different fission-track analyst, five samples (F01a, F04 to F07) taken from *Grujic et al.* [2006] were reprocessed to ensure reproducibility, reliable comparison with ages produced by this study, and to improve age accuracy by increasing the number of dated grains. These samples labeled BHF in Table 2 yielded ages similar to the original ages, within errors, except for F04/BHF04 and F07/BHF07 for which older ages were obtained (compare *Grujic et al.* [2006] and Table 2). To increase the data density along the transects, we added five ages from *Grujic et al.* [2006] and seven ages from *Long et al.* [2012] (Table S1).

3.2.3. Zircon (U-Th)/He (Table 3)

Five new samples were processed (Table 3) complementing preexisting data sets [*Long et al.*, 2012; *McQuarrie et al.*, 2014] (Table S2); one sample is located in northeastern Bhutan (BH357) and four (BH211, BH260, BH406, and BHF05) in western Bhutan (Tables S1 and 3). Four samples produced three excellent age replicates and yielded mean ages between 7.42 ± 0.55 Ma and 10.44 ± 0.61 Ma. However, only one aliquot was processed for BH406 yielding a single-grain age of 6.15 ± 0.08 Ma (Table 3). When merged with published data, these new ZHe ages display very well defined north-south trends for both western and eastern Bhutan (see Figure 5 and description in section 3.3).

Table 1. Apatite (U-Th)/He Data[a]

Samples	^{238}U (mol)	^{232}Th (mol)	^{147}Sm (mol)	^{4}He (mol)	Mean L (μm)	Mean R (μm)	Raw Age (Ma)	Ft	Corrected Age (Ma)	Age Error (%)	Mean Age (Ma)	Error (Ma)
BH101-1	3.61E-13	7.09E-14	5.09E-13	2.23E-15	184.4	72.28	4.53	0.81	5.62	3.41	6.8	0.6
BH101-4	7.07E-13	2.05E-13	7.33E-13	5.49E-15	235.1	65.78	5.61	0.8	7.02	3.17		
BH101-5	1.13E-12	3.72E-13	5.53E-13	9.28E-15	236.8	52.45	5.88	0.76	7.75	3.13		
BH163-1	1.54E-12	1.03E-13	3.65E-12	4.60E-15	293	60	2.25	0.79	2.85	2.03	5.7	0.8
BH163-2	9.75E-12	6.28E-13	1.75E-11	5.25E-14	342	102.5	4.07	0.87	4.69	1.81		
BH163-3	5.83E-12	4.49E-13	8.68E-12	4.85E-14	318	91.25	6.28	0.85	7.36	1.81		
BH163-4	1.08E-11	7.26E-13	1.24E-11	7.89E-14	362	101.25	5.56	0.87	6.41	1.8		
BH163-5	7.73E-12	5.21E-13	1.16E-11	6.18E-14	421	92.5	6.05	0.86	7.03	1.81		
BH409-1	1.77E-13	4.17E-14	6.35E-13	8.81E-16	157	48	3.6	0.73	4.94	3.18	5.4	0.6
BH409-2	3.14E-13	7.35E-14	1.16E-12	1.60E-15	224	55.25	3.68	0.77	4.8	2.58		
BH409-4	1.23E-12	4.55E-13	2.11E-12	8.94E-15	257	60.5	5.17	0.79	6.57	1.93		
BH689-1	3.35E-12	4.37E-13	6.58E-12	1.14E-14	277	78	2.54	0.83	3.06	1.7	3.2	0.4
BH689-2	2.44E-12	1.87E-13	3.54E-12	1.16E-14	335	74.75	3.59	0.83	4.34	1.9		
BH689-4	1.85E-12	1.85E-13	5.68E-12	6.78E-15	266	97	2.73	0.86	3.18	1.93		
BH689-5	1.37E-12	8.47E-14	5.77E-12	3.58E-15	356	90.25	1.95	0.85	2.28	2.09		
BH161-1	2.03E-12	1.56E-13	8.11E-12	2.01E-14	237	86.25	7.39	0.84	8.8	1.83	5.5	3.3
BH161-3	5.33E-12	6.71E-13	9.21E-12	1.32E-14	273	101.5	1.85	0.86	2.15	1.97		
BHF04-1	2.32E-14	2.90E-15	7.11E-14	5.88E-17	318	88.5	1.88	0.85	2.21	23.3	3.7	0.7
BHF04-3	1.21E-14	1.19E-15	8.53E-15	6.67E-17	260	72	4.17	0.82	5.1	19.1		
BHF04-4	3.91E-14	2.90E-15	6.50E-14	1.31E-16	239	107.25	2.54	0.86	2.93	11.78		
BHF04-5	1.63E-13	3.44E-14	2.99E-13	8.83E-16	306	87.25	3.97	0.85	4.69	3.16		
F09-1	1.63E-12	4.15E-13	5.01E-13	5.70E-15	374	94	2.56	0.86	2.98	2.01	2.9	0.2
F09-2	2.01E-12	9.94E-13	2.94E-13	7.89E-15	268	90.5	2.73	0.85	3.22	1.95		
F09-3	6.71E-13	6.34E-14	5.89E-13	1.95E-15	322	124.5	2.19	0.89	2.47	2.38		
F09-4	9.18E-13	2.37E-13	3.52E-13	2.01E-15	354	75.5	1.6	0.83	1.93	2.3		
F09-5	2.18E-12	6.02E-13	4.53E-13	4.58E-15	269	84.25	1.53	0.84	1.82	2		
02-102-F-1	2.51E-12	1.09E-13	3.79E-12	1.68E-14	307	82.75	5.1	0.84	6.07	1.85	6.0	0.3
02-102-F-3	1.22E-12	3.58E-14	1.95E-12	8.34E-15	230	64.5	5.22	0.8	6.55	1.93		
02-102-F-4	5.24E-13	1.62E-14	8.71E-13	2.65E-15	320	43.75	3.85	0.73	5.29	2.26		
02-102-F-5	5.93E-13	1.75E-14	7.57E-13	3.56E-15	226	48.25	4.59	0.74	6.19	2.13		
02-235-F-2	3.24E-13	6.20E-14	4.22E-13	1.07E-15	217	51	2.43	0.75	3.23	2.14	2.7	0.2
02-235-F-3	5.94E-13	8.34E-14	5.92E-13	1.92E-15	201	64	2.41	0.79	3.04	2.3		
02-235-F-4	2.31E-12	9.94E-14	8.00E-13	5.68E-15	208	71.75	1.88	0.81	2.32	1.97		
02-235-F-5	2.03E-12	9.20E-13	8.52E-13	5.20E-15	228	70.5	1.79	0.81	2.22	2		
02-104-F-1	9.74E-13	3.49E-13	2.97E-12	5.26E-15	215	68.5	3.81	0.8	4.74	1.9	6.5	1.2
02-104-F-3	2.75E-13	5.26E-14	1.08E-12	1.43E-15	248	90	3.78	0.85	4.47	2.59		
02-104-F-4	1.31E-12	4.69E-13	4.81E-12	1.49E-14	278	76.25	7.96	0.83	9.64	1.88		
02-104-F-5	7.10E-13	3.41E-13	4.22E-12	6.14E-15	222	79.75	5.87	0.83	7.11	1.96		
BH438-1	8.31E-13	3.22E-14	1.34E-12	5.32E-15	297	53.75	4.87	0.77	6.32	1.97	6.5	0.4
BH438-3	9.61E-13	9.46E-14	1.76E-12	7.83E-15	228	81.75	6.11	0.83	7.35	1.87		
BH438-5	2.84E-13	1.15E-14	5.14E-13	1.65E-15	156	50.75	4.42	0.74	5.96	2.38		
BH437-1	1.51E-12	6.78E-14	2.32E-12	1.15E-14	278	76.25	5.81	0.83	7.03	1.91	6.8	0.3
BH437-2	2.17E-12	9.37E-14	3.83E-12	1.53E-14	257	97	5.35	0.86	6.25	1.83		
BH437-3	2.24E-12	7.09E-14	3.65E-12	1.98E-14	324	85.25	6.74	0.85	7.97	1.82		
BH437-4	6.17E-12	2.25E-13	7.69E-12	4.44E-14	405	116	5.49	0.88	6.21	1.82		
BH437-5	2.18E-12	3.36E-14	5.77E-12	1.55E-14	340	89	5.41	0.85	6.34	1.88		
BH284-1	8.56E-12	1.65E-12	2.04E-12	2.71E-14	208	89.75	2.35	0.84	2.79	1.84	3.6	0.5
BH284-2	3.45E-11	4.43E-12	1.10E-11	2.13E-13	342	116	4.63	0.88	5.26	1.79		
BH284-3	1.98E-11	1.96E-12	5.24E-12	9.82E-14	293	118.25	3.75	0.88	4.26	1.81		
BH284-4	7.84E-12	9.47E-13	1.62E-12	1.96E-14	244	84.75	1.88	0.84	2.24	1.84		
BH284-5	9.44E-12	3.28E-13	3.03E-12	3.59E-14	315	77	2.92	0.83	3.51	1.84		
BH436-2	7.60E-13	2.08E-14	1.31E-12	4.39E-15	184	72	4.41	0.81	5.46	2	6.3	0.5
BH436-3	9.44E-13	7.99E-15	1.48E-12	7.01E-15	163	67	5.69	0.79	7.18	1.95		
BH211-3	3.83E-12	3.53E-13	8.28E-12	3.24E-14	336	103	6.33	0.87	7.29	1.84	4.6	1.3
BH211-4	3.04E-12	1.04E-13	6.27E-12	1.08E-14	306	97.75	2.7	0.86	3.13	1.89		
BH211-5	4.29E-12	7.44E-13	6.98E-12	1.69E-14	356	95.25	2.91	0.86	3.38	1.86		
BH39-3	4.76E-13	1.28E-14	4.41E-13	2.79E-15	244	98.75	4.49	0.86	5.24	2.15	5.4	0.1
BH39-5	2.63E-14	2.07E-15	1.92E-14	1.30E-16	132	40.25	3.75	0.68	5.49	7.69		
BH287-1	7.62E-12	3.43E-11	1.94E-12	5.36E-14	246	113.25	2.67	0.86	3.1	1.84	2.6	0.3
BH287-2	8.28E-12	5.25E-11	2.96E-13	7.02E-14	259	102	2.67	0.85	3.14	1.83		

Table 1. (continued)

Samples	^{238}U (mol)	^{232}Th (mol)	^{147}Sm (mol)	^{4}He (mol)	Mean L (μm)	Mean R (μm)	Raw Age (Ma)	Ft	Corrected Age (Ma)	Age Error (%)	Mean Age (Ma)	Error (Ma)
BH287-3	7.31E-12	4.24E-11	5.57E-13	4.11E-14	244	100.75	1.87	0.85	2.2	1.84		
BH287-4	4.03E-12	2.32E-11	2.47E-13	1.57E-14	228	93	1.3	0.84	1.55	1.88		
BH287-5	3.36E-12	3.34E-11	2.68E-13	3.52E-14	371	119.5	2.47	0.87	2.83	1.84		
BH417-1	1.03E-12	3.99E-14	1.26E-12	4.92E-15	174	72	3.66	0.81	4.54	2.01	5.0	0.4
BH417-2	1.99E-12	1.06E-13	2.25E-12	1.05E-14	230	80.75	4.01	0.83	4.82	1.91		
BH417-3	2.77E-12	6.00E-14	2.60E-12	1.37E-14	237	80	3.79	0.83	4.56	1.89		
BH417-4	1.37E-12	2.60E-14	1.59E-12	9.50E-15	183	74.5	5.3	0.81	6.52	1.93		
BH417-5	1.36E-12	3.74E-14	1.28E-12	6.03E-15	181	59.75	3.39	0.78	4.36	1.99		
F08-1	1.67E-12	4.00E-13	1.74E-12	1.25E-14	217	60.5	5.46	0.78	6.97	1.89	5.4	0.8
F08-3	5.06E-13	6.47E-14	1.27E-12	2.26E-15	230	59	3.33	0.78	4.26	2.19		
F08-5	3.27E-13	4.62E-14	7.97E-13	1.66E-15	215	47.25	3.75	0.74	5.1	2.34		
BH109b-1	6.61E-12	9.01E-13	6.64E-12	3.84E-14	418	109	4.35	0.88	4.95	1.89	5.1	0.1
BH109b-2	3.51E-12	3.85E-13	2.66E-12	1.99E-14	277	87	4.27	0.84	5.05	1.93		
BH109b-3	1.22E-12	1.56E-13	1.64E-12	6.35E-15	221	67.25	3.89	0.8	4.85	2.1		
BH109b-4	6.58E-12	5.69E-13	4.82E-12	4.16E-14	340	111.5	4.79	0.88	5.46	1.89		
BH109b-5	3.38E-12	2.33E-13	2.93E-12	2.08E-14	288	103.5	4.68	0.87	5.41	1.93		
BH111b-1	4.34E-13	3.34E-14	6.88E-13	2.28E-15	224	55.5	3.96	0.77	5.15	2.4	4.9	0.1
BH111b-2	7.80E-13	8.84E-14	8.96E-13	4.11E-15	340	66.25	3.95	0.81	4.88	2.19		
BH111b-3	6.48E-13	5.22E-14	1.01E-12	3.01E-15	333	58.25	3.5	0.79	4.45	2.33		
BH111b-4	8.98E-13	1.69E-13	7.74E-13	4.95E-15	250	58.25	4.07	0.78	5.22	2.02		
BH111b-5	4.33E-13	6.61E-14	4.56E-13	2.22E-15	213	56.5	3.81	0.77	4.95	2.25		
BH412-1	7.03E-13	6.43E-14	2.33E-12	3.54E-15	221	63.25	3.76	0.79	4.74	2.26	5.1	0.1
BH412-2	1.54E-12	1.62E-13	5.09E-12	8.91E-15	259	84.5	4.31	0.84	5.14	2.02		
BH412-3	3.36E-12	3.06E-13	8.49E-12	1.98E-14	362	93.5	4.41	0.86	5.14	1.92		
BH412-4	1.71E-12	1.69E-13	5.15E-12	1.07E-14	262	90.75	4.67	0.85	5.5	1.87		
BH412-5	1.71E-12	1.69E-13	4.91E-12	9.79E-15	259	83	4.27	0.84	5.1	1.94		
F5-3	9.72E-13	3.61E-14	1.32E-12	4.56E-15	235	67.75	3.58	0.81	4.44	2.05	4.9	0.5
F5-4	1.86E-12	4.50E-14	2.62E-12	1.10E-14	242	84.25	4.51	0.84	5.39	1.94		
BH352-1	1.23E-12	3.09E-13	1.11E-12	6.74E-15	265	88.75	4.00	0.85	4.74	2.08	4.3	0.2
BH352-2	1.25E-12	1.98E-13	1.64E-12	6.11E-15	347	95.75	3.64	0.86	4.23	2.13		
BH352-3	3.32E-12	8.44E-13	1.37E-12	1.83E-14	322	85.5	4.03	0.84	4.77	1.91		
BH352-4	4.16E-13	2.04E-13	6.45E-13	2.03E-15	277	69.5	3.38	0.81	4.16	1.48		
BH352-5	1.36E-12	2.50E-13	1.32E-12	5.47E-15	253	98.25	2.98	0.86	3.48	2.01		
BH357-1	4.80E-12	9.76E-13	3.47E-12	2.27E-14	269	58.75	3.49	0.78	4.46	1.87	4.4	0.4
BH357-2	2.37E-12	4.83E-13	2.31E-12	1.13E-14	201	62.5	3.51	0.79	4.46	1.91		
BH357-4	2.60E-12	2.51E-13	2.42E-12	9.25E-15	190	73	2.68	0.81	3.31	1.94		
BH357-5	2.00E-11	3.99E-12	1.58E-11	1.25E-13	387	116.25	4.62	0.88	5.23	1.85		
BH362-1	3.69E-13	4.43E-14	6.69E-13	1.08E-15	260	47.25	2.19	0.74	2.96	3.08	3.7	0.4
BH362-2	6.53E-13	1.23E-13	1.36E-12	2.91E-15	275	65	3.28	0.80	4.09	2.18		
BH362-3	2.45E-13	6.70E-14	5.88E-13	7.96E-16	282	52	2.34	0.76	3.08	3.94		
BH362-4	8.02E-13	1.60E-13	1.41E-12	4.09E-15	300	66	3.75	0.81	4.65	2.05		
BH378-1	6.60E-13	1.24E-13	2.05E-12	2.56E-15	219	52	2.84	0.76	3.75	2.27	2.9	0.5
BH378-2	2.12E-12	4.19E-13	4.22E-12	2.60E-15	326	62.75	0.90	0.80	1.13	2.31		
BH378-3	1.40E-12	3.29E-13	3.10E-12	4.84E-15	259	59.25	2.52	0.78	3.21	1.98		
BH378-4	2.65E-12	5.96E-13	5.24E-12	1.05E-14	264	65	2.88	0.80	3.59	1.92		
BH378-5	1.66E-12	3.93E-13	4.31E-12	5.43E-15	211	73.25	2.37	0.81	2.92	1.99		
BH60-1	1.02E-12	1.15E-12	1.03E-12	4.13E-15	415	74.25	2.48	0.83	3.00	2.02	5.5	1.1
BH60-2	5.80E-13	1.34E-12	1.07E-12	5.91E-15	266	79	5.12	0.82	6.21	1.97		
BH60-3	5.82E-13	4.55E-13	6.19E-13	6.02E-15	222	79.75	6.76	0.82	8.20	1.96		
BH60-4	4.02E-13	5.65E-14	2.73E-13	3.20E-15	244	62.75	5.94	0.79	7.49	2.08		
BH60-5	5.50E-13	3.88E-14	4.24E-13	1.65E-15	269	75	2.28	0.82	2.76	2.34		
BH70-1	3.68E-12	2.35E-13	3.25E-12	1.56E-14	199	85.25	3.22	0.83	3.86	1.89	3.7	0.1
BH70-2	3.45E-12	2.14E-13	2.99E-12	1.44E-14	217	72.75	3.18	0.81	3.91	1.89		
BH70-3	1.96E-12	1.28E-13	2.01E-12	7.24E-15	212	65	2.81	0.80	3.53	1.96		
BH70-4	6.55E-12	3.53E-13	7.67E-12	2.82E-14	275	104.5	3.28	0.87	3.79	1.86		
BH70-5	2.09E-12	9.25E-14	3.11E-12	7.49E-15	202	77.25	2.73	0.82	3.33	1.95		
BH53-2	1.43E-13	1.08E-14	1.43E-13	5.89E-16	166	58.25	3.13	0.77	4.07	3.41	4.8	0.4
BH53-4	3.14E-13	1.59E-14	8.24E-14	1.83E-15	230	73	4.46	0.82	5.46	2.34		
BH53-5	5.05E-14	5.35E-15	6.68E-14	2.36E-16	175	46	3.51	0.72	4.85	5.76		

Table 1. (continued)

Samples	^{238}U (mol)	^{232}Th (mol)	^{147}Sm (mol)	^{4}He (mol)	Mean L (μm)	Mean R (μm)	Raw Age (Ma)	Ft	Corrected Age (Ma)	Age Error (%)	Mean Age (Ma)	Error (Ma)
BH63-1	9.55E-13	2.53E-13	4.81E-12	5.30E-15	253	79.5	3.96	0.83	4.77	2.00	4.2	0.4
BH63-2	1.38E-12	3.08E-13	3.18E-12	7.59E-15	269	59.5	4.02	0.79	5.11	1.93		
BH63-3	6.65E-13	1.52E-13	2.29E-12	2.34E-15	206	57.5	2.55	0.77	3.30	2.17		
BH63-4	9.39E-13	2.12E-13	3.51E-12	3.47E-15	248	65.5	2.67	0.80	3.34	2.07		
BH63-5	1.27E-12	4.04E-13	3.23E-12	6.19E-15	226	60	3.48	0.78	4.45	1.96		

[a]Abbreviations: L, grain length; R, grain radius; Ft, alpha-ejection correction factor. Mean ages are the mean of each selected aliquot and the age error is the standard deviation between selected aliquots divided by the square root of the number of aliquots.

Table 2. Apatite Fission-Track Data[a]

Sample	*N*	$\rho_s \times 10^6$ cm^{-2} (Ns)	$\rho_i \times 10^6$ cm^{-2} (Ni)	$\rho_d \times 10^6$ cm^{-2} (Nd)	$P(\chi^2)$ (%)	Central Age ± 1σ (Ma)
BH38	25	0.0898 (214)	4.0739 (9706)	1.2744 (5807)	57.2	5.2 ± 0.4
BH63	14	0.0670 (83)	4.0375 (5002)	1.3144 (5807)	75.9	4.0 ± 0.4
BH161	15	0.0579 (48)	3.6991 (3067)	1.4508 (11881)	94.3	4.2 ± 0.6
BH163	19	0.2213 (388)	11.4142 (20015)	1.3444 (5807)	56.4	4.8 ± 0.3
BH164	8	0.1157 (75)	6.8730 (4454)	1.4364 (11881)	31.9	4.5 ± 0.6
BH211	20	0.0949 (179)	4.7029 (8874)	1.4221 (11881)	93.7	5.3 ± 0.4
BH284	18	0.3941 (498)	15.8585 (20040)	1.3643 (5807)	45.1	6.3 ± 0.3
BH339	17	0.063 (84)	4.5818 (6113)	1.4068 (5807)	96.7	3.6 ± 0.4
BH342	24	0.0282 (62)	1.862 (4099)	1.4162 (5807)	97.9	4.0 ± 0.5
BH351	7	0.0332 (7)	1.9531 (412)	0.9660 (10677)	88.7	3.0 ± 1.2
BH352	20	0.1198 (219)	5.3181 (9719)	0.97839 (10677)	99.7	4.1 ± 0.3
BH355	18	0.1349 (229)	6.4656 (10974)	0.99077 (10677)	31	3.8 ± 0.3
BH357	21	0.1731 (347)	8.0171 (16070)	1.00320 (10677)	80.1	4.0 ± 0.2
BH362	25	0.0435 (99)	1.8741 (4263)	1.01560 (10677)	88.2	4.2 ± 0.4
BH363	22	0.0663 (135)	4.9585 (10103)	1.02790 (10677)	91.9	2.5 ± 0.2
BH378	29	0.0497 (132)	3.5203 (9349)	1.05270 (10677)	91.5	2.7 ± 0.2
BH380	17	0.0715 (37)	1.6726 (865)	1.06510 (10677)	74.3	8.4 ± 1.4
BH406	30	0.0247 (69)	1.1817 (3306)	0.77583 (6663)	98.8	3.0 ± 0.4
BH408	20	0.0414 (70)	2.5327 (4279)	0.79265 (6663)	96.2	2.4 ± 0.3
BH409	23	0.0662 (107)	2.2690 (3668)	0.80105 (6663)	97.1	4.3 ± 0.4
BH411	24	0.0501 (96)	1.7316 (3316)	0.88660 (6663)	97.3	4.7 ± 0.5
BH412	30	0.0779 (215)	2.7995 (7726)	0.93027 (6663)	98.6	4.8 ± 0.3
BH413	26	0.0846 (175)	3.9973 (8265)	0.97386 (6663)	91.6	3.8 ± 0.3
BH415	26	0.0588 (126)	3.0031 (6437)	1.01750 (6663)	92.4	3.7 ± 0.3
BH416	23	0.0363 (39)	1.2073 (1298)	1.0610 (6663)	89.7	5.9 ± 1.0
BH417	20	0.1455 (265)	5.9251 (10788)	1.10460 (6663)	56.3	5.0 ± 0.3
BH424	19	0.0302 (38)	1.4720 (1853)	1.05980 (12962)	90.1	4.0 ± 0.7
BH426	30	0.0185 (27)	0.6668 (971)	1.07420 (10962)	95	5.5 ± 1.1
BH430	9	0.0420 (31)	2.5839 (1909)	1.10300 (12962)	99.8	3.3 ± 0.6
BH431	24	0.0228 (31)	0.9406 (1281)	1.1174 (12962)	99.7	5.0 ± 0.9
BH436	27	0.1069 (192)	3.3750 (6178)	1.1749 (12962)	75.6	6.9 ± 0.5
BH437	24	0.0927 (212)	3.0806 (7046)	1.4225 (5948)	99.7	7.9 ± 0.6
BH438	25	0.0872 (146)	3.8943 (6517)	1.4256 (5948)	95.2	5.9 ± 0.5
BH651	19	0.0620 (104)	3.8735 (6497)	1.3093 (11881)	90.2	3.9 ± 0.4
BH683	19	0.2331 (422)	10.4418 (18907)	1.2699 (11881)	42.6	5.2 ± 0.3
BH686	15	0.0963 (78)	5.6527 (4579)	1.2502 (11881)	85	3.9 ± 0.5
BH687	21	0.1859 (236)	10.1135 (12838)	1.2305 (11881)	99.5	4.2 ± 0.3
BH689	20	0.0992 (189)	5.9428 (11327)	1.1714 (11881)	62.6	3.6 ± 0.3
BH695	19	0.0897 (92)	4.5727 (4689)	1.3313 (6118)	90.5	4.8 ± 0.5
02-102 F	25	0.1363 (291)	4.6845 (10000)	1.1546 (5807)	12.2	6.2 ± 0.4
02-232 F	19	0.0435 (65)	4.2508 (6356)	1.2345 (5807)	99.1	2.3 ± 0.3
02-235 F	20	0.0380 (43)	3.9473 (4469)	1.2445 (5807)	99.5	2.2 ± 0.3
BHF01a	21	0.0362 (20)	3.6889 (2039)	1.3776 (6118)	52.8	2.5 ± 0.6
BHF01b	18	0.0403 (17)	4.1925 (1770)	1.3416 (6118)	93.1	2.4 ± 0.6
BHF02	11	0.0796 (17)	3.3260 (710)	1.3725 (6118)	90.7	6.1 ± 1.5
BHF04	21	0.0238 (29)	1.0903 (1330)	1.3828 (6118)	87.7	5.6 ± 1.0

Table 2. (continued)

Sample	N	$\rho_s \times 10^6\,cm^{-2}$ (Ns)	$\rho_i \times 10^6\,cm^{-2}$ (Ni)	$\rho_d \times 10^6\,cm^{-2}$ (Nd)	$P(\chi^2)$ (%)	Central Age ± 1σ (Ma)
BHF05	15	0.0671 (76)	2.5844 (2926)	1.3622 (6118)	82.2	6.5 ± 0.8
BHF06	20	0.0662 (118)	2.8713 (5117)	1.393 (6118)	75.1	5.9 ± 0.6
BHF07	20	0.1066 (127)	4.1771 (4976)	1.321 (6118)	96.7	6.2 ± 0.6

[a]Abbreviations: *N*, number of individual grains dated per sample; ρ_s, spontaneous track density; Ns, number of spontaneous tracks counted in the sample; ρ_i, induced track density in external detector (muscovite); Ni, number of induced tracks counted in external detector; ρ_d, induced track density in external detector adjacent to CN_5 dosimetry glass; Nd, number of induced tracks in external detector adjacent to dosimeter; and $P(\chi^2)$, chi-square probability.

3.2.4. Zircon Fission Track (Table 4)

Sixteen samples were processed for ZFT, 10 located along the Western profile (samples BH406 to 428) and six along the Eastern profile (samples BH352 to BH380), (Tables S1 and 4).

For the western transect samples, only 6 to 15 grains per sample were analyzed because of poor zircon quality (U zoning, fracturing, and inclusions), yielding ages between 7.9 ± 1.1 Ma and 13.5 ± 1.6 Ma (Table 4). Samples BH406, BH408, BH409, and BH415 were collected in the GHS, while the remaining samples were derived from the metasedimentary rocks of the Paro Formation in the Paro window [*Gansser*, 1983; *Tobgay et al*., 2012] (Figure 1). Four samples did not pass the χ^2 test, indicating that the single-grain ages are not consistent with a common age for those samples. The limited number of grains analyzed per sample does not permit clear identification of different age peaks; at least 20 grains per age peak would be needed [*Vermeesch*, 2004]. Because the pooled ages are within the 2σ error of the central ages of the samples that failed the χ^2 test, we report central ages for all samples (Table 4).

Along the eastern transect, 10 to 12 grains per samples were dated, and the samples yield ages ranging from 7.9 ± 1.3 Ma to 17.5 ± 0.7 Ma (Table 4). Again, the zircon quality was poor. Sample BH378 fails the χ^2 test. Samples BH355, BH357, and BH362, derived from the GHS, yield ages from 14.2 ± 0.7 Ma to 17.5 Ma. Consistent with the samples from the western transect, we report the central ages in Table 4. In our data inversion, we use only samples that passed the χ^2 test.

3.3. Age Pattern Along the Transects

Ages plotted against latitude show similar characteristic patterns in both profiles with, from south to north, ages increasing from the MBT to and across the MCT, then progressively decreasing with a minimum at about 27.75°N and increasing again in the footwall of the I-STD (Figure 5).

3.3.1. Western Transect

From south to north along the western transect, all four thermochronometer systems show similar age patterns, with ages generally increasing across the LHS, decreasing across most of the GHS and then again increasing again in the upper GHS near the I-STD. Between 89.1 and 89.82°E, traces of the MBT and the MCT are subparallel and separated by a horizontal distance that does not exceed 10–15 km (Figures 4 and 5a). In

Table 3. Zircon (U-Th)/He Results

Samples	He (pmol)	U (ng)	Th (ng)	Th/U	Raw Age (Ma)	Error Raw Age (± 1σ) (Ma)	Rs (μm)	Corrected Age (Ma)	Age Error (1σ) (%)	Mean Age (Ma)	Age Error (1σ) (Ma)
BHF05-1	0.0562	1.7038	0.3664	0.2206	5.8433	0.0810	42	8.15	1.39	7.74	0.44
BHF05-2	0.0444	1.5972	0.2334	0.1499	4.9980	0.0731	45	6.85	1.47		
BHF05-3	0.0964	2.8445	0.2948	0.1063	6.1599	0.0871	48	8.21	1.42		
BH406-1	0.6595	24.5990	7.0844	0.2954	4.6709	0.0625	51	6.15	1.34	6.15	0.08
BH357-1	0.9741	32.7154	5.7079	0.1790	5.3223	0.0883	72	6.44	1.66	7.42	0.55
BH357-2	0.7944	23.9443	5.0904	0.2181	5.8787	0.0978	58	7.46	1.67		
BH357-3	0.3955	10.9104	5.2102	0.4899	6.0599	0.0973	44	8.35	1.61		
BH260-1	0.8922	22.2489	2.8576	0.1318	7.2428	0.1263	57	9.21	1.75	10.44	0.61
BH260-2	2.0139	42.4225	2.1631	0.0523	8.7296	0.1298	57	11.09	1.49		
BH260-3	1.2907	26.3789	2.2422	0.0872	8.9255	0.1319	65	11.01	1.48		
BH211-1	1.9067	40.6037	15.9721	0.4035	7.9918	0.1112	112	9.02	1.39	8.67	0.31
BH211-2	2.9799	74.8896	15.0023	0.2055	7.0696	0.1033	104	8.05	1.46		
BH211-3	0.8307	17.9465	9.8991	0.5658	7.6152	0.0977	86	8.94	1.29		

Table 4. Zircon Fission-Track Results[a]

Sample	N	$\rho_s \times 10^5$ cm^{-2} (Ns)	$\rho_i \times 10^5$ cm^{-2} (Ni)	$\rho_d \times 10^6$ cm^{-2}	$P(\chi^2)$ (%)	Central Age ± 1σ (Ma)	U (ppm)	± 2σ
BH352	15	8.38 (206)	15.2 (373)	1.32	24.6	12.5 ± 1.3	172	19
BH355	15	73.6 (1856)	94.8 (2392)	1.32	94.2	17.5 ± 0.7	1078	60
BH357	15	39 (802)	61.6 (1268)	1.32	50.5	14.2 ± 0.7	703	47
BH362	12	52.1 (770)	73.7 (1089)	1.31	92.0	15.9 ± 0.8	843	60
BH378	10	12 (249)	34.1 (707)	1.31	0.0	7.9 ± 1.3	391	33
BH380	15	8.21 (299)	16.2 (592)	1.30	93	11.3 ± 0.9	187	17
BH406	7	29.0 (212)	57.5 (420)	1.26	1.7	10.6 ± 1.4	687	70
BH408	10	5.47 (108)	14.5 (286)	1.25	47.0	8.1 ± 1.0	174	21
BH409	15	32.4 (783)	60.3 (1457)	1.25	0.0	11.3 ± 0.9	726	44
BH411	15	10.2 (334)	25.8 (844)	1.24	0.1	8.1 ± 0.9	311	23
BH412	6	12.9 (89)	34.5 (238)	1.24	36.9	7.9 ± 1.1	418	56
BH413	15	12.6 (276)	26.0 (569)	1.24	58.9	10.3 ± 0.8	315	28
BH415	15	31.2 (661)	58.7 (1234)	1.23	1.2	11.2 ± 0.8	715	46
BH424	15	10.1 (229)	23.0 (521)	1.23	9.5	9.3 ± 1.0	281	26
BH426	10	13 (154)	27.1 (322)	1.22	39.3	10.0 ± 1.1	332	38
BH428	11	8.36 (138)	12.9 (213)	1.22	89.0	13.5 ± 1.6	158	22

[a]Abbreviations are the same as for Table 2.

this short distance, ZHe ages increase from 3.36 ± 0.05 Ma immediately north of the MBT to 9.74 ± 1.07 Ma south of the MCT (Figure 5a). One sample located in the hanging wall of the MCT is, within error, slightly younger at 7.74 ± 0.44 Ma, an age which slowly, steadily decreases northward reaching 6.15 ± 0.08 and 6.11 ± 0.33 Ma at about 27.5°N (Figure 5a). Finally, north of 28°N at higher elevations and closer to the I-STD, ages increase to 8.67 ± 0.31 and 10.44 ± 0.61 Ma (Figure 5a). Similarly, the southernmost AFT ages are young (2.4 to 2.5 ± 0.6 Ma), increase to 6.1 ± 1.5 Ma south of the MCT and, within errors, remain similar or slightly increase across and north of the MCT until approximately 27.25°N (Figure 5a). North of 27.25°N there is an abrupt decrease of AFT ages toward the north, reaching a minimum of 2.2 and 2.3 ± 0.3 Ma around 27.75°N (Figure 5a). North of 28°S, AFT ages become progressively older with a maximum of 6.3 ± 0.3 Ma in the footwall of the I-STD. AHe ages show more scatter and are often equal within error of the AFT ages, following the same north-south pattern (Figure 5a). Finally, the ZFT data between 27.3 and 27.5°N show a clear decreasing trend from 10.3 ± 0.8 Ma in the south to 8.1 ± 1.0 Ma in the north.

3.3.2. Eastern Transect

In spite of differences in the surface geology, the general age pattern along the eastern transect is similar to the western transect. ZHe data show an abrupt increase from 7.50 ± 0.13 to 11.60 ± 0.27 Ma in less than a 15 km horizontal distance between 26.9 and 27°N (Figure 5b). From that point, ZHe ages steadily decrease to 4.05 ± 0.07 just north of the MCTn at 27.65°N and finally increase to 7.42 ± 0.55 Ma at 28°N (Figure 5b). (U-Th)/He ages recently published by *Adams et al*. [2013] fill the gap north of 27.75°N and perfectly fit with these trends. However, these data were published too late to be included in our inversions.

AFT ages increase from 3.0 ± 0.6 north of the MBT to 8.4 ± 1.4 Ma immediately southeast of Mongar at 27.27°N (Figures 4 and 5b). Then, as observed in the west, AFT ages decrease northward to 2.7 ± 0.2 Ma at 27.66°N and increase again to 4.2 ± 0.4 Ma in the northernmost section of the transect (Figure 5b). AHe data are, within error, equal to their fission-track counterparts and follow the same trends. Finally, three ZFT ages between 27.27 and 27.97°N reflect the trends described for the other thermochronometers, with ages decreasing north of 27.25°N from 11.3 ± 0.9 to 7.9 ± 1.3 Ma at 27.66°N, then increasing to 12.5 ± 1.3 Ma at ~28°N (Figure 5b).

It is important to note that, except for ZHe data along the western transect, inflections in the double-curved characteristic age pattern do not spatially coincide with the surface trace of the MCT, suggesting that the pattern does not result from displacement on this structure (Figure 5). This is supported by previous studies suggesting that the end of activity of the MCT occurred by 15 Ma in western Bhutan [*Tobgay et al*., 2012] and 13 Ma in eastern Bhutan [*Chambers et al*., 2011; *Daniel et al*., 2003]. This is true both in the west, where the MCT occurs as a single structure, and in the east, where between 91.1 and 91.6°E, the surface trace of the MCT defines a pronounced reentrant due to the incision of the Kuru Chu Valley along the hinge of a N-S trending, north plunging antiform of the MCT and the GHS in its hanging wall (Figures 1 and 4), the "Kuru Chu Spur" of

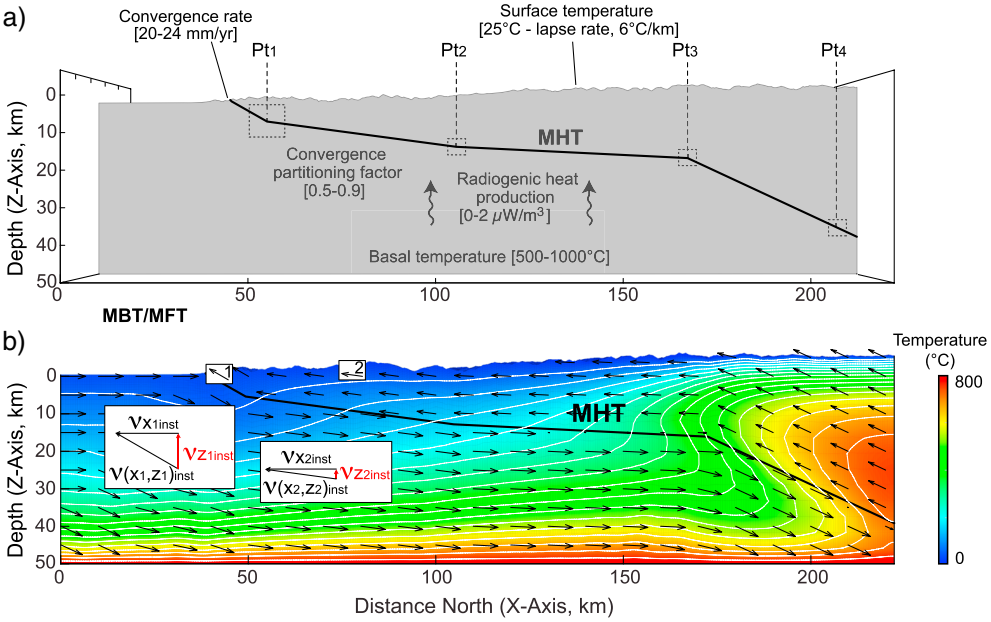

Figure 6. Thermokinematic model boundary conditions, free parameters, and example thermal solution (parameters are given in Table 5). (a) The kinematic model has Indo-Tibetan convergence partitioned on either side of the MHT, which is defined by a series of points along its length that may occupy any position within each corresponding search box. (b) Isotherms (thin white lines) show significant perturbations to the subsurface thermal field, mainly from advection using the velocity field (black arrows) generated by the kinematic model. Instantaneous exhumation rates in the numerical model correspond to the vertical component of the velocity vectors at the surface (insets).

Gansser [1983]. In that case, the MCT appears apparently twice along the age profile (Figure 5b), and we have labeled the southernmost and northernmost intersection of the MCT with the topography, MCTs and MCTn, respectively.

4. Thermokinematic Modeling

The large thermochronologic data set presented in the previous section can be used to extract information about fault slip rates, fault geometry, and thermal parameters in the surrounding crust. This procedure is not trivial, however, because thermochronologic ages are nonunique, and many combinations of kinematic, geometric, and thermal parameters are capable of producing equivalent ages within typical sample uncertainties. We address this challenge by using a numerical thermokinematic modeling approach to formally invert the data and define the parameter ranges that provide a satisfactory fit to the observations. The two-stage inversion procedure involves (1) a search through the multidimensional parameter space for parameter combinations that provide a good fit to the observed ages and (2) an appraisal of the search results to define acceptable parameter ranges. Predicted ages are calculated from 3-D forward models that use input parameters selected by the inversion search algorithm based on the goodness-of-fit of prior predictions. Below, we first detail the forward model before describing the inversion method.

4.1. Forward Model (Pecube) and Model Input Parameters

Thermochronometer cooling ages are predicted for comparison with observed ages by forward modeling of the 3-D crustal thermal field using a modified version of the software Pecube [*Braun*, 2003; *Braun et al*., 2012]. The functionality of Pecube is described well by *Braun* [2003] and *Braun et al*. [2012], so here we provide only a brief overview of the general operation of the code and indicate how the code was modified for this study. In essence, Pecube consists of three main components: (1) A kinematic model that calculates rock transport (advection) velocities as a function of defined fault geometries, (2) a thermal model that calculates the thermal field as a function of rock thermal properties, thermal boundary conditions, fault motion, and surface erosion, and (3) a set of age prediction algorithms that calculate thermochronometer ages from thermal histories recorded as particles cool during exhumation from depth to the model surface.

Table 5. Models Parameters[a]

Parameter Name	Parameter Range	Units	Parameter Symbol	Reference
	Material Properties			
Thermal conductivity	2.5	W/m/K	k	*Whipp et al.* [2007]
Specific heat capacity	800	J/kg/K	c	*Whipp et al.* [2007]
Crustal density	2750	kg/m^3	ρ_c	
Thermal diffusivity	35	km^2/My	α	
Volumetric radiogenic heat production	**0–2**	μW/m^3	H	
Radiogenic heat production	**0–30**	°C/Myr	A	
	Pecube Model Parameters			
Mean annual surface temperature in the foreland	25	°C	T_s	NOAA
Atmospheric lapse rate	6	°C/km	L	*Naito et al.* [2006]
Basal temperature	**500–1000**	°C	T_b	
India-Eurasia convergence rate	**20–24**	mm/yr	v_{conv}	*Banerjee et al.* [2008]
Hanging wall overthrusting	-	mm/yr	v_o	
Hanging wall underthrusting	-	mm/yr	v_u	
Convergence partitioning	**0.5–0.9**	n/a	λ	
Model time step	Optimal	years		
Horizontal node spacing	0.9	km		
Vertical node spacing (0–5 km)	0.9	km		
Vertical node spacing (5–15 km)	2.7	km		
Vertical node spacing (15–50 km)	8.1	km		
Model domain, western transect	62 × 220 × 50	km		
Model domain, eastern transect	60 × 220 × 50	km		
Fault geometry	**Variable**	km	(X_n, Z_n)	

[a]Mean annual surface temperature taken for Guwahati (Assam) located 55 m above sea level; NOAA, ftp://dossier.ogp.noaa.gov/GCOS/WMO-Normals/RA-II/IN/42410.TXT. Values in bold indicate free parameters.

Rock transport in the model is defined by a modified version of the fault model in Pecube, simulating overthrusting and underthrusting of rock on either side of the MHT in Bhutan. The geometry of the faults is determined by a series of input points; X, the horizontal distance with respect to the surface trace of the MBT and Z, the vertical distance (depth) with respect to sea level (Figure 6). For individual faults in Pecube, a spatially constant, but temporally variable slip velocity is associated with each planar fault dip segment, and segments are defined by depth-distance coordinate pairs [*Braun et al.*, 2012]. Where fault velocity fields overlap or diverge, velocities are averaged. We modified the Pecube fault model, similar to *Herman et al.* [2010], to utilize a single-model input convergence rate between India and Tibet, v_{conv}, and a partitioning factor, λ, that splits the convergence velocity into hanging wall overthrusting, $v_o = (1 - \lambda)v_{conv}$, and footwall underthrusting, $v_u = \lambda v_{conv}$ with respect to the position of the MHT (Table 5 and Figure 6).

Previous studies suggest Indo-Tibetan convergence rates in Bhutan may be slightly faster than elsewhere in the Himalaya, but the range of overthrusting rates is poorly constrained. Inversion of estimated Quaternary fault slip rates and modern interseismic geodetic velocities across the MFT/MHT yields convergence rates of 21.0 ± 0.2 mm/yr along the MFT from eastern Nepal to eastern Bhutan [*Lave and Avouac*, 2000; *Loveless and Meade*, 2011]. In Bhutan, convergence rates appear more rapid, with orogen-normal GPS velocity vectors showing velocities that are ~10 mm/yr faster than in the western Himalaya [*Banerjee et al.*, 2008], comparable to the difference suggested by plate reconstructions over the past ~11 Ma [*Molnar and Stock*, 2009]. If the Shillong Plateau region moves southward at 4–7 mm/yr, as suggested by the model of *Banerjee et al.* [2008], the residual convergence rate across the Bhutan Himalaya is 18–23 mm/yr, which, to a certain extent, compares with the rate of 17 mm/yr found by *Jade et al.* [2007]. Preliminary testing indicated that values < 20 mm/yr do not yield good fits to the data for any of our tectonic scenarios, so we use a convergence rate range of 20–24 mm/yr for inversion of the thermochronometer data. The factor controlling the partitioning of the convergence rate into overthrusting and underthrusting components, λ, has a range that is more difficult to define. This is, in part, because the partitioning depends on the combination of the convergence rate and the fault geometry. Previous studies from the central and eastern Himalaya suggest partitioning values of $\lambda \cong 0.75$, corresponding to overthrusting rates of 5–6 mm/yr [*Herman et al.*, 2010; *Robert et al.*, 2011; *Whipp et al.*, 2007]. For rocks in the GHS, for example, this overthrusting rate range would yield exhumation

Table 6. Inversion Results[a]

Transect Name	WB1	WB2	EB1	EB2
Number of models	20816	15414	24222	20424
Best misfit	0.65	0.63	0.43	0.43
Tb (°C)	**841** (**500**:**1000**)	840	840	840
A (°C/Myr)	**0.13** (**0**:**30**)	0.15	0.15	0.15
X_5 (km)	n/a	n/a	177	177
Z_5 (km)	n/a	n/a	**32.2** (**30**:**40**)	35
X_4 (km)	182	182	**142** (**130**:**150**)	**131** (**130**:**150**)
Z_4 (km)	**38.5** (**35**:**40**)	**37.5** (**35**:**40**)	**17.4** (**15**-**35**)	**25.7** (**15**:**35**)
X_3 (km)	126	126	**109** (**90**:**110**)	**93.1** (**90**:**110**)
Z_3 (km)	30	30	**15.9** (**10**:**25**)	**17.1** (**10**:**25**)
X_2 (km)	70	70	**51** (**50**:**70**)	**50.3** (**50**:**70**)
Z_2 (km)	**14.9** (**10**:**15**)	14.9	**11.3** (**10**:**20**)	**10.6** (**10**:**20**)
X_1 (km)	**5.1** (**0**:**15**)	**5.8** (**0**:**15**)	**5.6** (**0**:**15**)	**13.3** (**0**:**15**)
Z_1 (km)	**14.7** (**5**:**15**)	**14.8** (**5**:**15**)	**5.1** (**5**:**15**)	**11.2** (**5**:**15**)
Convergence rate (v_{conv}) (mm/yr)	**20.2** (**20**:**24**)	**23.4** (**20**:**24**)	**22.5** (**20**:**24**)	**22.7** (**20**:**24**)
Time step	1	2	1	2
Running time (Ma)	12-0	12-0	12-0	12-0
Transition time (Ma)	n/a	**4.3** (**7**:**2**)	n/a	**5.9** (**7**:**2**)
Partitioning 1 (λ_1)	**0.68** (**0.5**:**0.9**)	**0.69** (**0.5**:**0.9**)	**0.53** (**0.5**:**0.9**)	**0.56** (**0.5**:**0.9**)
Partitioning 2 (λ_2)	n/a	**0.73** (**0.5**:**0.9**)	n/a	**0.79** (**0.5**:**0.9**)

[a]Values in brackets indicate the investigated range of the free parameters, and the lowest misfit values for each parameter are indicated in bold.

rates of ~2–3 mm/yr, comparable to Late Tertiary exhumation rate estimates in the Bhutan Himalaya of ~1–2 mm/yr [*Grujic et al*., 2006]. Because our model geometry and the convergence rate are variables in the inversion, we have selected a broad range for the partitioning factor of $\lambda = 0.5 - 0.9$ (Table 5).

In our models, we treat the MBT and the MFT as a single structure located at the modern surface trace of the MBT, considering that the two are geographically close (0–6 km in horizontal distance as measured in the field) (Figure 1) and because reset thermochronologic data along both profiles are restricted to the north of the MBT suggesting the MFT has little contribution to the wedge exhumation since its activation.

For both transects, two tectonomorphic scenarios spanning the last 12 Ma are tested: (1) steady slip on the MHT and (2) two-stage slip on the MHT (Figure 6 and Table 6). We start our models at 12 Ma for two reasons: First, thermochronometer ages in our data are all younger than 12 Ma, recording cooling and exhumation after that time, and second, structural, metamorphic, and geochronological data indicate that prior to 11–15 Ma, the Himalayan range in Bhutan was hot and deformed ductily [*Grujic*, 2006; *Grujic et al*., 2002, 2006, 2011; *Hollister and Grujic*, 2006; *Warren et al*., 2011b]. Ductile deformation cannot currently be simulated using the fault model in Pecube.

Other than the MBT, we do not simulate other faults that sole into the MHT, as there is no evidence for significant activity between 0 and 12 Ma. Previous studies suggest that the MCT was no longer active by 15 Ma in western Bhutan [*Tobgay et al*., 2012] and 13 Ma in eastern Bhutan [*Chambers et al*., 2011; *Daniel et al*., 2003], which is further supported by the age patterns presented in the previous section. In addition, duplexing episodes in the outer LHS are interpreted to have been completed by 9 to 10.5 Ma in western [*McQuarrie et al*., 2014] and eastern [*Long et al*., 2012] Bhutan, respectively. Finally, displacements on the STDS, the KT, and the RT are not considered, because they were mostly inactive by 12 Ma (see section 2.1).

Temperatures within the 3-D crustal block are calculated by iterative solution of the 3-D advection-diffusion equation using the finite element method [*Braun*, 2003; *Braun et al*., 2012],

$$\rho c\left(\frac{\partial T}{\partial t} + v\nabla T\right) = k\nabla^2 T + H, \quad (1)$$

where ρ is density, c is heat capacity, T is temperature, t is time, v is the velocity field, k is thermal conductivity, and H is volumetric radiogenic heat production (for units and symbols, see Table 5). The input kinematic model parameters are used to calculate a steady state thermal solution at 12 Ma as the initial conditions for the subsequent transient thermal solution. As mentioned above, this initial solution not only simulates fault kinematics

for the approximate onset of activity on the MBT but also produces the first-order thermal influence of deformation and uplift of the Himalayan orogenic wedge above the subducting Indian Shield. The transient thermal field is calculated from 12 to 0 Ma subject to constant temperature boundary conditions at the base and free surface of the model (Table 5). A basal boundary temperature of 500–1000°C is applied at 50 km depth below sea level, corresponding to an average crustal geothermal gradient of 10–20°C/km. Tests performed with a much larger model thickness of 130 km and corresponding increase in model basal temperature (1200–1500°C) show no significant differences in the predicted cooling ages, so we have chosen to use a thinner model design with a higher horizontal finite element mesh resolution. At the model surface, temperature decreases with elevation from 25°C in the foreland (NOAA data for the town of Guwahati, ftp://dossier.ogp.noaa.gov/GCOS/WMO-Normals/RA-II/IN/42410.TXT) following an atmospheric lapse rate of 6°C/km [*Naito et al.*, 2006]. Steady state model topography is down sampled to ~0.5–1 km resolution from a Shuttle Radar Topography Mission [*Farr et al.*, 2007] 90 m digital elevation model of Bhutan. The extent of the model topography is minimized but large enough to ensure the zero-flux lateral boundaries of the model do not influence the predicted cooling ages. For example, the northernmost sample locations are ~40 and ~60 km from the northern margin of the model for the Western and Eastern transects, respectively. Typical crustal values are used for rock thermal properties in the model (Table 5) (see also *Ehlers* [2005]), but we invert for the crustal average radiogenic heat production in the range 0–2 $\mu W/m^3$. For simplicity, we do not consider the potential thermal influence of groundwater flow or fault shear heating on the crustal thermal field. The current version of Pecube does not include an option for groundwater flow, and modifying the code to include this effect is well beyond the scope of this study. Furthermore, since fault geometry and kinematics have a much larger influence on the thermal field than shear heating [*Whipp et al.*, 2007] we have opted not to consider its influence in order to minimize the free parameter space. See Table 5 for a complete list of model input parameters.

Lastly, cooling ages are predicted using the thermochronometer age prediction algorithms available in Pecube [e.g., *Braun*, 2003; *Braun et al.*, 2012], but faults in the model are kinematically translated to simulate lateral advection of the model topography [e.g., *Herman et al.*, 2007; *Whipp et al.*, 2009]. Lateral advection of the model topography provides near-vertical exhumation pathways for the bedrock sample locations in the model, which prevents potential problems arising from the use of steady state topography and rock transport trajectories above fault segments with shallow dip (<20°) (see Data Set S1, Appendix F for additional discussion).

4.2. Inversion Algorithm: Neighborhood Algorithm (NA)

We use the neighborhood algorithm [*Rickwood and Sambridge*, 2006; *Sambridge*, 1999a, 1999b] with the forward model Pecube [*Braun*, 2003; *Braun et al.*, 2012] to perform a formal inversion of the thermochronometer data presented in section 3. The goal of the inversion is to place bounds on allowable geometries and slip rate of the MHT and thermal properties in the crust. Because we follow the procedure used by a number of previous studies [*Braun and Robert*, 2005; *Campani et al.*, 2010; *Herman et al.*, 2010; *Robert et al.*, 2011; *Valla et al.*, 2010], below we provide only a brief overview of the two stages of the inversion.

The first stage of the neighborhood algorithm is designed to search through the multidimensional parameter space and find parameter combinations that minimize the misfit between observed and predicted data [*Sambridge*, 1999a]. To start, a set of input values are randomly selected within the parameter space and forward models are run with those parameters, generating a misfit value for each parameter combination. For our use of Pecube, this misfit value reflects the goodness-of-fit between our observed thermochronometer dataset and a set of predicted cooling ages based on the input parameter combination in Pecube. Mathematically, the misfit function, Φ, used in Pecube is,

$$\Phi = \frac{1}{n}\sqrt{\sum_{i=1}^{n}\frac{(\mathrm{PredAge}_i - \mathrm{ObsAge}_i)^2}{\sigma_i^2}} \tag{2}$$

where n is the number of thermochronometer ages, PredAge is the age predicted by Pecube, ObsAge is the observed age, and σ is the 1 sigma uncertainty in the observed age. After generating misfit values for the initial set of points, the parameter space is divided into a set of Voronoi cells [*Sambridge*, 1999a], which comprise the nearest neighborhood about each point in the parameter space. Misfit values for each point are assigned to the surrounding Voronoi cell, and input values for subsequent forward models are selected within a subset of Voronoi cells containing the points with the lowest misfit values, thereby guiding the search to regions with the best fit to the data. This process was traditionally done iteratively [*Sambridge*, 1999a], but we use

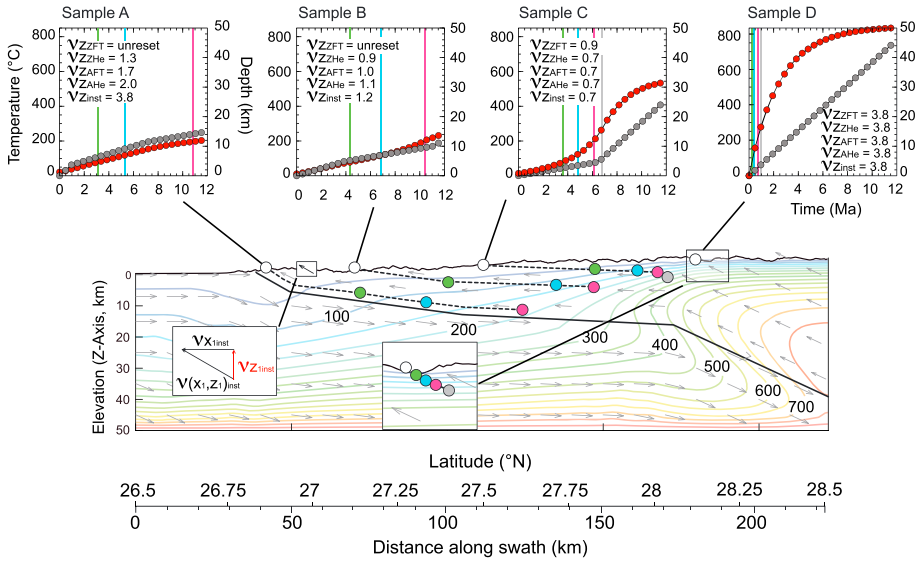

Figure 7. Cooling and exhumation of four rock samples (A, B, C, and D) now exposed at the surface (white dots) in the hanging wall of an active structure (black bold line) with variable dip angle. Light grey arrows represent the velocity field and light colored lines are isotherms. Black dashed lines indicate the exhumation pathway to the surface and the coloured dots represent the position at which the exhumation pathway crosses the effective closure temperature isotherm for the AHe (green), AFT (blue), ZHe (pink), and ZFT (grey) thermochronometers. The four plots above the cross section show cooling (red dots) and exhumation (grey dots) curves for samples A, B, C, and D between 12 and 0 Ma. The colored lines indicate the time at which the samples passed through their respective effective closure temperature isotherms with same color coding as for the dots. Long-term and instantaneous exhumation rates (υz) are reported for each thermochronometer and sample location in mm/yr.

a modified version of the neighborhood algorithm that continually samples the best Voronoi cells containing the models with the lowest misfit for each new forward model [*Rickwood and Sambridge*, 2006]. For our inversions, we resample 90% of the previous Voronoi cells and typically converge on a good fit ($\Phi < 1$) to the observed thermochronometer data in less than ~20,000 forward models.

Once the parameter search stage is finished, the complete set of forward model results is resampled in the appraisal stage to place statistical bounds on the parameter ranges that provide a satisfactory fit to the data. Appraisal of the suite of forward model misfits is done using Bayesian inference [*Sambridge*, 1999b]. This stage of the neighborhood algorithm produces posterior probability density functions (PPDFs) for each model parameter, in our case, using the likelihood function below,

$$L = \exp\left(-\frac{n}{2}\sqrt{\Sigma_{i=1}^{n}\frac{(\mathrm{PredAge}_i - \mathrm{ObsAge}_i)^2}{\sigma_i^2}}\right) \quad (3)$$

Output from this stage of the neighborhood algorithm calculation will be presented in the results in the form of 1-D and 2-D PPDFs for the inversion parameters.

4.3. Interpretation of Cooling and Long-Term Exhumation Rates

Our thermokinematic models involve continuous slip on a single structure (MHT) with steady state topography, and exhumation rates in the model orogen that are a function of the time over which they are calculated. Instantaneous exhumation rates (υz_{inst}) in thermokinematic models are equal to the vertical component of the velocity vectors at the model surface. In contrast, longer-term exhumation rates calculated for a given thermochronometer ($\upsilon z_{thermochronometer}$), correspond to the depth (with respect to the surface) of a sample at the time equal to its apparent cooling age divided by its apparent cooling age (Figure 7). Clearly, this depth will depend on both, the subsurface thermal field and the particle pathway to the surface. For samples with multiple thermochronologic measurements, the long-term exhumation rate will represent the increment of the integrated exhumation history recorded over the sample age (Figure 7). Thus, the long-term and instantaneous exhumation rates may not be equal, especially in areas where some fault segments have

shallow dip angles or samples are exhumed above multiple fault dip segments. For example, in a situation where exhumation recorded by a given thermochronometer occurred while the sample was being transported above a fault of uniform dip angle, the instantaneous and long-term exhumation rates may be equal (e.g., Figure 7, sample D). Where this is not true, the instantaneous and long-term exhumation rates are likely different (e.g., Figure 7, samples A–C), with important implications for the interpretation of those samples, as discussed below.

As emphasized by previous studies [e.g., *Batt and Brandon*, 2002; *Ehlers*, 2005; *Stüwe and Hintermüller*, 2000], lateral or horizontal particle displacement is critical for data interpretation. Samples may have traveled tens of kilometers horizontally but little vertically between cooling below their effective closure temperature isotherm and reaching the surface (Figure 7). As a result, the use of simpler 1-D modeling techniques that assume vertical exhumation only may yield erroneous long-term exhumation rates that are spatially offset. Furthermore, it is often assumed in low-temperature thermochronology that cooling relates to upper crustal exhumation. This may be true in some tectonic settings, but in a shallowly dipping fold-thrust belt, this assumption is unlikely to be true, as cooling and exhumation curves may be decoupled even in the shallowest portions of the crust (Figure 7).

We note that it may be difficult to compare our thermokinematic results with equivalent studies in the Himalaya because (1) previous thermokinematic modeling-based studies used different fault models, data sets, tectonomorphic scenarios, software, and analytical solutions [*Adlakha et al*., 2013; *Bollinger et al*., 2006; *Célérier et al*., 2009; *Herman et al*., 2010; *Robert et al*., 2011; *Whipp et al*., 2007], (2) some have used simpler one-dimensional thermal models [*Long et al*., 2012; *Thiede et al*., 2009] that do not take into account the geometric complexities of the subsurface thermal field and the horizontal component of particle paths, potentially biasing exhumation rates, and (3) exhumation rates calculated from near-vertical age-elevation profiles [e.g., *Blythe et al*., 2007; *Grujic et al*., 2006; *Huntington et al*., 2006] imply a range of assumptions [e.g., *Ehlers*, 2005; *Huntington et al*., 2007; *Mancktelow and Grasemann*, 1997] regarding the particle paths and the geometry of isotherms at depth that also may yield poor estimates of the long-term exhumation rates.

4.5. Modeling Results

In the following sections, we describe inversion results from the two tectonomorphic scenarios (for details, see Table 6) and for each transect.

4.5.1. Constant Slip Rate on the MHT

4.5.1.1. Inversion Set Western Bhutan 1 (WB1)

As described in section 2, available geophysical constraints for the MHT along the western transect (Figure 3a) are used to evaluate the model's ability to reproduce realistic age patterns and fault geometries for the basal detachment. In this initial inversion, we let the geometry of the MHT vary within the range defined by geophysical and geological data at points 1, 2, and 4, as indicated in Figure 3a (red bars/box). The Himalayan shortening rate range is 20–24 mm/yr and the convergence partitioning range is 0.5–0.9 (these ranges are also used in subsequent inversions; see Table 6). We allowed the basal temperature and the heat production to vary between 500–1000°C and 0–30°C/My, respectively. This first inversion set comprises 20,816 forward models (Figure 8), and parameter values for the best fit solution can be found in Table 6.

The results of the inversion demonstrate the data are particularly sensitive to the geometric and kinematic parameters, with NA appraisal producing Gaussian- and exponential-shaped 1-D PPDFs for Z_4, X_1, and λ (Figure 8). The minimum misfit value observed was 0.65, indicating a good overall fit to the data. The calculated MHT geometry is in excellent agreement with geophysical data for points 2–4 (see Figures 8b and 9c). The flat segment of the detachment in the shallowest part of the section (between points 1 and 2) located at 15 km depth is consistent with the highest values proposed in Sikkim by *Acton et al.* [2011] but 5 km deeper than cross-section balancing results by *Bhattacharyya and Mitra* [2009] and *Tobgay et al.* [2012] (Figures 8c and 9c). The location of point 1 produces a steep (65–70°) frontal fault segment linking the 15 km deep point 1 to the surface exposure of the MBT. This geometry is likely the result of the model attempting to reproduce the steep age gradient observed in the southernmost part of the western transect (Figure 5a). The convergence rate is poorly resolved with values ranging between 20 and 23 mm/yr (Figure 8d), but the partitioning value of 0.68 is very well defined and indicates that about one third of the convergence is accommodated by overthrusting at rates of 6–7 mm/yr, consistent with previous studies [*Herman et al*., 2010; *Robert et al*., 2011; *Whipp et al*., 2007]. The preferred temperature at the base of the model falls between 800 and 900°C, with a best fit at 841°C and coupled with a low radiogenic heat production of 0.13°C/My (Figure 8a). Although the thermal parameters in the model appear to be well defined, we found in test inversions that this good fit occurs both for combinations

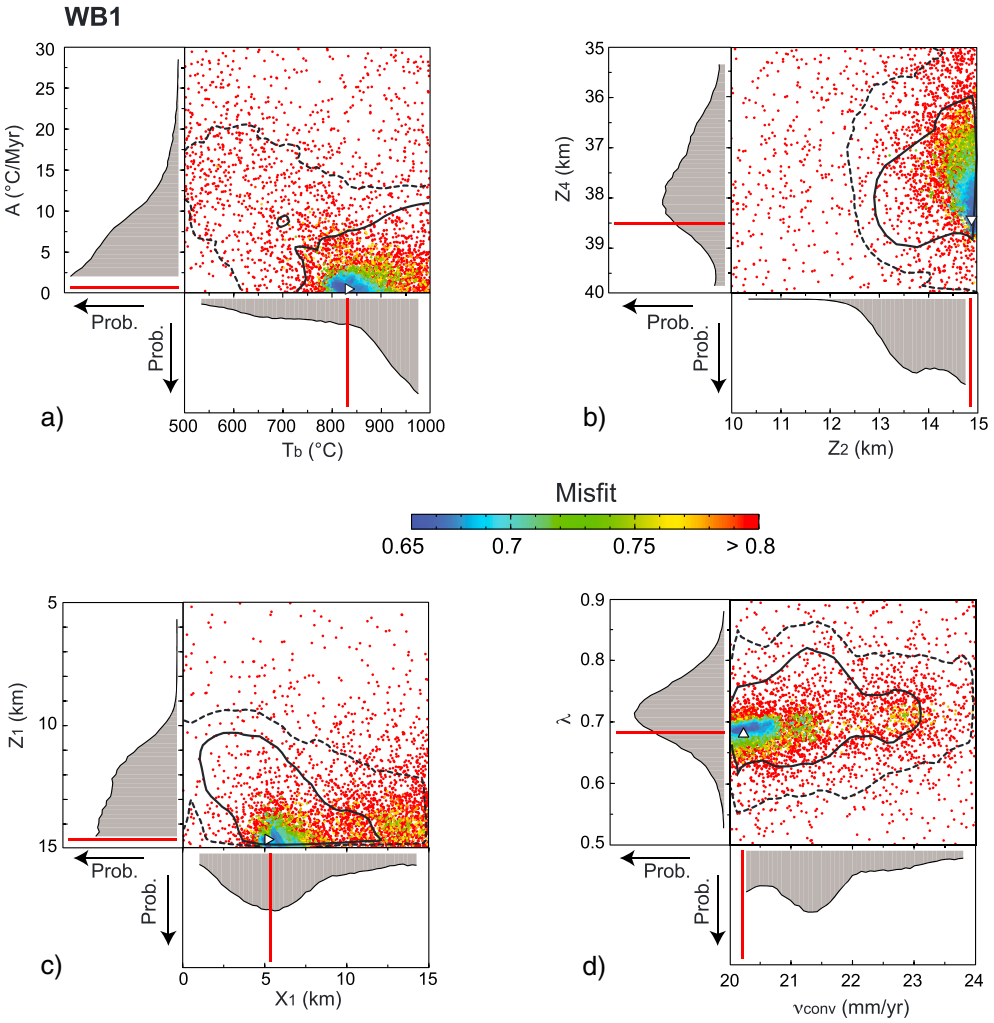

Figure 8. Inversion results for model West Bhutan 1 (WB1) solving for eight free parameters. In the largest frames, each dot represents a single forward model, and the color scheme associated with each dot corresponds to the goodness of fit to the data set (see color scale: red dot = highest misfit, blue dot = lowest misfit). The white triangle represents the parameter values used in the forward model with the lowest overall misfit. One-dimensional posterior Probability Density Functions (PPDFs) derived from the NA appraisal are shown adjacent to the axes for each parameter. The red lines indicate parameter values for the lowest misfit forward model. Two-dimensional PPDFs are represented by lines overlying the scatter diagram where the solid black line is the 1σ confidence interval and the dashed line the 2σ confidence interval.

of high basal temperature and low heat production and vice versa, suggesting the model can produce similar ages for both. For example, correlation matrices between the different free parameters calculated for each inversion from the neighborhood algorithm [*Sambridge*, 1999b] (see Data Set S1, Appendix G) show that the strongest correlation of parameters in model WB1 is an anticorrelation between the basal temperature of the model (Tb) and the heat production (A). With that in mind, and in order to reduce the number of model-free parameters in subsequent inversions, we have chosen to fix the basal temperature and radiogenic heat production to the best fit values from inversion WB1 (Table 6). Predicted ages obtained from a forward model using the parameters yielding the lowest misfit fit reasonably well with observed AFT, ZHe, and ZFT data, but the predicted AHe ages are much younger than the observed (Figure 9a).

Instantaneous exhumation rates extracted from the model velocity field show very rapid exhumation in the immediate MBT hanging wall, rapid exhumation across the LHS and southern GHS, and slow to no exhumation further north. Instantaneous exhumation rates are derived from the model velocity field at $t = 0$ Ma and correspond to the vertical component of the velocity vectors at the surface (Figure 6b, $vz_{n,inst}$), which are controlled by the fault geometry and slip rate. The modern distribution of instantaneous exhumation from

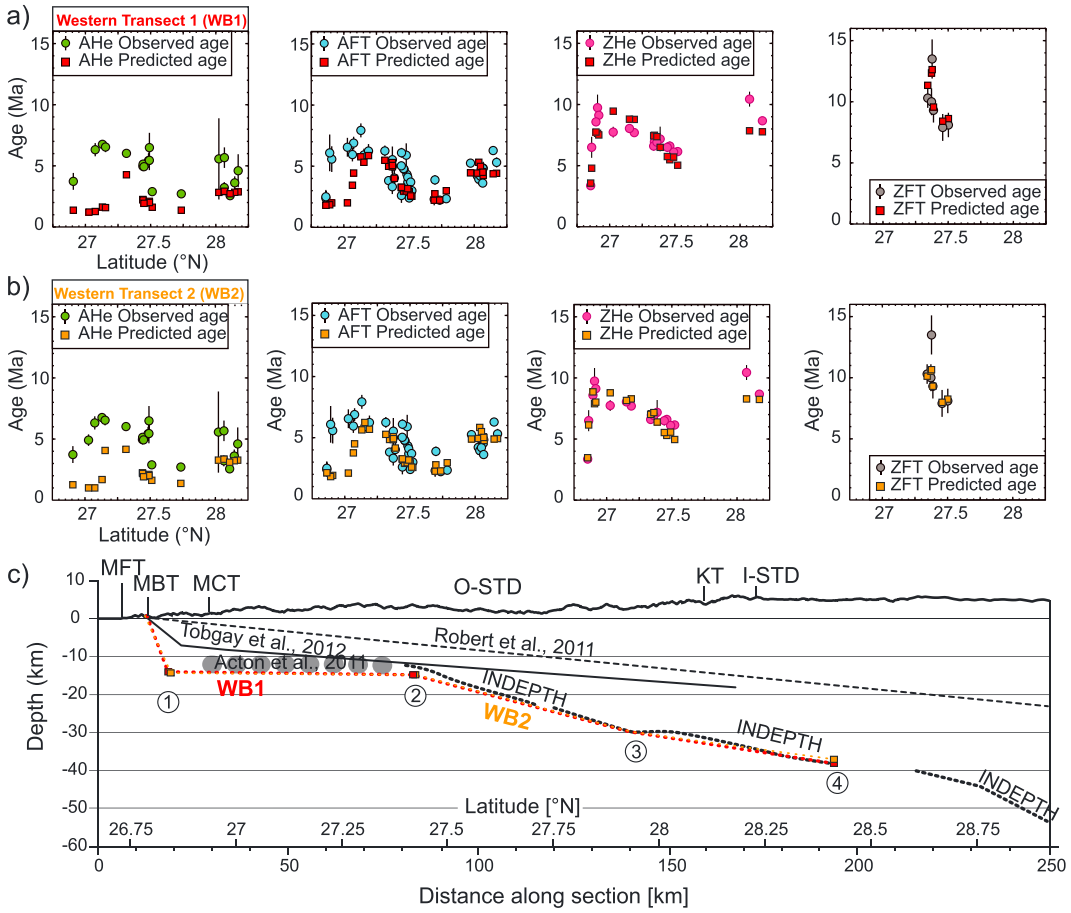

Figure 9. Cooling ages and preferred MHT geometry for the western transect inversions. Observed cooling ages along the western transect with the predicted cooling ages from the forward model with the lowest misfit in inversions (a) WB1 and (b) WB2. (c) MHT geometry for lowest-misfit forward model in inversions WB1 (red) and WB2 (orange) with resulting MHT geometry data.

model WB1 (Figure 10b) indicates that from south to north, there is a 2–3 km wide band of rapid exhumation of up to 6 mm/yr located above the frontal MBT ramp, an exhumation rate decrease to 3 mm/yr until 50 km north of the MBT, an abrupt decrease to near 0 values at the northern extremity of the flat segment, an increase between 100 and 170 km north of the MBT to values of ~1.8 mm/yr, and finally, a decrease to 1 mm/yr due to the slightly shallower dip of the MHT north of 170 km (Figure 10b).

The results of our inversions highlight the significant tectonic/advective distortion of the crustal isotherms; deformation of the subsurface thermal field induces substantial north-south changes in the geothermal gradient (Figure 10a). Mean surface heat flow predicted by the model vary from 8.8 ± 1.0 mW/m^2 in the foreland to 56.6 ± 12.3 mW/m^2 in the hinterland (Figure 10c). Moreover, the obliquity of the particle paths with respect to these deformed isotherms (Figures 7 and 10c) variably impacts the cooling ages exposed at the surface for the different thermochronometers, as was discussed in section 4.3.

4.5.1.2. Inversion Set Eastern Bhutan 1 (EB1)

Geophysical constraints on the MHT geometry beneath eastern Bhutan are scarce to nonexistent, requiring a larger number of geometric free parameters (Table 6 and Figure 3b). In this inversion, all points are free parameters in both the *X* and *Z* directions (except for point 5, free only in the *Z* direction), with ranges defined based on a balanced cross section by *Long et al.* [2011a] for the southern points and geophysical data projected from the west for the northern point 5 (Table 6 and Figure 3b). Similar to WB1, the convergence rate and partitioning are also free parameters. As mentioned in the previous section, input thermal parameters are the best fit values from inversion WB1. We however note that we have performed a test inversion letting the basal temperature free and that it returned similar results as those described below. This inversion set required 24,222 forward models (Table 6).

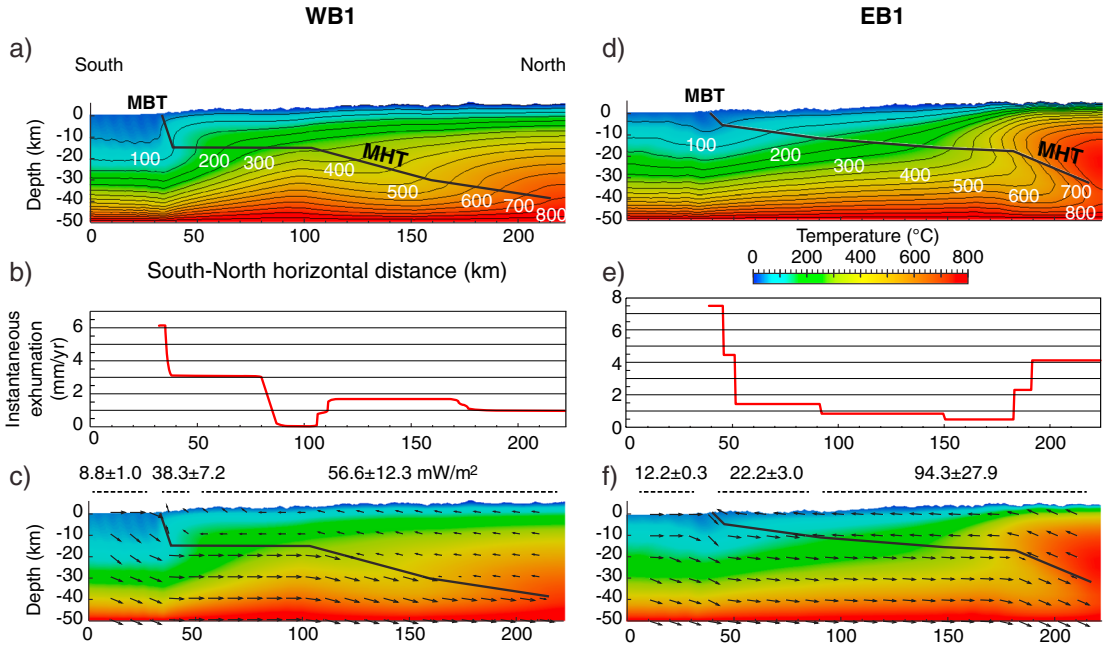

Figure 10. Thermal field and instantaneous exhumation rates for single-stage inversions in western and eastern Bhutan. Cross sections showing MHT geometry with thermal field, instantaneous exhumation rates, and velocity vectors for the (a–c) western (WB1) and (d–f) eastern (EB1) transects. Values of the predicted mean heat flow (mW/m^2) are provided in Figures 10c and 10f for the foreland, LHS, and GHS units.

Again, the model shows strong sensitivity to the geometric parameters and convergence partitioning factor, with Gaussian- and exponential-shaped PPDFs produced for parameters λ, Z_5, X_4, Z_4, Z_3, Z_2, X_1, and Z_1. The depth of the northernmost point (Z_5) is constrained between 31 and 35 km (Figure 11a), which is consistent, but slightly shallower than the equivalent on the western transect. Most other geometric points also yielded narrow position ranges (Figures 11b–11d). In the south, these results are in good agreement with *Long et al.* [2011a], and in the north, they imply the presence of a major crustal ramp north of 28°N, dipping 23° northward (Figure 12c), which is a feature that is not observed in geophysical data in the west (Figure 3a). This ramp produces young predicted ages at 28°N for all thermochronologic systems (Figure 12a), which are significantly different from the observed ages, specifically for ZHe and ZFT where the difference can reach 5 and 10 Ma, respectively (Figure 12a). Finally, similar to WB1, the convergence rate is poorly defined, (Figure 11f), and the convergence partitioning factor hits the range value with a low best fit value of 0.53 (Table 6). The latter implies that up to 47% of the convergence is accommodated by overthrusting, yielding abnormally high overthrusting rates of up to 9.5–11 mm/yr as compared to the 25–30% suggested by previous studies [e.g., *Herman et al.*, 2010] and that from the western transect.

The distribution of instantaneous exhumation rates is comparable to WB1 in that exhumation is most rapid in the immediate MBT hanging wall, but EB1 also shows rapid exhumation in the far north of the eastern transect. From south to north, the instantaneous exhumation rates are highest across a narrow range in the first 10 km from the trace of the MBT with rates of 7.5 to 4.5 mm/yr (Figure 10e). From there the rates decrease progressively northward down to values of 0.5 mm/yr at 180 km before finally increasing to 4 mm/yr above the northern ramp (Figures 10e and 10f). The resulting thermal field is heavily perturbed in the northern section of the eastern transect, where heat is rapidly advected above the steep ramp, whereas thermal differences between the hanging and footwall are less pronounced in the south, atop the flatter segment of the MHT (Figure 10d). Mean surface heat flow predicted by the model vary from 12.2 ± 0.3 mW/m^2 in the foreland to 94.3 ± 27.9 mW/m^2 in the hinterland (Figure 10f).

4.5.2. Two-Stage Partitioning of Slip on the MHT

In order to explore the potential for temporal variations in exhumation rates over the 12 Ma model run time, we ran two sets of inversions that permitted a change in the convergence partitioning factor (explored range between 0.5 and 0.9) at a transition time between 7 and 2 Ma. This range encompasses the timing of proposed changes in exhumation rate suggested by previous studies [e.g., *Grujic et al.*, 2006; *Huntington et al.*, 2006]. Because the models

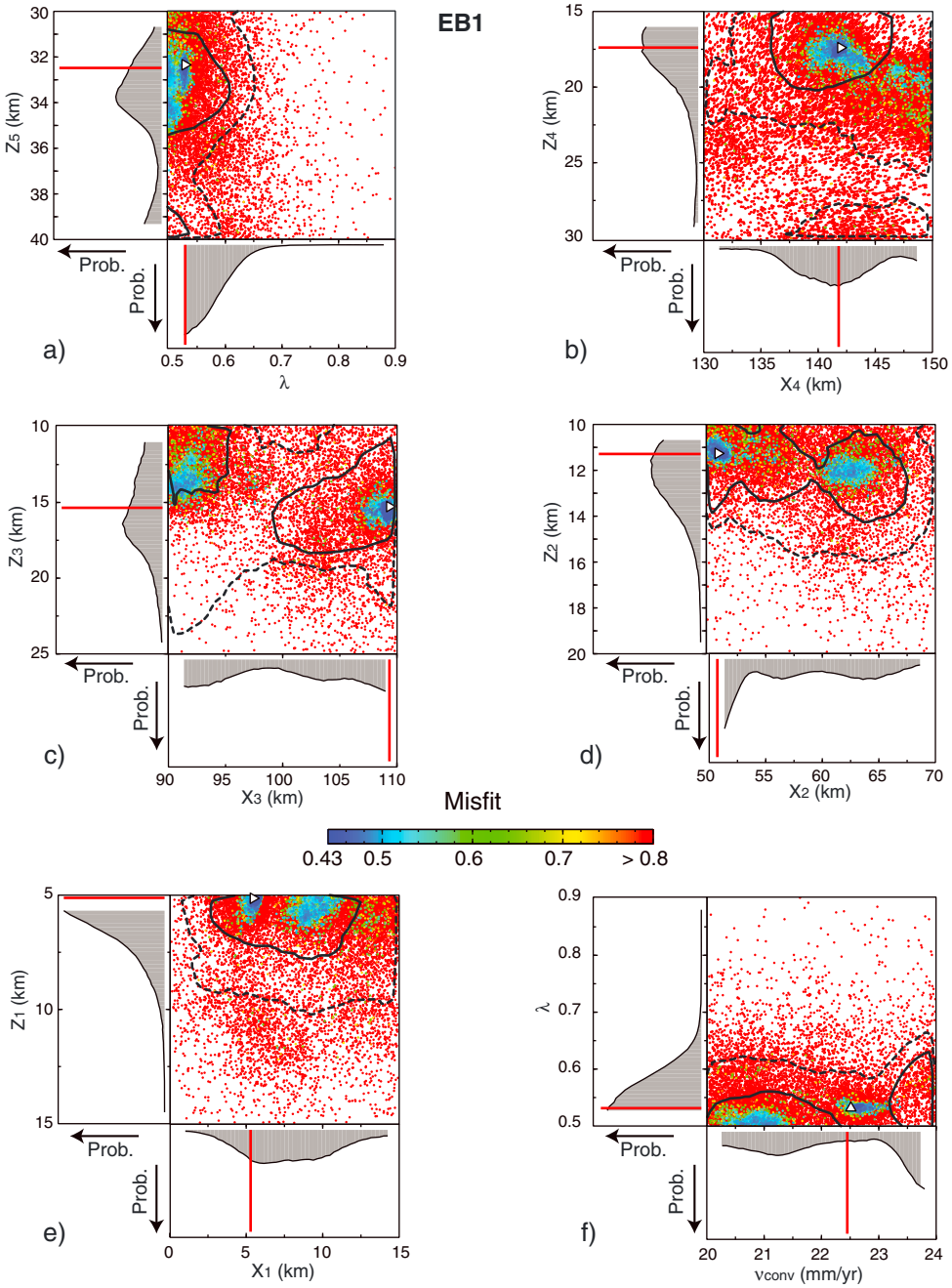

Figure 11. Inversion results for model East Bhutan 1 (EB1) solving for 11 free parameters. Symbols and plot layout are as in Figure 8.

have steady state topography, any change in convergence partitioning from the first stage to the second stage (λ_1 and λ_2, respectively) would produce a proportional change in exhumation rates in the hanging wall of the MBT. If $\lambda_1 > \lambda_2$, it would correspond to an increase in exhumation rate, and if $\lambda_1 < \lambda_2$, the exhumation rate will decrease. Note that the thermal and geometric parameters and the convergence rate do not change with time in these simulations but are allowed to be different than in WB1 and EB1.

4.5.2.1. Inversion Set Western Bhutan 2 (WB2)

In spite of adding free parameters for the transition in convergence partitioning, inversion WB2 has one less free parameter than WB1 and converges more rapidly. We reduced the number of free geometrical parameters to two points (1 and 4) and relied on the geophysical data for the others. As mentioned above, the convergence rate (v_{conv}), partitioning factors λ_1, λ_2, and the transition time were also investigated (Table 6).

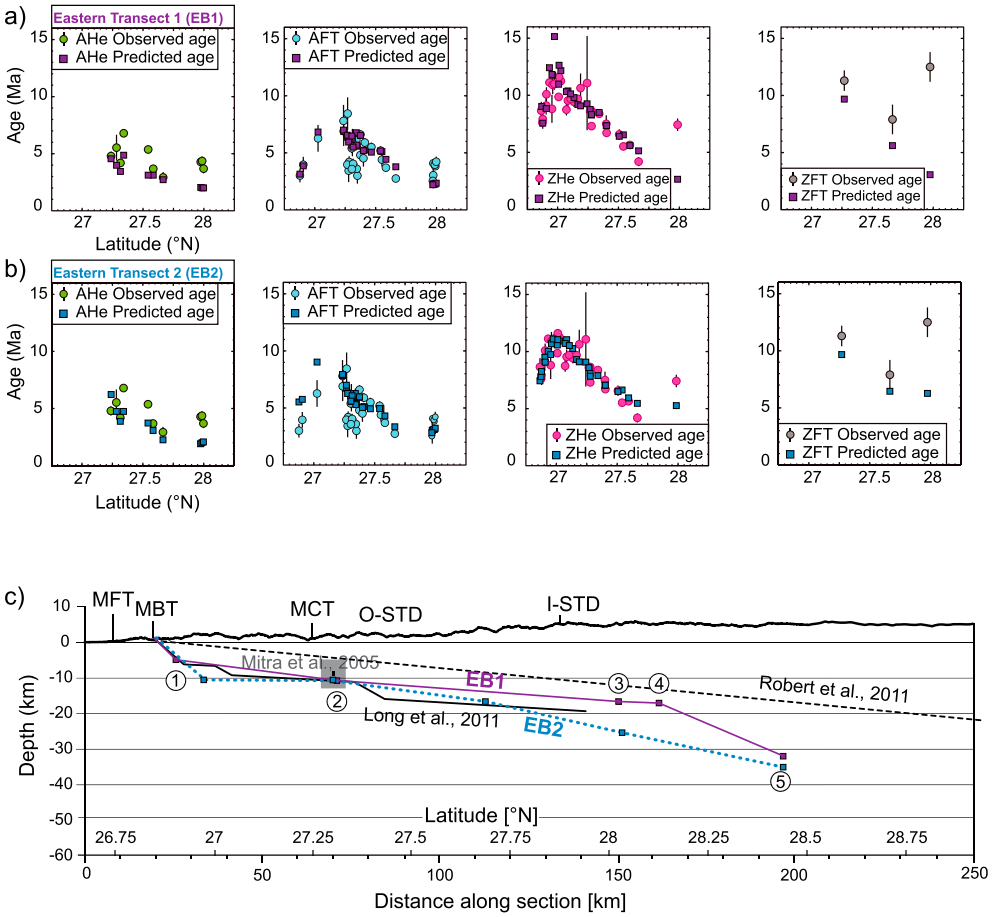

Figure 12. Cooling ages and preferred MHT geometry for the eastern transect inversions. Observed cooling ages along the eastern Bhutan with the predicted cooling ages from the forward model with the smallest misfit in inversions (a) EB1 and (b) EB2. (c) MHT geometry for lowest-misfit forward model in inversions EB1 (purple) and EB2 (blue) with resulting MHT geometry data.

Convergence was reached after running 15,414 forward models, with a minimum misfit value of 0.63, similar to that found in inversion WB1.

Similar to WB1, the data show sensitivity to the geometric parameters and convergence partitioning factors, yielding a MHT geometry identical to that found in WB1 (Figures 9c, 13a, and 13b). The inversion produces Gaussian- and exponential-shaped PPDFs for parameters λ_1, λ_2, X_1, and Z_1 (Figure 13). This inversion included a two-stage exhumation history, but the transition time at ~4.3 Ma was poorly defined (Figure 13c). Part of the poor transition time definition may relate to the fact that similar optimal partitioning factors were found (Figure 13d) for the two stages; the forward model with the lowest overall misfit yielded values of 0.69 and 0.73 for λ_1 and λ_2, respectively (Figure 13d and Table 6). Although the best forward models, represented by the clusters in Figure 13, are located on the upper left side of the steady exhumation line (Figure 13d, bold grey dashed line) suggesting that there is a tendency for the exhumation to decelerate by 5–10% sometime after 4–5 Ma, the 1σ uncertainty in the rate change (Figure 13d, heavy black line) suggests there may be no requirement for an exhumation rate change. Finally the forward model with parameters yielding the lowest misfit shows that the predicted ages fit the observed ages just as well as they do for model WB1, except again for AHe data (Figure 9b).

4.5.2.2. Model Eastern Bhutan 2 (EB2)

Due to the lack of geophysical data along the eastern Bhutan, eight geometric parameters were kept free and a two-step evolution was allowed, as described in the previous section requiring a larger number of forward models to reach convergence (Table 6). In total, 20,424 forward models were run, yielding a minimum misfit value of 0.43, identical to the first step run for the same transect (EB1).

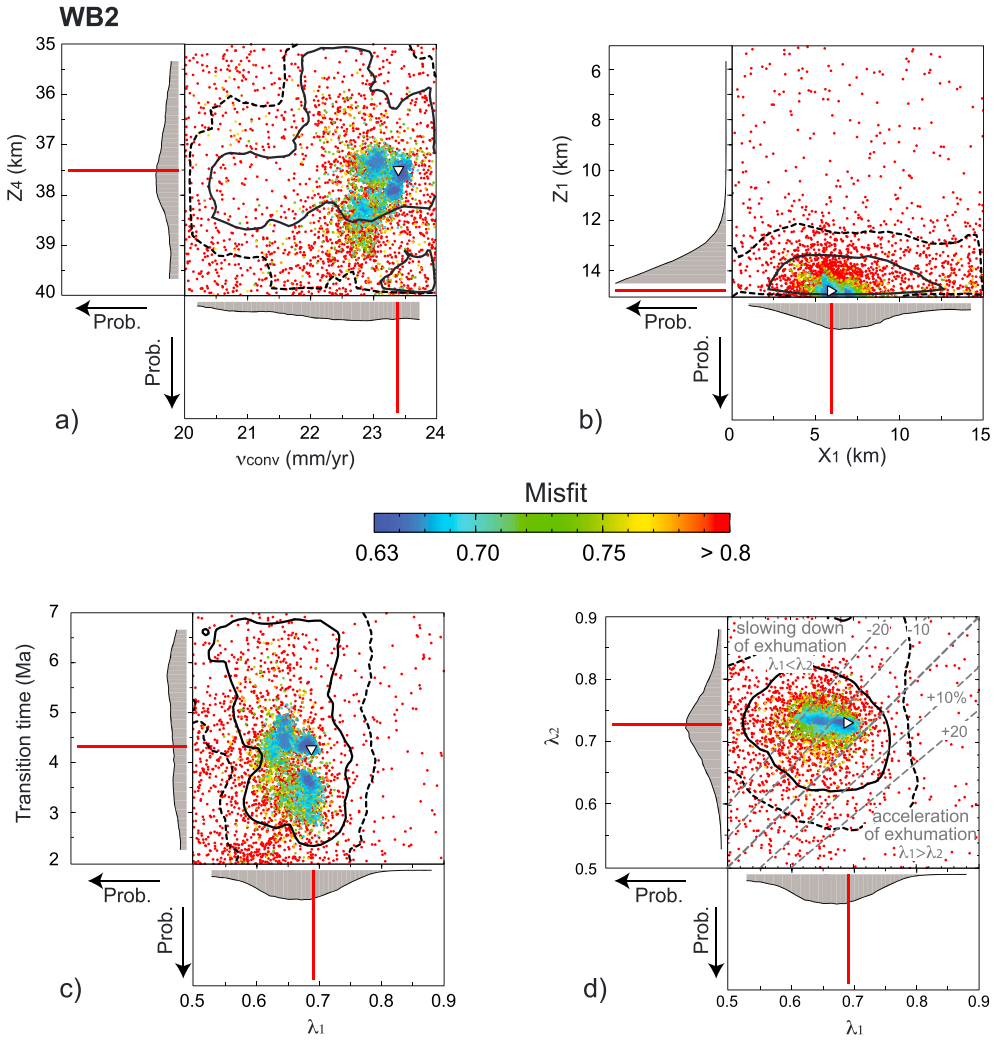

Figure 13. Inversion results for model western Bhutan 2 (WB2) solving for seven free parameters. Symbols and plot layout are as in Figure 8.

Surprisingly, in this inversion the model not only shows a significant change in the convergence partitioning (exhumation rate) but the geometry of the MHT is also significantly different than that obtained in inversion EB1 (Figure 12c). Similar to above, the model showed sensitivity to the geometric parameters and partitioning factor, producing Gaussian- and exponential-shaped PPDFs for parameters λ_1, λ_2, X_4, Z_3, X_3, Z_2, X_2, Z_1, X_1, and the transition time (Figure 14). For the model geometry, the frontal segment dips at similar moderate angle of 40° but roots deeper at 10 km (Figures 12c and 14d) and remains subhorizontal until point 2 (Figures 12c and 14c). North of that point, the MHT steadily dips northward at 9–11°, and there is no inflection or ramp north of 28°S as observed in EB1, (Figures 12c and 14a–14c). Note that Z_4 remains poorly constrained (Figure 14a) and may vary between 20 and 30 km. A well-defined transition time at about 5.9 Ma (Figure 14e) separates a pre-5.9 Ma time interval (stage 1) characterized by a low partitioning factor (best fit model returned a value of 0.56) and a post-5.9 Ma stage 2 characterized by a higher partitioning factor (best fit is 0.79) (Figure 14f). The convergence rate, again poorly defined, has a lowest-misfit value of 22.7 mm/yr (Figure 14e), yielding overthrusting rates of ~10 and 4.7 mm/yr for stages 1 and 2, respectively. These results suggest that along this transect, exhumation rates decelerated by about 30–50% after ~6 Ma (Figures 14e and 14f), in this case reflecting a statistically significant rate change, as shown by the 2-D PPDFs for the convergence partitioning factor (Figure 14f). Although this two-step model returned a similar misfit value than EB1, it yields a better fit between predicted and observed ages than EB1 for all the thermochronologic

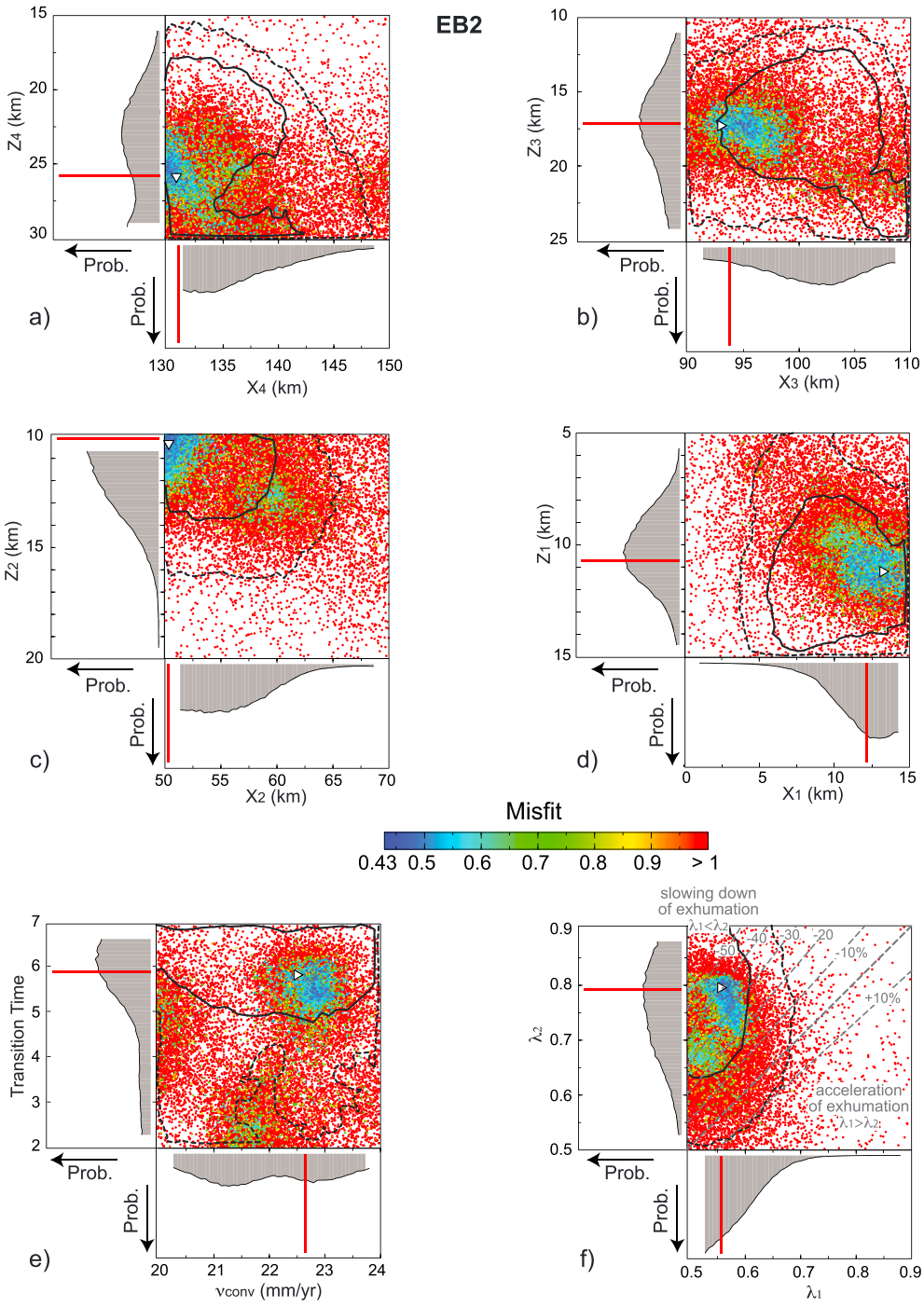

Figure 14. Inversion results for model East Bhutan 2 (EB2) solving for 12 free parameters. Symbols and plot layout are as in Figure 8.

systems (except for the three southern AFT data, Figure 12b), in particular north of 28°N, where a better fit can be attributed to the absence of the steep ramp observed in that location in inversion EB1 (Figure 12c).

The spatial distribution of instantaneous exhumation rates for both stages is similar because the geometry of the MHT does not change through time, but the rate decreases (Figures 15b and 15e). Higher overthrusting rates before 5.9 Ma produce more rapid advection of heat and a larger thermal perturbation as compared to the second stage from 5.9 Ma to present (Figures 15a and 15d) and trigger a drastic decrease of predicted mean flow values at the surface (Figures 15c and 15f).

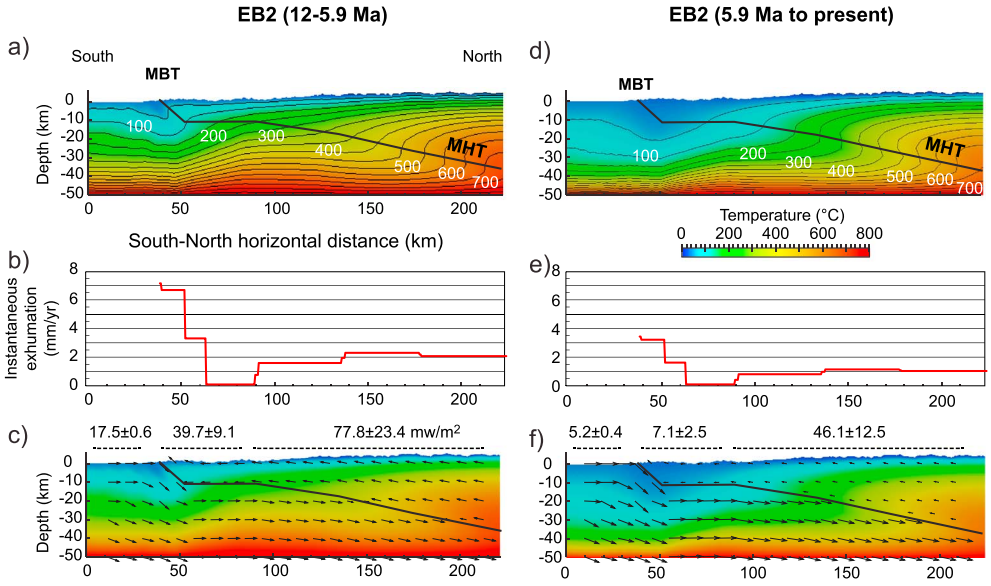

Figure 15. Thermal field and instantaneous exhumation rates for two-stage inversion in eastern Bhutan (EB2). Cross sections showing MHT geometry with thermal field, instantaneous exhumation rates and velocity vectors for the (a–c) step 1 (12–5.9 Ma) and (d–f) step 2 (5.9 Ma to present) of the run. Values of the predicted mean heat flow (mW/m^2) are provided in Figures 15c and 15f for the foreland, LHS, and GHS units.

The instantaneous exhumation rates along the transect feature a 10 km wide domain of fast exhumation located above the frontal ramp of the MHT in the south, with rates reaching 7–6.5 mm/yr during stage 1 and 3 mm/yr during stage 2. Further north, exhumation rates decrease abruptly to values near 0 above the subhorizontal segment of the MHT where particle paths are horizontal, and north of the flat segment where the MHT dips steadily at 9–11°, exhumation rates increase to about 1.5–2 mm/yr prior to 5.9 Ma and 0.8–1 mm/yr between 5.9 Ma and the present (Figure 15).

5. Discussion

Before discussing our results, we emphasize that our thermokinematic model is not coupled to surface-processes or landscape-evolution models. As a consequence, the model topography does not evolve with time and exhumation is controlled by a combination of model topography and underlying fault kinematics.

5.1. Geometry of the Main Himalayan Thrust

In Bhutan, the MHT can be divided into three main segments, from north to south: (a) A deep crustal ramp north of 27.5°N, (b) a flat section at ~ 10–15 km depth extending 26.8–27.3°N in the west and 27–27.3°N in the east, and (c) a steep frontal ramp (Figures 9c and 12c). In the following discussion, we review our preferred model geometries, their relationship to available data, and possible explanations for discrepancies in our calculated MHT geometries. Along most of the western transect (where geophysical data provide both the basis and support for our results), the model predicts the MHT geometry well, suggesting that tectonic displacement on the MHT may be the dominant influence on upper crustal cooling and exhumation. Conversely, geometric anomalies in some fault sections may reflect an oversimplified fault model or the influence of external forcing (e.g., climate-driven erosion, variability in rock erodibility, and transient fluvial erosion) on the cooling age distribution.

We find our preferred MHT geometries are in broad agreement not only with available geophysical data but also with structural reconstructions and other important geological observations. North of 27.5°N, previous thermokinematic modeling [*Robert et al.*, 2011] and results from balanced cross sections [*Long et al.*, 2011a; *Tobgay et al.*, 2012] predict that the MHT is located at a depth ranging between 15 and 25 km below the surface trace of the I-STDS. As previously mentioned, this geometry is incompatible with INDEPTH data (see Figure 3) and is too flat to allow for the occurrence at the surface of late Miocene granulitized eclogites exhumed from crustal depths of ~70 km to midcrustal depths (20–30 km) in the hanging wall of the Kakhtang

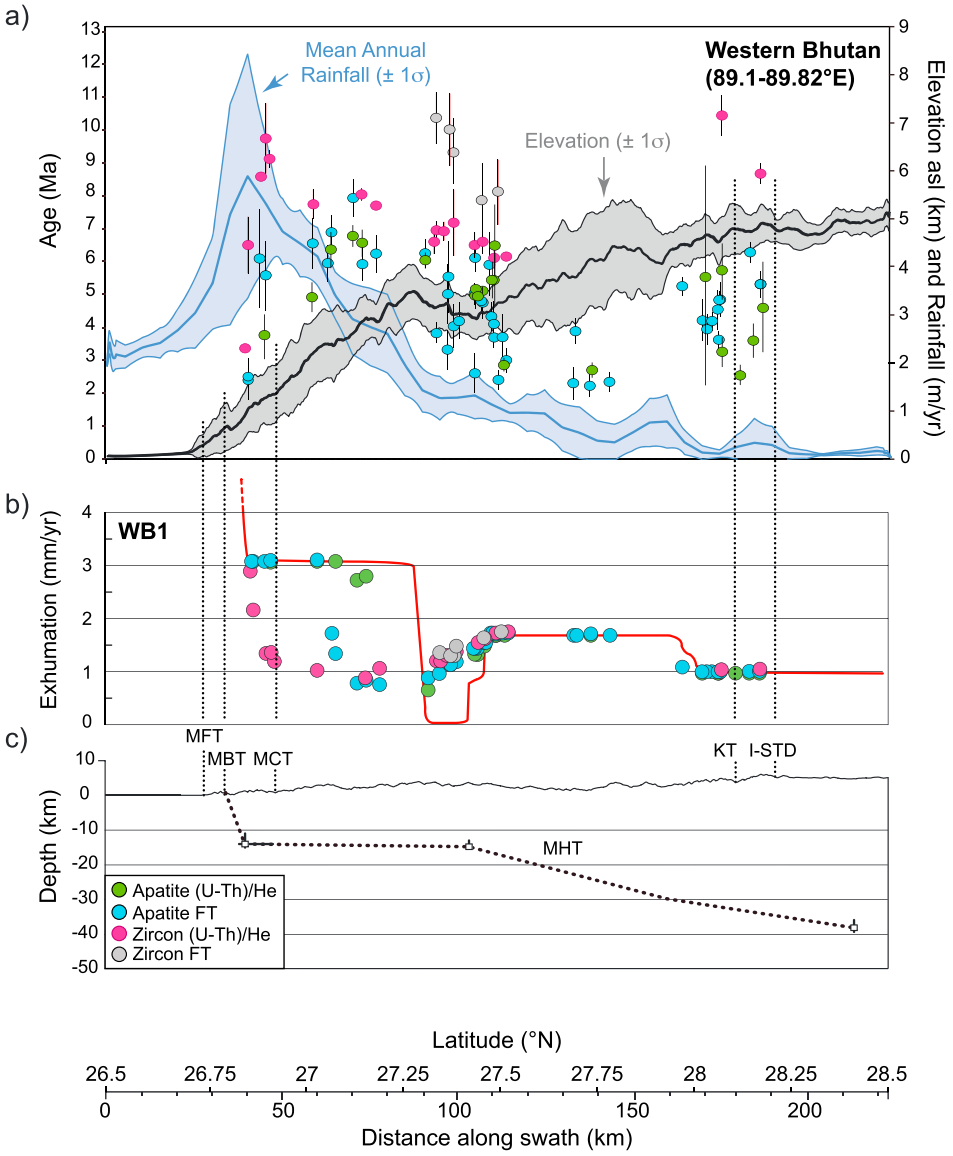

Figure 16. Summary of the results for the western transect. (a) North-south distribution of cooling ages. Mean topographic profile is represented by the bold black line and minimum/maximum elevations by the thin black lines. Mean annual rainfall distribution represented by the bold blue line and minimum/maximum values by the thin blue lines. The location of the main shear zones are represented by vertical dotted lines. Abbreviations are as in Figure 1. Color coding is as in Figure 5. (b) Instantaneous (red line) and long-term (colored dots) exhumation rates; each dot represents the long-term exhumation value returned by each sample reported in Figure 16a; (Color coding: green, AHe sample; blue, AFT sample; pink, ZHe sample; and grey, ZFT sample). (c) Geometry of the MHT as obtained in run WB1.

Thrust in ~ 2 Ma [*Grujic et al.*, 2011], nor of the MCT zone gneisses and migmatites isothermally decompressed from crustal depths of 37–45 km to 22–15 km in the mid-Miocene [*Chakungal*, 2006; *Daniel et al.*, 2003]. *Robert et al.* [2011] inverted a much smaller and suboptimally distributed AFT data set, concluding that the MHT in Bhutan is a plane steadily dipping northward at 5–7°, which does not fit the geophysical data (Figure 3). This is confirmed by a test inversion with free thermal (basal temperature and heat production) and kinematic (partitioning and convergence rate) parameters, allowing the dip of the MHT to vary between 5 and 7° toward the north. Results from the test inversion are unable to reproduce the north-south distribution (and variation) of the thermochronologic ages presented in this study. In contrast, we find geometries that place the MHT at depths of 30–40 km at the northern extremity of our models (28.5°N) (Figures 9c and 12c). Further south, the flat segment between points 1 and 2 (Figure 9c) is in broad agreement with balanced cross

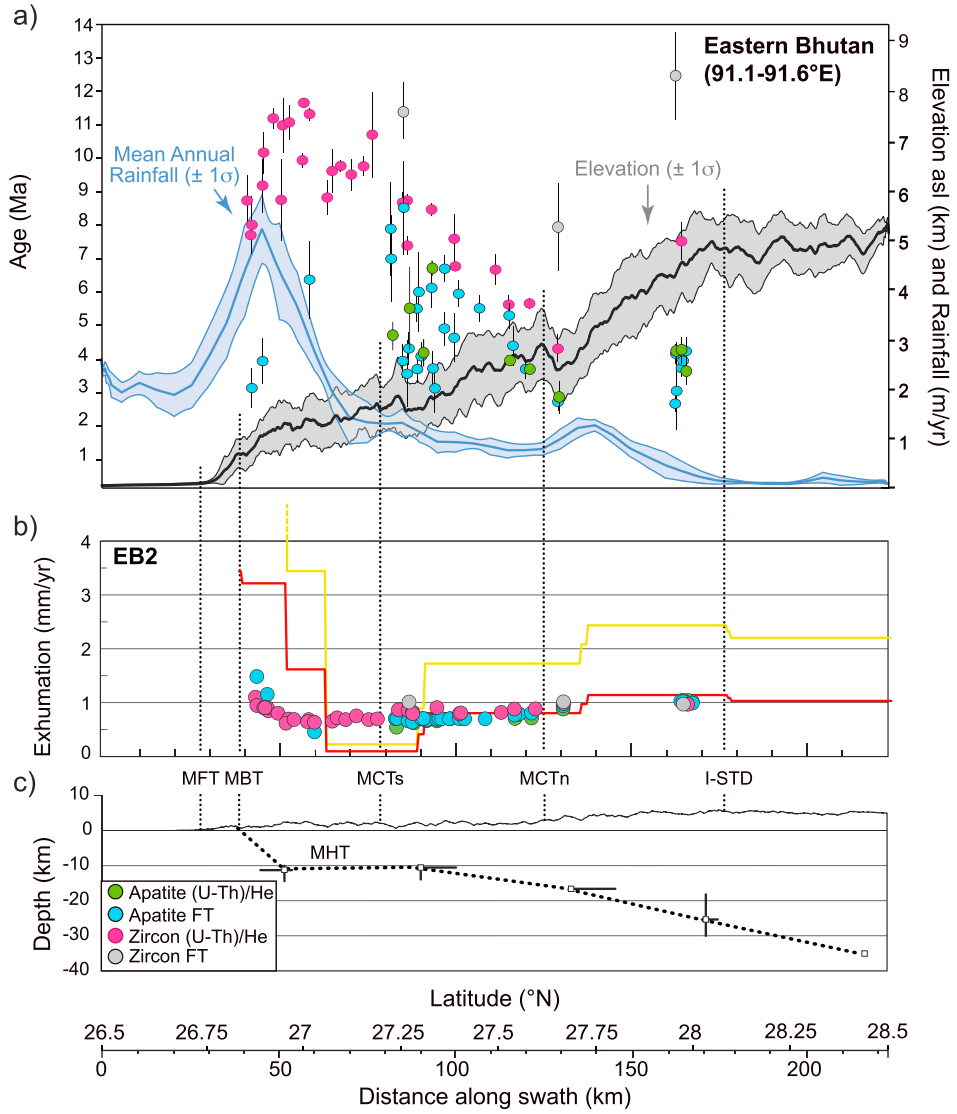

Figure 17. Summary of the results for the eastern transect. (a) North-south distribution of cooling ages. Mean topographic profile is represented by the bold black line and minimum/maximum elevations by the thin black lines. Mean annual rainfall distribution represented by the bold blue line and minimum/maximum values by the thin blue lines. The location of the main shear zones are represented by vertical dotted lines. Abbreviations are as in Figure 1. Color coding is as in Figure 5. (b) Instantaneous (red line: stage 12–5.9 Ma; yellow line: stage 5.9 Ma to present) and long-term (colored dots) exhumation rates; each dot represents the long-term exhumation value returned by each sample reported in Figure 17a; same color coding as in Figure 16. (c) Geometry of the MHT as obtained in run EB2.

sections, although the western flat is 2–7 km deeper than that of *Tobgay et al.* [2012] yet within error of the geophysical data. In the east, the calculated MHT flat fits well with the geometric model of *Long et al.* [2011a], although the resolution of the thermochronologic data set and the limited number of points defining the MHT geometry preclude from predicting a geometry that includes alternating ramps and flats, as suggested by *Long et al.* [2011a] (Figure 12c).

The southernmost segment of the MHT is a steeply northward dipping (65–70° in the west and 40° in the east) frontal ramp rooted at 15 and 10 km in the west and east, respectively (Figures 9c and 12c). This geometry is different from that documented by geological cross sections available at the toe of the wedge [*Long et al.*, 2011a; *Tobgay et al.*, 2012]. These differences may reflect (1) biases introduced by the thermochronological data set characteristics (age, uncertainty, and spatial distribution of the data) and/or (2) erosion rates that are not in balance with tectonic uplift rates. Each point is discussed separately below.

First, the misfit function we use (equation (2)) is quite sensitive to the size of the age uncertainties. Comparisons between observed and predicted ages (Figures 9 and 12) suggest that the model is most sensitive to ages with very small measurement uncertainties and will tend to minimize the misfit to the ZHe data, because they have smaller uncertainties than AFT and AHe systems. For example, along the frontal part of the western transect, sample BU07-60-z1 has a young ZHe age of 3.36 Ma and a very low analytical error of 0.05 Ma (Table S2), mostly because there is only one aliquot for this sample. To determine how sensitive the inversion is to this sample and assess whether our results may be biased by the very low uncertainty, we performed a test inversion equivalent to WB1 but without the ZHe age of sample BU07-60-z1 in the age data set. The resulting geometry of the frontal segment has a rooting depth of 10 km and a dip of about 55°, instead of 15 km and 70° in WB1, suggesting the geometry is sensitive to this individual ZHe age. However, sample BU07-60-z1 is likely not an outlier, because it is located next to and compatible with the cooling ages of samples BHF01a and b, with AFT ages of 2.5 ± 0.6 and 2.4 ± 0.6 Ma, respectively (Figure 5). Thus, we see no objective reason that the ZHe age from sample BU07-60-z1 should be excluded from the age data set.

Second, there are several potential reasons why the proximal part of the MBT hanging wall may have experienced rapid localized surface erosion. First, high erodability of surface rocks may facilitate focused denudation. In western Bhutan this seems unlikely because the rocks exposed within 5 km north of the MBT are quartzite intercalated with slates, phyllites, and dolomite of the Baxa Formation [see *Tobgay et al*., 2012, Figure 3] that are resistant to erosion as compared to sandstones of the Siwaliks. In the east, the leading edge of the steep frontal ramp is located beneath the mechanically weak Permian Gondwana sediments [*Gansser*, 1983]; however, those rocks are only exposed along a narrow (1–2 km wide) strip [see *Long et al*., 2012, Figure 2]. North of the Gondwana sediments, resistant Diuri and Baxa Formation are exposed similar to western Bhutan. It thus seems unlikely that focused erosion of the Gondwana sequence alone would generate significant change in the geometry of the model MBT. An alternative explanation for rapid localized erosion on the MBT is that the southernmost sections of both transects reside within the high monsoonal precipitation band located over the foothills of the wedge with rainfall of up to 6 m/yr [*Bookhagen and Burbank*, 2010] (Figures 16 and 17). If this precipitation zone has remained at this position for the past several million years and induced significant local erosion, it may compensate rapid rock uplift on a steep frontal ramp and allow for persistent steep geometries. In addition, high, spatially localized erosion rates may result in an upstream-propagating knickpoint that results in transient topography. Depending on whether landscape has reached steady state after disturbance, the current topography may represent a transient state and does not represent a balance between rock uplift and erosion. We note again that transient topography is not accounted for in the thermokinematic model.

Lastly, in eastern Bhutan the lack of geophysical data makes it difficult to verify the geological accuracy of our models results. The MHT geometries found by inversions EB1 and EB2 are very dissimilar (Figure 12c). EB1 predicts a steep northward dipping ramp north of 28°N that is not observed in the INDEPTH profiles in the west and which induces young ages north of 27.5°N, incompatible with observed ages (Figures 12a and 12c). The two-stage model, EB2, yields an overall better fit with the balanced cross-section data, is in better agreement with INDEPTH data and produces predicted ages in better agreement with observed ages (Figures 12b and 12c). For these reasons, we favor model EB2 as representing best the geometry of the MHT in eastern Bhutan.

5.2. Tertiary Exhumation Rates

In Bhutan, there is growing evidence for a drastic change in regional crustal exhumation rates around 10 Ma. Although our study mainly focuses on upper crustal exhumation in Bhutan after 10 Ma, it is important to first briefly discuss the pre-late Miocene lower-middle crustal exhumation rates to provide a context for the late Miocene to present upper crustal exhumation history as interpreted in this study.

5.2.1. Pre-10 Ma Exhumation Rates

Records of deformation in the Bhutanese Himalaya prior to 10 Ma include very rapid cooling of deep crustal rocks, exhumation of granulite grade metamorphic rocks between synchronous, subparallel but opposite sense shear zones that cannot be explained by conventional fold-thrust belt tectonics, suggesting exhumation by ductile extrusion and channel flow tectonics [e.g., *Grujic et al*., 2002; *Grujic*, 2006; *Hollister and Grujic*, 2006]. Nonuniform, spatially variable early to middle Miocene exhumation of rock from midcrustal depths is documented across the GHS, including (1) in southeastern Bhutan (south of Tashigang, Figure 1), where ~17–27 km of rapid exhumation in the MCT zone occurred between 18–13 Ma and present at rates of 3 to 9 mm/yr [*Daniel et al*.,

2003], (2) further north in the footwall of the Kakhtang Thrust, rocks were exhumed from midcrustal depths by 21–17 Ma, possibly aided by synchronous slip on the O-STD and MCT [*Chambers et al*., 2011; *Kellett et al*., 2009, 2010; *Tobgay et al*., 2012; *Warren et al*., 2011a], and (3) in the hanging wall of the Kakhtang Thrust in NW Bhutan (Figure 2), where granulitized eclogites experienced 20–44 km of exhumation in 1–2 Myr, implying exhumation rates of 10–44 mm/yr between 15 and 13 Ma, again possibly aided by coeval slip on the I-STD [*Grujic et al*., 2011; *Kellett et al*., 2009; *Warren et al*., 2011b]. Peak temperature metamorphic ages combined with muscovite $^{40}Ar/^{39}Ar$ ages across the GHS and upper LHS suggest very rapid cooling until 13–11 Ma (that may also be partly attributed to isotherm relaxation) and a common GHS-LHS cooling history by 10 Ma [*Castelli and Lombardo*, 1988; *Gansser*, 1983; *Kellett et al*., 2009, 2013; *Long et al*., 2012; *Maluski et al*., 1988; *Stüwe and Foster*, 2001]. Combined, these observations closely match predictions from numerical geodynamic models of channel flow tectonics in the Himalaya [*Beaumont et al*., 2004; *Jamieson et al*., 2004, 2006]. By 10 Ma, rock uplift/decompression rates decreased, perhaps in response to a decrease in the India-Eurasia convergence rate [*Molnar and Stock*, 2009]. Tectonometamorphic data [e.g., *Grujic et al*., 2011, Figure 9b] suggest that by circa 10 Ma, the upper-middle crust had cooled to temperatures at which the Himalayan range would dominantly deform by frictional plastic flow and act as a critical wedge. Thus, we suggest common cooling of the GHS by 10 Ma correlates with activation of the MBT and cessation of ductile deformation within the GHS, including the MCT, the KT, and the ductile STDS.

5.2.2. Post-10 Ma Exhumation Rates

Our thermokinematic models suggest contrasting late Miocene-to-present upper crustal exhumation histories for western and eastern Bhutan. In western Bhutan, post-10 Ma exhumation is compatible with steady displacement on the MHT at overthrusting rates of 6–7 mm/yr consistent with previous studies in Nepal [*Herman et al*., 2010; *Robert et al*., 2011; *Whipp et al*., 2007]. At a given location along our two transects, long-term exhumation varies in space, from 1–1.5 mm/yr north of 27.5°N down to 0.7 mm/yr where the MHT flattens, before increasing again up to ~3 mm/yr in the frontal part of the system (Figure 16). Note that the distribution of long-term exhumation rates does not spatially correlate with and mimic the shape of cooling ages distribution (Figures 16a and 16b) for the reasons explained in section 4.3. Where samples have been exhumed above a fault segment of constant dip angle, instantaneous and long-term exhumation rates agree (Figure 16), but where the MHT is subhorizontal, thermochronometer-derived exhumation rates calculated over millions of years do not equal to instantaneous exhumation (surface erosion) rates.

In contrast to western Bhutan, long-term exhumation rates in eastern Bhutan show considerably less variation along the two transect (Figure 17). Inversion EB2 provides the favored tectonic scenario with high overthrusting rates between 12 and 6 Ma that decrease considerably after ~6 Ma, causing instantaneous exhumation rates to decrease 40–50% after the transition time (Figure 17). Long-term exhumation rates averaged over the last 12 Ma, are spatially fairly constant along the transect with rates of 1 mm/yr in the north, 0.7 mm/yr along most of the transect, and 1–1.5 mm/yr above the MBT (Figure 17). Because the thermal field is relatively cool in the vicinity of the MBT during the last 6 Ma (Figure 15d), long-term exhumation rates do not match the instantaneous exhumation rates above the MBT.

5.2.3. Decrease in Exhumation Rates at 6 Ma: Western Versus Eastern Bhutan

Our model results suggest that upper crustal exhumation rates in the GHS and LHS in the Bhutan Himalaya may have decelerated at ~6 Ma, however, this rate change is only seen clearly along the eastern transect. Why did exhumation rates change only in eastern Bhutan? Besides a slightly different MHT geometry for each of these transects, the main tectonic difference between western and eastern Bhutan is the presence of the Shillong Plateau to the east of 90°E (see Figure 1 and *Biswas et al*. [2007, Figure 1]). The Shillong Plateau is a foreland basement uplift bounded by two steeply dipping reverse faults. Tectonic rock uplift and erosional exhumation initiated by 9–14 Ma [*Biswas et al*., 2007; *Clark and Bilham*, 2008]. Late Miocene mean cumulative shortening rates derived from thermochronologic data are only 0.65–2.3 mm/yr [*Biswas et al*., 2007] and 1–2 mm/yr [*Clark and Bilham*, 2008] across the Shillong Plateau. In contrast, GPS velocities suggest that possibly as much as 6.3 ± 3.8 mm/yr [*Paul et al*., 2001], 4.3 ± 4.8 mm/yr [*Sridevi Jade*, 2004], and more recently 4–7 mm/yr [*Banerjee et al*., 2008] of the India-south Eurasia convergence is accommodated in the Shillong Plateau region. Since the overall India-south Eurasia convergence rate has remained constant over the last 11 Ma [*Molnar and Stock*, 2009] and the reverse faults bounding the plateau were activated by 9–14 Ma [*Biswas et al*., 2007; *Clark and Bilham*, 2008], it seems unlikely that these two events triggered the deceleration of exhumation observed in eastern Bhutan at 6 Ma. However, the difference between long- and short-term mean cumulative shortening rates suggests that the shortening accommodated by

the Shillong Plateau might have increased during the latest Miocene; however, no data are available as to when this occurred and whether or not it reflects a longer-term tendency at Pliocene timescales. It is interesting to note that in central Bhutan at ~90°E, NS-trending active strike slip faults are aligned with the western margin of the Shillong Plateau [*Gansser*, 1983] [see *Meyer et al*., 2006, Figure 10 (Pho Chhu)]. These could potentially act as transfer structures accommodating different overthrusting rates between eastern and western Bhutan; however, there is admittedly no field evidence of large-scale displacement of major structures (e.g., MCT, RT, and MBT).

The study area, located in the wettest (eastern) part of the Himalaya, is unique in that it has a distribution of modern precipitation that mimics the topographic profile [see *Bookhagen and Burbank*, 2010, Figure 8] and rainfall amounts in the central and eastern Bhutan foothills may have been perturbed by the Pliocene surface uplift of the Shillong Plateau. The Shillong Plateau, with an average elevation of 1.6 km and Shillong Peak at ~2 km, forms an orographic barrier that forces out significant amounts of Indian Summer Monsoon rainfall on its southern slope, making the southern Shillong Plateau one of the wettest inhabited places on Earth [*Bookhagen and Burbank*, 2006, 2010]. Pliocene uplift of the Shillong Plateau [*Biswas et al*., 2007] may have also introduced a significant precipitation barrier in the foreland in eastern Bhutan, and it has been suggested that this change in precipitation distribution may have influenced upper crustal exhumation rates in the Bhutanese orogenic wedge during the Pliocene [*Grujic et al*., 2006]. However, our results suggest that the thermochronologic data are more compatible with a model in which exhumation of the hanging wall of the MBT is controlled by tectonically driven erosion processes. This contradicts *Grujic et al*.'s [2006] conclusions for the inner part of the orogenic wedge. It is worth noting, however, that in the Bhutanese foothills, the peak of mean annual precipitation spatially coincides with the steep and/or deeply rooted frontal ramp (Figures 16 and 17). We thus suggest that climatically controlled erosion south of 27°S may have enhanced the steep age gradient, requiring the numerical model to compensate for a steep, deep frontal thrust in order to replicate the abrupt age gradient. This is compatible with recent fidings suggesting that the morphology of the Himalayan foreland fold-and-thrust belt, south of the MBT, is primarily controlled by surface processes [*Hirschmiller et al*., 2014].

6. Conclusions

Our analysis of 101 new apatite and zircon (U-Th)/He and fission track in situ bedrock samples combined with extensive structural and geological field observations, and 3-D thermokinematic modeling of the thermochronological data allow us to make the following conclusions:

1. When combined with published data, our new substantial multithermochronologic data set plotted against latitude shows comparable cooling age distribution patterns in western and eastern Bhutan: from south to north, cooling ages increase from the Main Boundary Thrust to and across the Main Central Thrust, then progressively decrease to a minimum age at about 27.75°N and increase again in the footwall of the Inner South Tibetan Detachment. Importantly, these trends in cooling ages distribution do not spatially correlate with surface traces of principal faults and shear zones and are interpreted to result from changes in the geometry of the Main Himalayan Thrust underlying the orogenic wedge.
2. Inversions of thermochronologic data using 3-D thermokinematic modeling indicate that the data are compatible with a tectonically driven model in which the basal detachment (Main Himalayan Thrust) is overthrusted by an orogenic wedge for the last 10 Ma. The geometry of the basal detachment consists, from north to south, of three segments: (1) a deep crustal ramp north of 27.5°N, (2) a flat section at ~ 10–15 km depth extending 26.8–27.3°N in the west and 27–27.3°N in the east, and (3) a steep frontal ramp. At first order, these geometries are consistent with the available geophysical data, but in detail, the geometry and kinematics of the MHT may vary along strike between western and eastern Bhutan, in a similar fashion as elsewhere in the Himalaya.
3. We observe significant differences in exhumation rates and patterns between western and eastern Bhutan: In western Bhutan, the slip rates and the partitioning of deformation along the MHT has remained steady during the last 10 Ma, with long-term exhumation rates ranging from 3 mm/yr in the south down to 0.7 mm/yr at 27.25°N and up to 1–1.5 mm/yr north of 27.5°N. In eastern Bhutan, we predict a 40–50% decrease in overthrusting rate at 5–6 Ma. Long-term exhumation rates averaged over the last 10 Ma remain spatially fairly constant with rates of 1–1.5 mm/yr in the south, 0.7 mm/yr along most of the transect,

and 1 mm/yr north of 27.5°N. This local decrease in overthrusting rate may be potentially related to late Miocene to Pliocene changes in the India-southern Eurasia convergence partitioning, with shortening taken up by faults bounding the Shillong Plateau.

4. We suggest that north of the MBT in the Bhutan Himalaya, the geometry and kinematics of the basal detachment is the dominant factor in controlling Neogene upper crustal long-term exhumation rates.
5. Finally, we emphasize that in fold-and-thrust belts soled by a basal detachment with a flat-ramp geometry, exhumational particle paths include significant amount of horizontal displacement within distorted and complex 3-D thermal fields. As a result, cooling and exhumation curves are decoupled even in the shallowest portions of the crust. Currently, inversion of multithermochronometer data sets using 3-D thermal-kinematic modeling is the most appropriate technique to extract geologically meaningful long-term (~10^6 year) upper crustal exhumation rates in such contractional tectonic settings.

Acknowledgments

Fieldwork in Bhutan was enabled by the invaluable help provided by the honorable Jigme Thinley, the Hoch family, L. Hollister, and the Department of Geology and Mines of Bhutan. Stimulating discussions with J. Braun, F. Herman, L. Hollister, D. Kellett, X. Robert, M. Sambridge, and P. van der Beek are greatly appreciated. T. Dumitru and G. Hilley facilitated AFT sample preparation at Stanford University. A. Blythe provided some mineral separates from southwestern Bhutan. Acquisition of the new zircon (U-Th)/He data presented in this study were performed at the University of Arizona and were greatly aided by N. McQuarrie. A thorough and constructive review by M. Fox improved a previous version of the manuscript. This study was supported by the Centre National de la Recherche Scientifique (CNRS, France), the Fulbright Foundation, the France-Stanford Foundation, and the Natural Sciences and Engineering Research Council of Canada (Discovery grant RGPIN 371671).

References

Acton, C. E., K. Priestley, S. Mitra, and V. K. Gaur (2011), Crustal structure of the Darjeeling–Sikkim Himalaya and southern Tibet, *Geophys. J. Int.*, *184*(2), 829–852.

Adams, B. A., K. V. Hodges, M. C. van Soest, and K. X. Whipple (2013), Evidences for Pliocene-Quaternary normal faulting in the hinterland of the Bhutan Himalaya, *Lithosphere*, *5*(4), 438–449.

Adlakha, V., K. A. Lang, R. C. Patel, N. Lal, and K. W. Huntington (2013), Rapid long-term erosion in the rain shadow of the Shillong Plateau, eastern Himalaya, *Tectonophysics*, *582*, 76–83.

Alsdorf, D., L. D. Brown, K. D. Nelson, Y. Makovsky, S. Klemperer, and W. Zhao (1998a), Crustal deformation of the Lhasa terrane, Tibet Plateau from Project INDEPTH deep seismic reflection profiles, *Tectonics*, *17*(4), 501–519.

Alsdorf, D., et al. (1998b), INDEPTH (International Deep Profiling of Tibet and the Himalaya) multichannel seismic reflection data: Description and availability, *J. Geophys. Res.*, *103*(B11), 26,993–926,999.

Avouac, J.-P. (2003), Mountain building, erosion, and the seismic cycle in the Nepal Himalaya, in *Advances in Geophysics*, vol. 60, pp. 1–80, Elsevier, Amsterdam, Netherlands.

Banerjee, P., R. Burgmann, B. Nagarajan, and E. Apel (2008), Intraplate deformation of the Indian subcontinent, *Geophys. Res. Lett.*, *35*, L18301, doi:10.1029/2008GL035468.

Batt, G. E., and M. T. Brandon (2002), Lateral thinking: 2-D interpretation of thermochronology in convergent orogenic settings, *Tectonophysics*, *349*(1-4), 185–201.

Beaumont, C., R. A. Jamieson, M. H. Nguyen, and B. Lee (2001), Himalayan tectonics explained by extrusion of a low-viscosity crustal channel coupled to focused surface denudation, *Nature*, *414*(6865), 738–742.

Beaumont, C., R. A. Jamieson, M. H. Nguyen, and S. Medvedev (2004), Crustal channel flows: 1. Numerical models with applications to the tectonics of the Himalayan-Tibetan orogen, *J. Geophys. Res.*, *109*, B06406, doi:10.1029/2003JB002809.

Bernet, M. (2009), A field-based estimate of the zircon fission-track closure temperature, *Chem. Geol.*, *259*(3), 181–189.

Bernet, M., P. Van Der Beek, R. Pik, P. Huyghe, J.-L. Mugnier, E. Labrin, and A. Szulc (2006), Miocene to recent exhumation of the central Himalaya determined from combined detrital zircon fission-track and U/Pb analysis of Siwalik sediments, western Nepal, *Basin Res.*, *18*(4), 393–412.

Bhattacharyya, K., and G. Mitra (2009), A new kinematic evolutionary model for the growth of a duplex—An example from the Rangit duplex, Sikkim Himalaya, India, *Gondwana Res.*, *16*(3–4), 697–715.

Biswas, S., I. Coutand, D. Grujic, C. Hager, D. Stockli, and B. Grasemann (2007), Exhumation and uplift of the Shillong Plateau and its influence on the eastern Himalayas: New constraints from apatite and zircon (U-Th-[Sm])/He and apatite fission track analyses, *Tectonics*, *26*, TC6013, doi:10.1029/2007TC002125.

Blythe, A. E., D. W. Burbank, A. Carter, K. Schmidt, and J. Putkonen (2007), Plio-Quaternary exhumation history of the central Nepalese Himalaya: 1. Apatite and zircon fission track and apatite [U-Th]/He analyses, *Tectonics*, *26*, TC3002, doi:10.1029/2006TC001990.

Bollinger, L., J.-P. Avouac, O. Beyssac, E. J. Catlos, T. M. Harrison, M. Grove, B. Goffe, and S. Sapkota (2004), Thermal structure and exhumation history of the Lesser Himalaya in central Nepal, *Tectonics*, *23*, TC5015, doi:10.1029/2003TC001564.

Bollinger, L., P. Henry, and J.-P. Avouac (2006), Mountain building in the Nepal Himalaya: Thermal and kinematic model, *Earth Planet. Sci. Lett.*, *244*(1), 58–71.

Bookhagen, B., and D. W. Burbank (2006), Topography, relief, and TRMM-derived rainfall variations along the Himalaya, *Geophys. Res. Lett.*, *33*, L08405, doi:10.1029/2006GL026944.

Bookhagen, B., and D. W. Burbank (2010), Toward a complete Himalayan hydrological budget: Spatiotemporal distribution of snowmelt and rainfall and their impact on river discharge, *J. Geophys. Res.*, *115*, F03019, doi:10.1029/2009JF001426.

Brandon, M. T., M. K. Roden-Tice, and J. I. Garver (1998), Late Cenozoic exhumation of the Cascadia accretionary wedge in the Olympic Mountains, northwest Washington State, *Bull. Geol. Soc. Am.*, *110*, (8), 985–1009.

Braun, J. (2003), Pecube: A new finite-element code to solve the 3D heat transport equation including the effects of a time-varying, finite amplitude surface topography, *Comput.Geosci.*, *29*, 787–794.

Braun, J., and X. Robert (2005), Constraints on the rate of post-orogenic erosional decay from low-temperature thermochronological data: Application to the Dabie Shan, China, *Earth Surf. Processes Landforms*, *30*, 1203–1225, doi:10.1002/esp.1271.

Braun, J., P. Van Der Beek, P. Valla, X. Robert, F. Herman, C. Glotzbach, V. Pedersen, C. Perry, T. Simon-Labric, and C. Prigent (2012), Quantifying rates of landscape evolution and tectonic processes by thermochronology and numerical modeling of crustal heat transport using PECUBE, *Tectonophysics*, *524-525*, 1–28, doi:10.1016/j.tecto.2011.12.035.

Burbank, D. W., A. E. Blythe, J. Putkonen, B. Pratt-Sitaula, E. Gabet, M. Oskin, A. P. Barros, and T. P. Ojha (2003), Decoupling of erosion and precipitation in the Himalayas, *Nature*, *426*, 652–655.

Burchfiel, B. C., and L. H. Royden (1985), North-south extension within the convergent Himalayan region, *Geology*, *13*(10), 679–682.

Burg, J.-P., and G. M. Chen (1984), Tectonics and structural zonation of southern Tibet, China, *Nature*, *311*, 219–223.

Caldwell, W. B., S. L. Klemperer, J. F. Lawrence, and S. S. R. Ashish (2013), Characterizing the Main Himalayan Thrust in the Garhwal Himalaya, India, with receiver function CCP stacking, *Earth Planet. Sci. Lett.*, *367*, 15–27.

Campani, M., F. Herman, and N. Mancktelow (2010), Two- and three-dimensional thermal modeling of a low-angle detachment: Exhumation history of the Simplon Fault Zone, central Alps, *J. Geophys. Res.*, *115*, B10420, doi:10.1029/2009JB007036.
Carosi, R., C. Montomoli, D. Rubatto, and D. Visonà (2006), Normal-sense shear zones in the core of the Higher Himalayan Crystallines (Bhutan Himalaya): Evidence for extrusion?, in *Channel Flow, Ductile Extrusion and Exhumation in Continental Collision Zones*, edited by R. D. Law, M. P. Searle, and L. Godin, pp. 425–444, Geological Society, London, U. K.
Castelli, D., and B. Lombardo (1988), The Gophu La and Western Lunana granites: Miocene muscovite leucogranites of the Bhutan Himalaya, *Lithos*, *21*(3), 211–225.
Célérier, J., T. M. Harrison, O. Beyssac, F. Herman, W. J. Dunlap, and A. A. G. Webb (2009), The Kumaun and Garwhal Lesser Himalaya, India: Part 2. Thermal and deformation histories, *Geol. Soc. Am. Bull.*, *121*(9–10), 1281–1297.
Chakungal, J. (2006), Geochemistry and Metamorphism of Metabasites, and Spatial Variation of P-T Paths across the Bhutan Himalaya: Implications for the Exhumation of the Greater Himalayan Sequence, 169 pp., Dalhousie, Halifax, Canada.
Chambers, J., R. Parrish, T. Argles, N. Harris, and M. Horstwood (2011), A short-duration pulse of ductile normal shear on the outer South Tibetan detachment in Bhutan: Alternating channel flow and critical taper mechanics of the eastern Himalaya, *Tectonics*, *30*, TC2005, doi:10.1029/2010TC002784.
Chirouze, F., P. Huyghe, P. van der Beek, C. Chauvel, T. Chakraborty, G. Dupont-Nivet, and M. Bernet (2013), Tectonics, exhumation, and drainage evolution of the eastern Himalaya since 13 Ma from detrital geochemistry and thermochronology, Kameng River section, Arunachal Pradesh, *Geol. Soc. Am. Bull.*, *125*(3–4), 523–538.
Clark, M. K., and R. Bilham (2008), Miocene rise of the Shillong Plateau and the beginning of the end for the eastern Himalaya, *Earth Planet. Sci. Lett.*, *269*(3), 337–351, doi:10.1016/j.epsl.2008.01.045.
Corrie, S. L., M. J. Kohn, N. McQuarrie, and S. P. Long (2012), Flattening the Bhutan Himalaya, *Earth Planet. Sci. Lett.*, *349-350*, 67–74.
Coward, M. P., and R. W. H. Butler (1985), Thrust tectonics and the deep-structure of the Pakistan Himalaya, *Geology*, *13*(6), 417–420.
Daniel, C. G., L. S. Hollister, R. R. Parrish, and D. Grujic (2003), Exhumation of the Main Central Thrust from lower crustal depths, eastern Bhutan Himalaya, *J. Metamorph. Geol.*, *21*(4), 317–334.
Davidson, C., D. Grujic, L. S. Hollister, and S. M. Schmid (1997), Metamorphic reactions related to decompression and synkinematic intrusion of leucogranite High Himalayan Crystallines, Bhutan, *J. Metamorph. Geol.*, *15*, 593–612.
DeCelles, P. G., G. E. Gehrels, J. Quade, T. P. Ojha, P. A. Kapp, and B. N. Upreti (1998), Neogene foreland basin deposits, erosional unroofing, and the kinematic history of the Himalayan fold-thrust belt, western Nepal, *Geol. Soc. Am. Bull.*, *110*(1), 2–21.
DeCelles, P. G., D. M. Robinson, J. Quade, T. P. Ojha, C. N. Garzione, P. Copeland, and B. N. Upreti (2001), Stratigraphy, structure, and tectonic evolution of the Himalayan fold-thrust belt in western Nepal, *Tectonics*, *20*(4), 487–509.
Donelick, R. A., P. B. O'Sullivan, and R. A. Ketcham (2005), Apatite fission-track analysis, *Rev. Mineral. Geochem.*, *58*(1), 49–94.
Edwards, M. A., and T. M. Harrison (1997), When did the roof collapse? Late Miocene north-south extension in the high Himalaya revealed by Th-Pb monazite dating of the Khula Kangri granite, *Geology*, *25*(6), 543–546.
Edwards, M. A., W. S. F. Kidd, J. Li, Y. Yue, and M. Clark (1996), Multi-stage development of the southern Tibet detachment system near Khula Kangri. New data from Gonto La, *Tectonophysics*, *260*(1), 1–19.
Edwards, M. A., A. Pêcher, W. S. F. Kidd, B. C. Burchfiel, and L. H. Royden (1999), Southern Tibet Detachment System at Khula Kangri, eastern Himalaya: A large-area, shallow detachment stretching into Bhutan?, *J. Geol.*, *107*(5), 623–631.
Ehlers, T. A. (2005), Crustal thermal processes and the interpretation of thermochronometer data, *Rev. Mineral. Geochem.*, *58*(1), 315–350.
Farley, K. A., and D. F. Stockli (2002), (U-Th)/He dating of phosphates: Apatite, monazite, and xenotime, *Rev. Mineral. Geochem.*, *48*(1), 559–577.
Farr, T. G., et al. (2007), The Shuttle Radar Topographic Mission, *Rev. Geophys.*, *45*, RG2004, doi:10.1029/2005RG000183.
Galy, V., C. France-Lanord, B. Peucker-Ehrenbrink, and P. Huyghe (2010), Sr-Nd-Os evidence for a stable erosion regime in the Himalaya during the past 12 Myr, *Earth Planet. Sci. Lett.*, *290*, 474–480.
Gansser, A. (1964), *Geology of the Himalayas*, pp. 289, Interscience Publishers, London and New York.
Gansser, A. (1983), *Geology of the Bhutan Himalaya*, pp. 181, Birkhaüser, Verlag, Germany.
Green, P. F., I. R. Duddy, A. J. W. Gleadow, and P. R. Tingate (1985), Fission track annealing in apatite: Track length measurements and the form of the Arrhenius plot, *Nucl. Tracks Radiat. Meas.*, *10*, 323–328.
Grujic, D. (2006), Channel flow and continental collision tectonics: An overview, in *Channel Flow, Ductile Extrusion and Exhumation in Continental Collision Zones*, edited by R. D. Law, M. P. Searle, and L. Godin, pp. 25–37, Geological Society Special Publications, London.
Grujic, D., M. Casey, C. Davidson, L. S. Hollister, R. Ktindig, T. Pavlis, and S. Schmid (1996), Ductile extrusion of the Higher Himalayan crystalline in Bhutan: Evidence from quartz microfabrics, *Tectonophysics*, *260*, 21–43.
Grujic, D., L. S. Hollister, and R. R. Parrish (2002), Himalayan metamorphic sequence as an orogenic channel: Insight from Bhutan, *Earth Planet. Sci. Lett.*, *198*, 177–191.
Grujic, D., I. Coutand, B. Bookhagen, S. Bonnet, A. Blythe, and C. Duncan (2006), Climatic forcing of erosion, landscape, and tectonics in the Bhutan Himalayas, *Geology*, *34*(10), 801–804, doi:10.1130/G22648.1.
Grujic, D., C. J. Warren, and J. L. Wooden (2011), Rapid synconvergent exhumation of Miocene-aged lower orogenic crust in the eastern Himalaya, *Lithosphere*, *3*(5), 346–366, doi:10.1130/L154.1.
Hauck, M. L., K. D. Nelson, L. D. Brown, W. Zhao, and A. R. Ross (1998), Crustal structure of the Himalayan orogen at ~ 90 east longitude from Project INDEPTH deep reflection profiles, *Tectonics*, *17*(4), 481–500.
Herman, F., J. Braun, and W. J. Dunlap (2007), Tectonomorphic scenarios in the Southern Alps of New Zealand, *J. Geophys. Res.*, *112*, B04201, doi:10.1029/2004JB003472.
Herman, F., et al. (2010), Exhumation, crustal deformation, and thermal structure of the Nepal Himalaya derived from the inversion of thermochronological and thermobarometric data and modeling of the topography, *J. Geophys. Res.*, *115*, B06407, doi:10.1029/2008JB006126.
Hirn, A., et al. (1984), Crustal structure and variability of the Himalayan border of Tibet, *Nature*, *307*, 23–25.
Hirschmiller, J., D. Grujic, B. Bookhagen, I. Coutand, P. Huyghe, J.-L. Mugnier, and T. Ojha (2014), What controls the growth of the Himalayan fold-and-thrust belt?, *Geology*, 1, G35057.
Hodges, K. (2000), Tectonics of the Himalaya and southern Tibet from two perspectives, *Bull. Geol. Soc. Am.*, *112*(3), 324–350.
Hodges, K. V., C. Wobus, K. Ruhl, T. Schildgen, and K. Whipple (2004), Quaternary deformation, river steepening, and heavy precipitation at the front of the Higher Himalayan Ranges, *Earth Planet. Sci. Lett.*, *220*, 379–389.
Hollister, L. S., and D. Grujic (2006), Pulsed channel flow in Bhutan, in *Channel Flow, Ductile Extrusion and Exhumation in Continental Collision Zones*, edited by R. D. Law, M. P. Searle, and L. Godin, pp. 415–423, Geological Society Special Publications, London, U. K.
Huntington, K. W., A. E. Blythe, and K. V. Hodges (2006), Climate change and late Pliocene acceleration of erosion in the Himalaya, *Earth Planet. Sci. Lett.*, *252*(1), 107–118, doi:10.1016/j.epsl.2006.09.031.

Huntington, K. W., T. A. Ehlers, K. V. Hodges, and D. M. Whipp Jr. (2007), Topography, exhumation pathway, age uncertainties, and the interpretation of thermochronometer data, *Tectonics*, *26*, TC4012, doi:10.1029/2007TC002108.
Jade, S. (2004), Estimates of plate velocity and crustal deformation in the Indian subcontinent using GPS geodesy, *Curr. Sci.*, *86*(10), 1443–1448.
Jade, S., et al. (2007), Estimates of interseismic deformation in Northeast India from GPS measurements, *Earth Planet. Sci. Lett.*, *263*(3), 221–234, doi:10.1016/j.epsl.2007.08.031.
Jamieson, R. A., C. Beaumont, S. Medvedev, and M. H. Nguyen (2004), Crustal channel flows: 2 Numerical models with implications for metamorphism in the Himalayan-Tibetan orogen, *J. Geophys. Res.*, *109*, B06407, doi:10.1029/2003JB002811.
Jamieson, R. A., C. Beaumont, M. H. Nguyen, and D. Grujic (2006), Provenance of the Greater Himalayan Sequence and associated rocks: Predictions of channel flow models, in *Channel Flow, Ductile Extrusion and Exhumation in Continental Collision Zones*, edited by R. D. Law, M. P. Searle, and L. Godin, pp. 165, Geological Society Special Publications, London, U. K.
Kellett, D. A., D. Grujic, and S. Erdmann (2009), Miocene structural reorganization of the South Tibetan detachment, eastern Himalaya: Implications for continental collision, *Lithosphere*, *1*(5), 259–281.
Kellett, D. A., D. Grujic, C. Warren, J. Cottle, R. A. Jamieson, and T. Tenzin (2010), Metamorphic history of a syn-convergent orogen-parallel detachment: The South Tibetan detachment system, Bhutan Himalaya, *J. Metamorph. Geol.*, *28*(8), 785–808, doi:10.1111/j.1525-1314.2010.00893.x.
Kellett, D. A., D. Grujic, I. Coutand, J. Cottle, and M. Mukul (2013), The South Tibetan detachment system facilitates ultra rapid cooling of granulite-facies rocks in Sikkim Himalaya, *Tectonics*, *32*, 1–28, doi:10.1002/tect.20014.
Ketcham, R. A., R. A. Donelick, and W. D. Carlson (1999), Variability of apatite fission-track annealing kinetics; III Extrapolation to geological time scales, *Am. Mineral.*, *84*, 1235–1255.
Lave, J., and J.-P. Avouac (2000), Active folding of fluvial terraces across the Siwaliks Hills, Himalayas of central Nepal, *J. Geophys. Res.*, *105*(B3), 5735–5770.
Le Fort, P. (1975), Himalayas: The collided range. Present knowledge of the continental arc, *Am. J. Sci.*, *275*(A), 1–44.
Lee, J., B. R. Hacker, W. S. Dinklage, Y. Wang, P. Gans, A. Calvert, J. Wan, W. Chen, A. E. Blythe, and W. McClelland (2000), Evolution of the Kangmar Dome, southern Tibet: Structural, petrologic, and thermochronologic constraints, *Tectonics*, *19*(5), 872–895.
Long, S., N. McQuarrie, T. Tobgay, and D. Grujic (2011a), Geometry and crustal shortening of the Himalayan fold-thrust belt, eastern and central Bhutan, *Geol. Soc. Am. Bull.*, *123*(7/8), 1427–1447, doi:10.1130/B30203.1.
Long, S., N. McQuarrie, T. Tobgay, and J. Hawthorne (2011b), Quantifying internal strain and deformation temperature in the eastern Himalaya, Bhutan: Implications for the evolution of strain in thrust sheets, *J. Struct. Geol.*, *33*(4), 579–608.
Long, S., N. McQuarrie, T. Tobgay, I. Coutand, F. J. Cooper, P. W. Reiners, J.-A. Wartho, and K. V. Hodges (2012), Variable shortening rates in the eastern Himalayan thrust belt, Bhutan: Insights from multiple thermochronologic and geochronologic data sets tied to kinematic reconstructions, *Tectonics*, *31*, TC5004, doi:10.1029/2012TC003155.
Loveless, J. P., and B. J. Meade (2011), Partitioning of localized and diffuse deformation in the Tibetan Plateau from joint inversions of geologic and geodetic observations, *Earth Planet. Sci. Lett.*, *303*(1–2), 11–24, doi:10.1016/j.epsl.2010.12.014.
Makovsky, Y., S. L. Klemperer, H. Liyan, L. Deyuan, and P. I. Team (1996), Structural elements of the southern Tethyan Himalaya crust from wide-angle seismic data, *Tectonics*, *15*(5), 997–1005.
Makovsky, Y., S. L. Klemperer, L. Ratschbacher, and D. Alsdorf (1999), Midcrustal reflector on INDEPTH wide-angle profiles: An ophiolitic slab beneath the India-Asia suture in southern Tibet?, *Tectonics*, *18*(5), 793–808.
Maluski, H., P. Matte, M. Brunel, and X. Xiao (1988), Argon 39-Argon 40 dating of metamorphic and plutonic events in the North and High Himalaya belts (southern Tibet-China), *Tectonics*, *7*(2), 299–326, doi:10.1029/TC007i002p00299.
Mancktelow, N. S., and B. Grasemann (1997), Time-dependent effects of heat advection and topography on cooling histories during erosion, *Tectonophysics*, *270*(3), 167–195.
McQuarrie, N., D. Robinson, S. Long, T. Tobgay, D. Grujic, G. Gehrels, and M. Ducea (2008), Preliminary stratigraphic and structural architecture of Bhutan: Implications for the along strike architecture of the Himalayan system, *Earth Planet. Sci. Lett.*, *272*(1), 105–117.
McQuarrie, N., T. Tobgay, S. P. Long, P. W. Reiners, and M. A. Cosca (2014), Variable exhumation rates and variable displacement rates: Documenting a recent slowing of Himalayan shortening in western Bhutan, *Earth Planet. Sci. Lett.*, *286*, 161–174, doi:10.1016/j.epsl.2013.10.045, in press.
Meyer, M. C., G. Wiesmayr, M. Brauner, H. Häusler, and D. Wangda (2006), Active tectonics in Eastern Lunana (NW Bhutan): Implications for the seismic and glacial hazard potential of the Bhutan Himalaya, *Tectonics*, *25*, TC3001, doi:10.1029/2005TC001858.
Mitra, S., K. Priestley, A. K. Bhattacharyya, and V. K. Gaur (2005), Crustal structure and earthquake focal depths beneath northeastern India and southern Tibet, *Geophys. J. Int.*, *160*(1), 227–248, doi:10.1111/j.1365-246X.2004.02470.x.
Mitra, G., K. Bhattacharyya, and M. Mukul (2010), The Lesser Himalayan duplex in Sikkim: Implications for variations in Himalayan shortening, *J. Geol. Soc. India*, *75*(1), 289–301.
Molnar, P., and J. M. Stock (2009), Slowing of India's convergence with Eurasia since 20 Ma and its implications for Tibetan mantle dynamics, *Tectonics*, *28*, TC3001, doi:10.1029/2008TC002271.
Nábělek, J., G. Hetényi, J. Vergne, S. Sapkota, B. Kafle, M. Jiang, H. Su, J. Chen, B.-S. Huang, and H.-C. Team (2009), Underplating in the Himalaya-Tibet collision zone revealed by the Hi-CLIMB experiment, *Science*, *325*(5946), 1371–1374.
Naito, N., Y. Ageta, S. Iwata, Y. Matsuda, R. Suzuki, Karma, and H. Yabuki (2006), Glacier shrinkages and climate conditions around Jichu Dramo Glacier in the Bhutan Himalayas from 1998 to 2003, *Bull. Glaciol. Res.*, *23*, 51–61.
Nelson, K. D., et al. (1996), Partially molten middle crust beneath southern Tibet: Synthesis of project INDEPTH results, *Science*, *274*, 1684–1688.
Paul, J., et al. (2001), The motion and active deformation of India, *Geophys. Res. Lett.*, *28*(4), 647–650.
Reiners, P. W. (2005), Zircon (U-Th)/He thermochronometry, *Rev. Mineral. Geochem.*, *58*(1), 151–179.
Reiners, P. W., and M. T. Brandon (2006), Using thermochronology to understand orogenic erosion, *Ann. Rev. Earth Planet. Sci.*, *34*(1), 419–466.
Reiners, P. W., T. A. Ehlers, S. G. Mitchell, and D. R. Montgomery (2003), Coupled spatial variations in precipitation and long-term erosion rates across the Washington Cascades, *Nature*, *426*, 645–647.
Rickwood, P., and M. Sambridge (2006), Efficient parallel inversion using the Neighbourhood Algorithm, *Geochem. Geophys. Geosyst.*, *7*, Q11001, doi:10.1029/2006GC001246.
Robert, X., P. van der Beek, J. Braun, C. Perry, M. Dubille, and J.-L. Mugnier (2009), Assessing Quaternary reactivation of the Main Central Thrust zone (central Nepal Himalaya): New thermochronologic data and numerical modeling, *Geology*, *37*(8), 731–734, doi:10.1130/G25736A.1.
Robert, X., P. Van Der Beek, J. Braun, C. Perry, and J.-L. Mugnier (2011), Control of detachment geometry on lateral variations in exhumation rates in the Himalaya: Insights from low-temperature thermochronology and numerical modeling, *J. Geophys. Res.*, *116*, B05202, doi:10.1029/2010JB007893.

Sambridge, M. (1999a), Geophysical inversion with a neighbourhood algorithm—I. Searching a parameter space, *Geophys. J. Int.*, *138*, 479–494.
Sambridge, M. (1999b), Geophysical inversion with a neighbourhood algorithm—II. Appraising the ensemble, *Geophys. J. Int.*, *138*(3), 727–746.
Schelling, D., and K. Arita (1991), Thrust tectonics, crustal shortening, and the structure of the far-eastern Nepal Himalaya, *Tectonics*, *10*(5), 851–862.
Schulte-Pelkum, V., G. Monsalve, A. Sheehan, M. R. Pandey, S. Sapkota, R. Bilham, and F. Wu (2005), Imaging the Indian subcontinent beneath the Himalaya, *Nature*, *435*, 1222–1225.
Shuster, D. L., R. M. Flowers, and K. A. Farley (2006), The influence of natural radiation damage on helium diffusion kinetics in apatite, *Earth Planet. Sci. Lett.*, *249*(3–4), 148–161.
Srivastava, P., and G. Mitra (1994), Thrust geometries and deep structure of the outer and lesser Himalaya, Kumaon and Garhwal (India): Implications for evolution of the Himalayan fold-and-thrust belt, *Tectonics*, *13*(1), 89–109.
Streule, M. J., A. Carter, M. P. Searle, and J. M. Cottle (2012), Constraints on brittle field exhumation of the Everest-Makalu section of the Greater Himalayan Sequence: Implications for models of crustal flow, *Tectonics*, *31*, TC3010, doi:10.1029/2011TC003062.
Stüwe, K., and D. Foster (2001), 40Ar/39Ar, pressure, temperature and fission track constraints on the age and nature of metamorphism around the main central thrust in the eastern Bhutan Himalaya, *J. Asian Earth Sci.*, *19*, 85–95.
Stüwe, K., and M. Hintermüller (2000), Topography and isotherms revisited: The influence of laterally migrating drainage divides, *Earth Planet. Sci. Lett.*, *184*(1), 287–303.
Swapp, S. M., and L. S. Hollister (1991), Inverted metamorphism within the Tibetan slab of Bhutan: Evidence for a tectonically transported heat-source, *Can. Mineral.*, *29*, 1019–1041.
Thiede, R. C., B. Bookhagen, J. R. Arrowsmith, E. R. Sobel, and M. R. Strecker (2004), Climatic control on rapid exhumation along the Southern Himalayan Front, *Earth Planet. Sci. Lett.*, *222*(3), 791–806.
Thiede, R. C., J. R. Arrowsmith, B. Bookhagen, M. O. McWilliams, E. R. Sobel, and M. R. Strecker (2005), From tectonically to erosionally controlled development of the Himalayan orogen, *Geology*, *33*(8), 689–692.
Thiede, R. C., T. A. Ehlers, B. Bookhagen, and M. R. Strecker (2009), Erosional variability along the northwest Himalaya, *J. Geophys. Res.*, *114*, F01015, doi:10.1029/2008JF001010.
Tobgay, T., N. McQuarrie, S. Long, M. J. Kohn, and S. L. Corrie (2012), The age and rate of displacement along the Main Central Thrust in the western Bhutan Himalaya, *Earth Planet. Sci. Lett.*, *319-320*, 146–158, doi:10.1016/j.epsl.2011.12.005.
Valla, P., F. Herman, P. A. van der Beek, and J. Braun (2010), Inversion of thermochronological age-elevation profiles to extract independent estimates of denudation and relief history—I: Theory and conceptual model, *Earth Planet. Sci. Lett.*, *295*, 511–522, doi:10.1016/j.epsl.2010.04.033.
Vermeesch, P. (2004), How many grains are needed for a provenance study?, *Earth Planet. Sci. Lett.*, *224*(3–4), 441–451, doi:10.1016/j.epsl.2004.05.037.
Warren, C. J., D. Grujic, J. M. Cottle, and N. W. Rogers (2011a), Constraining cooling histories: Rutile and titanite chronology and diffusion modelling in NW Bhutan, *J. Metamorph. Geol.*, *30*(2), 113–130, doi:10.1111/j.1525-1314.2011.00958.x.
Warren, C. J., D. Grujic, D. A. Kellett, J. Cottle, R. A. Jamieson, and K. S. Ghalley (2011b), Probing the depths of the India-Asia collision: U-Th-Pb monazite chronology of granulites from NW Bhutan, *Tectonics*, *30*, TC2004, doi:10.1029/2010TC002738.
Whipp, D. M., Jr., T. A. Ehlers, A. E. Blythe, K. W. Huntington, K. V. Hodges, and D. W. Burbank (2007), Plio-Quaternary exhumation history of the central Nepalese Himalaya: 2. Thermokinematic and thermochronometer age prediction model, *Tectonics*, *26*, TC3003, doi:10.1029/2006TC001991.
Whipp, D. M., Jr., T. A. Ehlers, J. Braun, and C. D. Spath (2009), Effects of exhumation kinematics and topographic evolution on detrital thermochronometer data, *J. Geophys. Res.*, *114*, F04021, doi:10.1029/2008JF001195.
Whipple, K. X. (2009), The influence of climate on the tectonic evolution of mountain belts, *Nat. Geosci.*, *2*(2), 97–104, doi:10.1038/ngeo413.
Wiesmayr, G., M. A. Edwards, M. Meyer, W. Kidd, D. Leber, H. Häusler, and D. Wangda (2002), Evidence for steady fault-accommodated strain in the High Himalaya: Progressive fault rotation of the southern Tibet detachment system in NW Bhutan, *Geol. Soc. London Spec. Publications*, *200*(1), 371–386.
Wobus, C. W., K. V. Hodges, and K. X. Whipple (2003), Has focused denudation sustained active thrusting at the Himalayan topographic front?, *Geology*, *31*(10), 861–864.
Wobus, C., M. Pringle, K. Whipple, and K. Hodges (2008), A late Miocene acceleration of exhumation in the Himalayan crystalline core, *Earth Planet. Sci. Lett.*, *269*(1), 1–10, doi:10.1016/j.epsl.2008.02.019.
Wu, C., K. D. Nelson, G. Wortman, S. D. Samson, Y. Yue, J. Li, W. S. F. Kidd, and M. A. Edwards (1998), Yadong cross structure and South Tibetan Detachment in the east central Himalaya (89°–90°E), *Tectonics*, *17*(1), 28–45.
Yin, A., C. S. Dubey, T. K. Kelty, A. A. G. Webb, T. M. Harrison, C. Y. Chou, and J. Célérier (2010), Geologic correlation of the Himalayan orogen and Indian craton: Part 2. Structural geology, geochronology, and tectonic evolution of the Eastern Himalaya, *Geol. Soc. Am. Bull.*, *122*, 360–395, doi:10.1130/B26461.1.
Zhao, W., K. D. Nelson, J. Che, J. Quo, D. Lu, and C. Wu (1993), Deep seismic reflection evidence for continental underthrusting beneath southern Tibet, *Nature*, *366*, 557–559.

Supporting Informations Paper 2013JB010891

Geometry and kinematics of the Main Himalayan Thrust and Neogene crustal exhumation in the Bhutanese Himalaya derived from inversion of multi-thermochronologic data

Isabelle Coutand, Department of Earth Sciences, Dalhousie University, Halifax, Nova Scotia, Canada, icoutand@da.ca

David M. Whipp Jr., Institute of Seismology, Department of Geosciences and Geography, University of Helsinki, Helsinki, Finland

Djordje Grujic, Department of Earth Sciences, Dalhousie University, Halifax, Nova Scotia, Canada

Matthias Bernet, Institut des Sciences de la Terre, Université Joseph Fourier, Grenoble, France

Maria Giuditta Fellin, Institute for Geochemistry and Petrology, Sonneggstrasse 5 8092, ETH-Zürich, Zürich, SWITZERLAND

Bodo Bookhagen, Department of Geography, University of California, Santa Barbara, California, USA

Kyle R. Landry, Department of Earth Sciences, Dalhousie University, Halifax, Nova Scotia, Canada

S. K. Ghalley, Department of Geology and Mines, Ministry of Economic Affairs, Thimphu, Bhutan

Chris Duncan, Department of Geosciences, University of Massachusetts Amherst, Amherst, Massachusetts, USA

Readme

The auxiliary material comprises one (1) text file including 7 appendices including 2 tables and 2 figures. Hereafter, we describe in detail the content of each appendix.

1.1 Appendix A – contains Table S1 displaying informations about the bedrock samples that were analyzed in this study. Hereafter, we detail the content of the table.

1.1.2 Column "sample", no unit, name of the samples used in this study.

1.1.3 Column "Unit", no unit, name of the tectonic unit in which the samples were collected.

1.1.4 Column "Longitude", degrees, longitude of samples east of Greenwich.

1.1.5 Column "Latitude" degrees, latitude of samples, north of equator.

1.1.6 Column "Elev.", meters, elevation of the samples with respect to sea-level.

1.1.7 Column "AHe", no unit, displays the samples dated using the method (U-Th)/He on apatite crystals. Signs in the columns are: x: no analysis available; 1: data from this study; 2: data from [*Grujic et al.*, 2006]; 3: data from [*Long et al.*, 2012]; 4: data from [*McQuarrie et al.*, 2014].

1.1.8 Column "AFT", no unit, displays the samples dated using the method fission-track on apatite crystals. Signs in the columns are: x: no analysis available; 1: data from this study; 2: data from [*Grujic et al.*, 2006]; 3: data from [*Long et al.*, 2012]; 4: data from [*McQuarrie et al.*, 2014].

1.1.9 Column "ZHe", no unit, displays the samples dated using the method (U-Th)/He on zircon crystals. Signs in the columns are: x: no analysis available; 1: data from this study; 2: data from [*Grujic et al.*, 2006]; 3: data from [*Long et al.*, 2012]; 4: data from [*McQuarrie et al.*, 2014].

1.1.10 Column "ZFT", no unit, displays the samples dated using the method fission-track on zircon crystals. Signs in the columns are: x: no analysis available; 1: data from this study; 2: data from [*Grujic et al.*, 2006]; 3: data from [*Long et al.*, 2012]; 4: data from [*McQuarrie et al.*, 2014].

1.2 Appendix B

Describes the analytical procedure of apatite (U-Th)/He thermochronology that we used in this study. Data were acquired both at Dalhousie University and at ETH-Zürich during the last two years. Each step of the data acquisition is described in details in this text section.

1.3. Appendix C

Describes the analytical procedure of zircon (U-Th)/He thermochronology that we used in this study. Data were acquired at the University of Arizona during the last two years. Each step of the data acquisition is described in details in *Long et al* [2012] and we refer to that paper instead of repeating their detailed description of the procedure.

In the main body of our paper, we present 5 new ages. In this section of the auxiliary material, we list in Table S2 zircon (U-Th)/He ages previously published that we use in our numerical modeling. We do so because for these ages, we have recalculated the errors using a standard error approach on single-grain ages where the standard deviation of the age population is divided by the square root of the number of data. This error takes into account the dispersion of the single-grain ages, which is commonly larger than analytical errors previously displayed for these data. Hereafter, we detail the content of Table S2 listing samples by *Long et al* [2012] and [*McQuarrie et al.*, 2014].

1.3.1 Column “samples”, no unit, name of each aliquot.

1.3.2 Column “Corrected Age”, million years, ages as provided by authors cited above.

1.3.3 Column “Mean Age”, million years, mean age of the different aliquots.

1.3.4 Column “Error”, million years, errors using a standard error approach on single-grain ages where the standard deviation of the age population is divided by the square root of the number of data.

1.4 Appendix D

Describes the analytical procedure of apatite fission-track thermochronology that we used in this study. Data were acquired both at Stanford and Dalhousie University during the last five years. Each step of the data acquisition is described in details in this text section.

1.5 Appendix E

Describes the analytical procedure of zircon fission-track thermochronology that we used in this study. Data were acquired at Université Joseph Fourier (Grenoble, France) three years ago. Each step of the data acquisition is described in details in this text section.

1.6 Appendix F

This section contains Figure S1 and describes the implementation of topographic advection in our models.

1.7 Appendix G

This section displays correlation matrices of the models parameters under the form of Figure S2.

Supporting Information, Data Set S1

Appendix A

Table S1. List and location of rock samples and thermochronologic data

Sample	Unit	Longitude (°E)	Latitude (°N)	Elev. (m)	AHe	AFT	ZHe	ZFT
BH38	Jaishidanda Fm. (Gneiss)	91.14425	27.54036	2135	x	1	3	x
BH39	Jaishidanda Fm. (Quartzite)	91.15983	27.54231	2139	1	x	x	x
BH52	GHS (Augengneiss)	91.55467	27.23606	2350	x	2	x	x
BH53	GHS (Augengneiss)	91.54808	27.23736	2405	1	2	x	x
BH57	LHS (Quartzite)	91.44656	27.27869	604	x	x	3	x
BH60	GHS (Augengneiss)	91.48067	27.28236	795	1	2	x	x
BH61	GHS (Migmatite)	91.49100	27.30342	780	x	2	x	x
BH63	GHS (Gneiss)	91.51898	27.31485	672	1	1	x	x
BH64	GHS (Migmatite)	91.55447	27.35006	825	x	1	x	x
BH66	GHS (Gneiss)	91.56114	27.55136	930	x	2	x	x
BH70	GHS (Augengneiss)	91.49953	27.58417	1760	1	2	x	x
BH72	GHS (Migmatite)	91.55472	27.46500	1420	x	2	x	x
BH90	GHS (Leucogranite)	91.57453	27.34497	910	x	2	x	x
BH94	GHS (Leucogranite)	91.59983	27.37533	2050	x	2	x	x
BH100	GHS (Leucogranite)	91.56372	27.41139	905	x	2	x	x
BH100/2	GHS (Migmatite)	91.15389	27.30881	1720	x	2	x	x
BH101	GHS (Augengneiss)	91.10072	27.34133	2380	1	2	3	x
BH109	Jaishidanda Fm. (Schist)	89.39972	27.44222	2400	1	2	4	x
BH111b	Jaishidanda Fm. (Schist)	89.42323	27.44900	2283	1	x	x	x
BH161	GHS (Migmatite)	89.51372	28.02333	4086	1	1	x	x
BH163	GHS (Migmatite)	89.58878	28.06583	4177	1	1	x	x
BH164	GHS (Leucogranite)	89.60957	28.06222	4248	x	1	x	x
BH171	GHS (Migmatite)	89.77081	27.69294	1440	x	2	x	x
BH211	GHS (Augengneiss)	89.80578	28.17140	4400	1	1	1	x
BH260	GHS (Migmatite)	89.72220	28.07293	3773	x	x	1	x
BH284	GHS (Quartzite)	89.72347	28.14491	4189	1	1	x	x
BH287	GHS (Marbble)	89.68955	28.10946	3874	1	x	x	x
BH324	GHS (Migmatite)	91.59683	27.37436	1995	x	2	x	x
BH339	LHS (Gneiss)	91.32806	27.30460	2026	x	1	x	x
BH342	LHS (Gneiss)	91.29907	27.26742	2219	x	1	3	x
BH351	GHS (Leucogranite)	91.30357	27.97318	3870	x	1	x	x
BH352	GHS (gneiss)	91.29016	27.97416	3880	1	1	x	1
BH355	GHS (Leucogranite)	91.29870	27.99005	4275	x	1	x	x
BH357	GHS (Gneiss)	91.29827	27.98563	4085	1	1	1	x
BH362	GHS (Leucogranite)	91.29901	27.99750	4300	1	1	x	x
BH363	GHS (Leucogranite)	91.37263	27.96956	3610	x	1	x	x
BH378	GHS (Gneiss)	91.20487	27.66549	1180	1	1	3	1
BH380	GHS (Leucogranite)	91.23065	27.26965	2150	x	1	x	1
BH406	GHS (Migmatite)	89.82001	27.52181	1700	x	1	1	1
BH408	GHS (Micaschist)	89.75380	27.50177	2625	x	1	x	1
BH409	GHS (Gneiss)	89.76088	27.48373	2910	1	1	x	1
BH411	GHS (Migmatite)	89.41996	27.46156	2339	x	1	4	1
BH412	GHS (Gneiss)	89.41937	27.45803	2480	1	1	x	1
BH413	Jaishidanda Fm. (Quartzite)	89.47229	27.34339	2320	x	1	4	1
BH415	GHS (Migmatite)	89.74973	27.49078	3123	x	1	4	1

Table S1. Continued

BH416	GHS (Augengneiss)	89.72231	27.47863	2640	x	1	x	x
BH417	GHS (Gneiss)	89.69500	27.44078	2640	1	1	x	x
BH424	Jaishidanda Fm. (Quartzite)	89.42762	27.38741	2500	x	1	4	1
BH426	Jaishidanda Fm. (Quartzite)	89.37143	27.37223	3390	x	1	x	1
BH428	Jaishidanda Fm. (Quartzite)	89.84515	27.37700	3675	x	x	x	1
BH430	Jaishidanda Fm. (Leucogranite dyke in quartzite)	89.34159	27.37169	3970	x	1	x	x
BH431	Jaishidanda Fm. (Calc-	89.31352	27.37272	3600	x	1	x	x
BH436	GHS (Migmatite)	89.55313	27.07518	2230	1	1	x	x
BH437	GHS (Migmatite)	89.55054	27.13060	2550	1	1	x	x
BH438	Jaishidanda Fm. (Micaschist)	89.54089	27.15421	2470	1	1	x	x
BH651	GHS (Leucogranite)	89.29044	27.69862	3540	x	1	x	x
BH683	GHS (Augengneiss)	89.51613	27.97138	4400	x	1	x	x
BH686	GHS (Gneiss)	89.55855	28.03493	5008	x	1	x	x
BH687	GHS (Gneiss)	89.56281	28.04786	4720	x	1	x	x
BH689	GHS (Migmatite)	89.58826	28.06487	4145	1	1	x	x
BH695	GHS (Migmatite)	89.62974	28.06862	3795	x	1	x	x
02-102F	02-102F	89.54850	27.31460	2116	1	1	x	x
02-104F	02-104F	89.76260	27.49077	2852	1	x	x	x
02-232F	02-232F	89.80645	27.78538	3086	x	1	x	x
02-235F	02-235F	89.74823	27.73522	1669	1	1	x	x
BHF01a	LHS (Schist)	89.40906	26.86218	650	x	1	4	x
BHF01b	LHS (Schist)	89.40906	26.86218	701	x	1	x	x
BHF02	LHS	89.43518	26.89151	1250	x	1	x	x
BHF04	GHS (Augengneiss)	89.45933	26.90723	1751	1	1	4	x
BHF05	GHS (Gneiss)	89.57415	27.02737	1864	1	1	1	x
BHF06	GHS (Gneiss)	89.55721	27.06583	1539	x	1	x	x
BHF07	Jaishidanda Fm. (Micaschist)	89.55243	27.18909	2153	x	1	4	x
F08	GHS (Gneiss)	89.74884	27.49029	3113	1	2	x	x
F09	GHS (Amphibolite)	89.79600	27.51240	1953	1	2	x	x
S17	Jaishidanda Fm. (Schist)	89.69520	27.44172	2524	x	2	x	x
BU07-6	Jaishidanda Fm. (Quartzite)	91.21519	27.59367	1170	x	x	3	x
BU07-9	LHS (Quartzite)	91.18111	27.40256	930	x	x	3	x
BU07-11	LHS (Orthogneiss)	91.19339	27.39969	840	x	3	3	x
BU07-12	LHS (Quartzite)	91.20289	27.27808	995	x	3	3	x
BU07-13	LHS (Quartzite)	91.23342	27.18844	645	x	x	3	x
BU07-14	LHS (Quartzite)	91.24000	27.16608	600	x	x	3	x
BU07-18	LHS (Quartzite)	91.25686	27.10706	1580	x	x	3	x
BU07-21	LHS (Quartzite)	91.22197	27.07247	950	x	x	3	x
BU07-22	LHS (Quartzite)	91.20628	27.00844	260	x	x	3	x
BU07-24	LHS (Quartzite)	91.19019	26.95358	505	x	x	3	x
BU07-26	LHS (Quartzite)	91.22817	26.90828	975	x	x	3	x
BU07-27	LHS (Diamictite)	91.23072	26.90567	975	x	3	3	x
BU07-29	LHS (Diamictite)	91.23983	26.87803	465	x	3	3	x
BU07-33	LHS (Diamictite)	91.54794	26.93311	1710	x	3	3	x
BU07-35	LHS (Quartzite)	91.54761	26.95992	1580	x	3	3	x
BU07-36	LHS (Quartzite)	91.53083	26.97442	1785	x	x	3	x
BU07-37	LHS (Quartzite)	91.50142	27.02675	2385	x	3	3	x
BU07-42	LHS (Quartzite)	91.52089	27.08486	2165	x	x	3	x
BU07-43B	LHS (Quartzite)	91.56708	27.13450	2315	x	x	3	x
BU07-53	Gondwana Fm. (Sandstone)	91.48011	26.86572	655	x	x	3	x
BU07-54	LHS (Quartzite)	91.48028	26.87497	700	x	x	3	x
BU07-60	LHS (Quartzite)	89.39319	26.85456	366	x	x	4	x

Table S1. Continued

BU07-75	Paro Fm. (Quartzite)	89.54175	27.15200	2282	x	x	4	x
BU07-79	Paro Fm. (Quartzite)	89.57497	27.33758	2190	x	x	4	x
BU08-135	Jaishidanda Fm. (Quartzite)	89.46922	26.91692	1871	x	x	4	x
BU10-71	LHS (Quartzite)	89.20083	26.89519	1528	x	x	4	x
NBH-11	LHS (Quartzite)	91.18354	27.50625	1365	x	x	3	x
NBH-18	LHS (Quartzite)	91.52072	27.01200	1815	x	x	3	x

Notes: x: no analysis available; 1: this study; 2: [*Grujic et al.*, 2006]; 3: [*Long et al.*, 2012]; 4: [*McQuarrie et al.*, 2014].

Appendix B. Analytical procedure of apatite (U-Th)/He thermochronology

Sample preparation and He measurement was performed at Dalhousie University. Individual apatite grains were selected from apatite concentrates on the basis of size, morphology and lack of inclusions as specified by [*Farley*, 2002]. When available, five grains per sample were hand-picked using a Zeiss stereoscopic microscope at 66 x magnification under cross-polarized light to screen for fluid and solid inclusions. Selected crystals were measured and photographed in three different directions for alpha-ejection correction. Each crystal was then packed into a Pt foil envelope. Fragments from a single, large, crushed Durango apatite crystal packed in Pt envelopes served as laboratory standards and empty Pt envelopes were included for blank measurements. Crystals, Durango standards and empty Pt foils were loaded in a 25-holes stainless steel planchet and placed into the UHV extraction system behind a Supra-Sil fused silica viewport. Individual packets were heated for 5 min. at 1050°C by a defocused Quantronics model NdYAG laser operated in continuous mode at 1064 nm to extract the ^{4}He. The sample temperature was controlled by measuring the Pt temperature with a 2-color optical pyrometer, which regulated the laser output power. Each grain was then re-heated for 5 minutes at 1050 °C to check for incomplete ^{4}He extraction and potential presence of undetected zircon micro-inclusions. If the percentage of re-extraction exceeded 0.15%, the grain was discarded. The ^{4}He abundance was measured by isotope dilution on a Pfeiffer Prisma QMS200 quadrupole mass 160 spectrometer using a calibrated ^{3}He spike. The ^{4}He extracted from the samples was purified before admission to the mass spectrometer by retention of condensable gases in a CTI Cryogenics liquid He cryogenic cold trap operated at 37 °K. U, Th and Sm measurement were performed at the Geology Department of ETH, Zürich. Apatite and platinum packages were opened and transferred to vials, where ^{233}U, ^{236}U, ^{230}Th, ^{149}Sm and ^{147}Sm standards were added. Apatites were digested in 5% HNO_3 for 24 hours on a hotplate at 90 ºC and U, Th and Sm concentration were measured using a quadrupole ICP-MS.

Appendix C. Analytical procedure of zircon (U-Th)/He thermochronology

Samples were processed at the Department of Geosciences at the University of Arizona together with the samples from [*Long et al.*, 2012] and [*McQuarrie et al.*, 2014]*. For a detailed description of the analytical procedure, see Supplementary Material by *Long et al.*, [2012].

Table S2. Zircon (U-Th)/He published data

Samples	Corrected Age (Ma)	Mean Age (Ma)	Error (Ma)	Samples	Corrected age (Ma)	Mean Age (Ma)	Error (Ma)
BH-38_z1	5.23	**5.52**	**0.28**	BU07-26-z1	11.07	**10.09**	**0.61**
BH-38_z2	5.80			BU07-26-z2	10.26		
				BU07-26-z3	8.95		
BH-57_z1	6.76	**7.30**	**0.27**	BU07-27-z1	10.48	**9.10**	**0.79**
BH-57_z2	7.51			BU07-27-z2	7.74		
BH-57_z3	7.63			BU07-27-z3	9.06		
BH-78_z1	6.84	**7.01**	**0.11**	BU07-29-z1	8.69	**7.92**	**0.85**
BH-78_z2	6.95			BU07-29-z2	8.86		
BH-78_z3	7.23			BU07-29-z3	6.22		
BH-101-z1	8.48	**8.38**	**0.18**	BU07-33-z1	10.55	**11.12**	**0.30**
BH-101-z2	8.02			BU07-33-z2	11.25		
BH-101-z3	8.64			BU07-33-z3	11.57		
BH-342_z1	8.70	**8.59**	**0.31**	BU07-35-z1	11.42	**10.91**	**0.81**
BH-342_z2	9.06			BU07-35-z2	11.99		
BH-342-z3	8.01			BU07-35-z3	9.32		
BH-378_z1	3.90	**4.19**	**0.40**	BU07-36-z1	11.80	**11.00**	**0.51**
BH-378_z2	5.00			BU07-36-z2	11.18		
BH-378_z3	3.67			BU07-36-z3	10.03		
BU07-6-z1	5.84	**5.65**	**0.12**	BU07-37-z1	11.10	**11.25**	**0.18**
BU07-6-z2	5.68			BU07-37-z2	11.04		
BU07-6-z3	5.43			BU07-37-z3	11.60		
BU07-9-z1	6.80	**6.71**	**0.04**	BU07-42-z1	9.98	**9.54**	**0.64**
BU07-9-z2	6.69			BU07-42-z2	8.27		
BU07-9-z3	6.64			BU07-42-z3	10.37		
BU07-11-z1	7.14	**7.50**	**0.74**	BU07-43B-z1	9.60	**9.43**	**0.47**
BU07-11-z2	8.93			BU07-43B-z2	10.15		
BU07-11-z3	6.42			BU07-43B-z3	8.55		
BU07-12-z1	8.87	**8.65**	**0.14**	BU07-53-z1	10.22	**8.65**	**0.78**
BU07-12-z2	8.39			BU07-53-z2	7.88		
BU07-12-z3	8.68			BU07-53-z3	7.86		
BU07-13-z1	11.52	**10.63**	**1.28**	BU07-54-z1	7.78	**7.61**	**0.10**
BU07-13-z2	12.27			BU07-54-z2	7.43		
BU07-13-z3	8.11			BU07-54-z3	7.62		
BU07-14-z1	9.51	**9.68**	**0.30**	BU07-55-z2	6.94	**11.07**	**4.13**
BU07-14-z2	9.26			BU07-55-z3	15.21		
BU07-14-z3	10.27						
BU07-18-z1	9.95	**9.69**	**0.15**	NBH-11-z1	7.03	**6.57**	**0.45**
BU07-18-z2	9.69			NBH-11-z2	6.12		
BU07-18-z3	9.43						

Table S2. Continued

BU07-21-z1	9.36	**8.74**	**0.51**	NBH-18-z2	11.62	**11.60**	**0.01**
BU07-21-z2	7.73			NBH-18-z3	11.59		
BU07-21-z3	9.12						
BU07-22-z1	9.55	**9.86**	**0.20**	BHF-01a-z1	7.36	**6.50**	**0.86 ***
BU07-21-z2	9.79			BHF-01a-z3	5.63		
BU07-21-z3	10.24						
BU07-24-z1	10.04	**8.81**	**1.22**	BHF-04-z1	9.13	**9.74**	**1.07 ***
BU07-24-z2	7.59			BHF-04-z2	8.27		
				BHF-04-z3	11.82		
BHF-05-z1	8.15	**7.74**	**0.44 ***	BH-424-z1	9.13	**7.18**	**1.01 ***
BHF-05-z2	6.85			BH-424-z2	5.75		
BHF-05-z3	8.21			BH-424-z3	6.65		
BHF-07-z1	7.77	**7.70**	**0.07 ***	BH-432-z1	7.46	**6.92**	**0.28 ***
BHF-07-z2	7.62			BH-432-z2	6.51		
				BH-432-z3	6.78		
BH-109-z1	6.45	**6.50**	**0.39 ***	BU07-60-z1	3.36	**3.36**	**0.05 ***
BH-109-z2	5.83						
BH-109-z3	7.21						
BH-406-z1	6.15	**6.15**	**0.08 ***	BU07-75-z1	8.20	**8.04**	**0.19 ***
				BU07-75-z3	8.26		
				BU07-75-z4	7.66		
BH-411-z1	6.40	**6.60**	**0.37 ***	BU07-79-z2	5.94	**6.60**	**0.37 ***
BH-411-z2	6.33			BU07-79-z3	7.25		
BH-411b-z3	6.54			BU07-79-z5	6.62		
BH-411b-z4	8.36						
BH-411b-z5	6.39						
BH-411b-z6	5.59						
BH-413-z1	6.63	**6.95**	**0.27 ***	BU08-135-z1	8.60	**9.12**	**0.26 ***
BH-413-z2	7.50			BU08-135-z2	9.30		
BH-413b-z3	6.71			BU08-135-z3	9.47		
BH-415-z1	6.63	**6.11**	**0.33 ***	BU10-71-z1	8.58	**8.58**	**0.12 ***
BH-415-z2	5.49						
BH-415-z3	6.20						

Published Zircon (U-Th)/He data used in the models. Errors were recalculated using a standard error approach on single-grain ages where the standard deviation of the age population is divided by the square root of the number of data. This error takes into account the dispersion of the single-grain ages, which is commonly larger than analytical errors.

Appendix D. Analytical procedure of apatite fission-track thermochronology

AFT samples were processed and analysed at Stanford University and Dalhousie University; Apatite aliquots were mounted in araldite epoxy on glass slides, ground and polished to expose internal grain surfaces, then etched for 20 s in 5.5M HNO_3 at 21 °C to reveal spontaneous fission tracks. All mounts were prepared using the external-detector method [*Hurford and Green*, 1983]. Samples and CN5 glass standards were irradiated with thermal neutrons in the Oregon State University reactor. After irradiation, the low-U muscovite detectors that covered apatite grain mounts and glass dosimeter were etched in 40% HF for 45 min at 21 °C to reveal induced fission tracks. Samples were analysed using a Kinetek computer-controlled stage driven by the FTStage software [*Dumitru*, 1993] attached to a Zeiss Axioplan microscope. Dry counting was done at a magnification of x1000 and between 7 to 30 grains per sample were analysed. Fission track ages were calculated using a weighted mean Zeta calibration factor [*Hurford and Green*, 1983] based on IUGS ages standards (Durango, Fish Canyon and Mount Dromedary apatites) [*Hurford*, 1990; *Miller et al.*, 1985]. Based on 23 analyses, the ζ for the operator (I. Coutand) is 369.8 ± 4.8.

Appendix E. Analytical procedure of zircon fission-track thermochronology

Samples were processed at Université Joseph Fourier (Grenoble, France). For fission-track analysis zircons were mounted in Teflon® sheets, polished, and etched at 228°C in a laboratory oven in a eutectic NaOH-KOH melt for up to 40 hours. The etching progress and the quality of the etched tracks were controlled between subsequent etching steps to obtain countable fission-track for the majority of the grains (e.g. [*Bernet et al.*, 2004; *Naeser et al.*, 1987]).

All samples were covered with mica sheets as external detectors and send for neutron irradiation in 2007 at the well-thermalized ORPHEE reactor in Gif-sur-Yvette, France. The samples were irradiated together with IRM540R glass standards and Fish Canyon Tuff and Buluk Tuff age standards. After irradiation the mica sheets of all samples and standards were etched for 18 minutes at 21°C in 48% HF. The samples and standards were counted dry at 1250x magnification, using an Olympus BH2 optical microscope and the FTStage 4.04 system of Trevor Dimitru. ZFT ages were calculated using the BINOMFIT software of Brandon (as described in *Ehlers*, [2005]).

Appendix F – Implementation of topographic advection

Topographic steady state is often assumed in 3D thermokinematic models, but this assumption geometrically limits the allowable fault geometries and resulting particle exhumation pathways. The main restriction is that the dip angle of thrust faults must not be shallower than the lowest surface slope in the same direction as the fault dip (Figure S1). In such cases, particles may not be exhumed along pathways that travel exclusively beneath the surface, but instead may track above the surface (Figure S1a). Although these particle pathways are clearly unrealistic, the particle cooling history may be interpolated in the numerical model during periods of cooling while outside (above) the model volume. The result is a synthetic cooling history that does not correspond to a geologically possible scenario, but this cooling history is still viable for cooling age prediction potentially masking the problem. This issue can be even more dangerous when inverting cooling age data as performed here, because individual model results are often not spot-checked to ensure the geometric parameters from the inversion are compatible with the model topography. In convergent orogens, the geometric limitation from the model topography and fault geometry can be avoided by altering the steady-state topography assumption to include lateral advection of the topography at a horizontal velocity equal to that of the fault segments with a shallow dip (Figure S1b; e.g. *Herman et al.,* 2007; *Whipp et al.,* 2009). In this case, the topography does not change with time, but because it is moving with a horizontal velocity equal to that of material in the hanging wall, rock exhumation pathways will differ with respect to the topography. In particular, particle pathways will project approximately vertically down from the surface sample locations. Thus, they will be compatible with nearly any model topography and cooling during rock exhumation will occur entirely within the model volume. This relationship between the sample exhumation trajectories and the surface topography is most easily seen in the reference frame of the topography (Figure S1c). In this reference frame, particle trajectories are vertical and faults in the model are laterally advected at a velocity equal to the horizontal advection velocity of the topography, but opposite in direction (Figure S1c). Because advection of the topography itself can be problematic in numerical models, we have opted to utilize this fixed-topography reference frame in the implementation of horizontal landscape advection in Pecube.

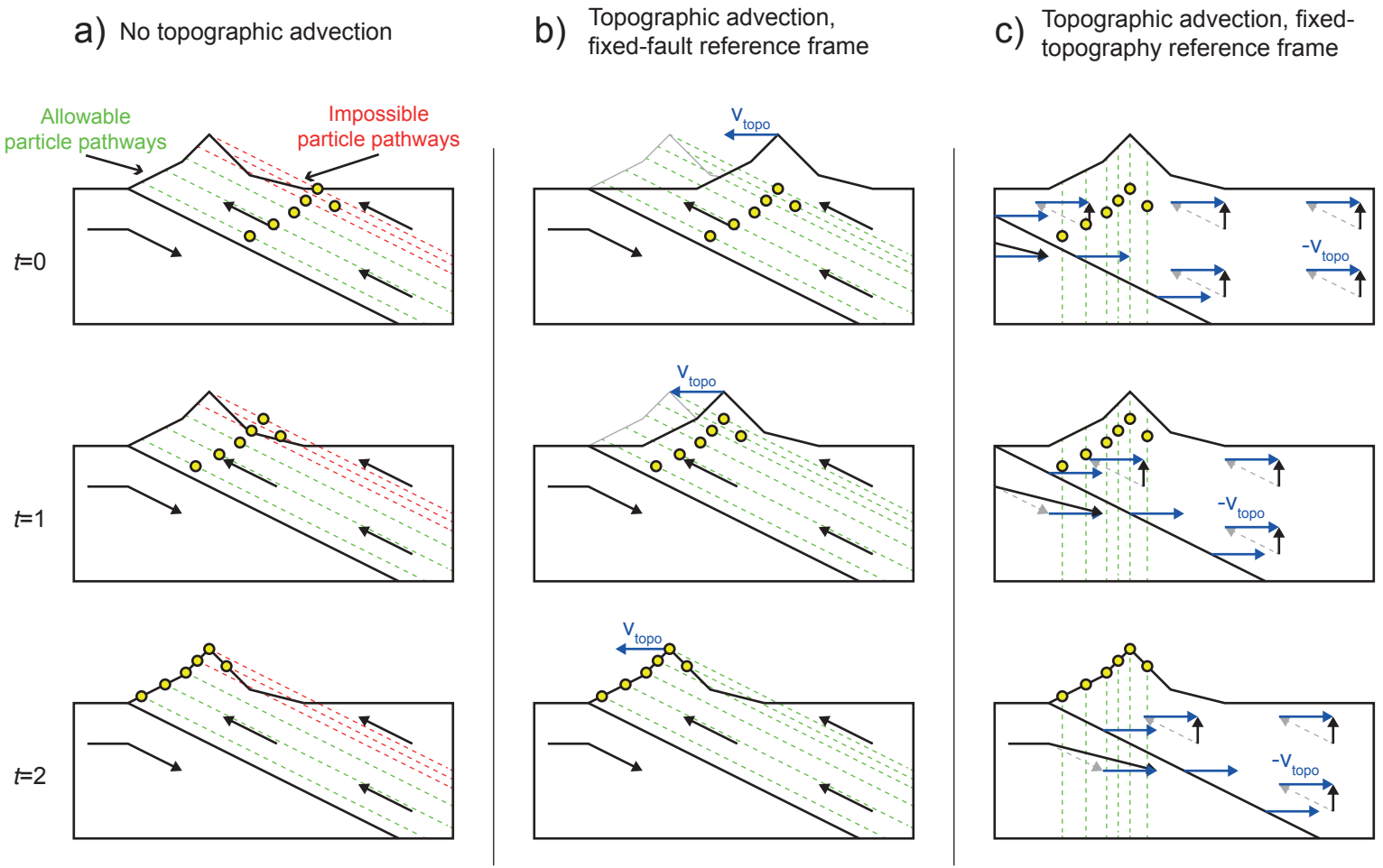

Figure S1. Schematic diagram of the time evolution of topography with and without topographic advection in a convergent orogen. Example rock samples (yellow circles) are shown for three time periods during their exhumation to the surface from time t=0 to t=2. Geometrically viable exhumation pathways (green lines) occur when particle exhumation pathways do not travel outside the hanging wall. Pathways that exit and re-enter the hanging wall are not geologically possible (red lines). a) In a scenario with no topographic advection, the surface topography and fault geometry/kinematics result in impossible particle trajectories for points near the mountain peak. b) Advection of the topography at a velocity equal to the horizontal component of hanging wall motion (v_{topo}) results in vertical exhumation pathways with respect to the topography and resolves this geometric limitation. c) Advection of the faults and orogen at velocity $-v_{topo}$ is equivalent to scenario b), but with the topography fixed in space.

Appendix G - Correlation matrices between the free parameters

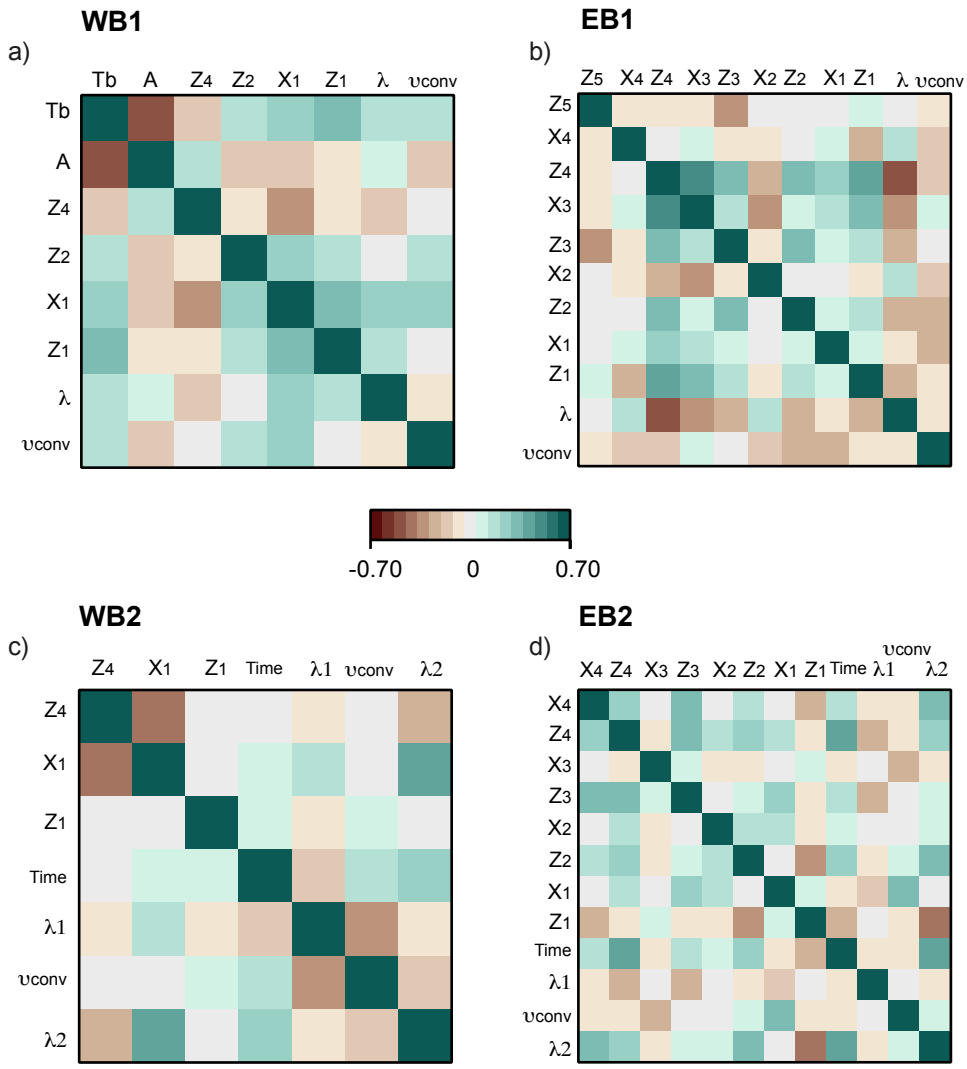

Figure S2. Correlation matrices between the different free parameters calculated for each inversion from the neighbourhood algorithm [*Sambridge,* 1999]. Each raw and column represents a free parameter. Each square represents the correlation (or anti-correlation) between two parameters. The closer the value to -0.7 (0.7), the larger the (anti)correlation. A value equal to 0 indicates the absence of trade-off between the two parameters. Parameters are labelled as in Table 6.

References

Bernet, M., M. T. Brandon, J. I. Garver, and B. Molitor (2004), Downstream Changes of Alpine Zircon Fission-Track Ages in the Rhone and Rhine Rivers, *Journal of Sedimentary Research*, *74*(1), 82-94.

Dumitru, T. A. (1993), A new computer-automated microscope stage system for fission track analysis, *Nuclear Tracks and Radiation Measurements*, *21*, 575-580.

Ehlers, T. A. (2005), Crustal thermal processes and the interpretation of thermochronometer data, *Reviews in Mineralogy and Geochemistry*, *58*(1), 315-350.

Farley, K. A. (2002), (U-Th)/He dating: Techniques, calibrations, and applications, *Reviews in Mineralogy and Geochemistry*, *47*(1), 819-844.

Grujic, D., I. Coutand, B. Bookhagen, S. Bonnet, A. Blythe, and C. Duncan (2006), Climatic forcing of erosion, landscape, and tectonics in the Bhutan Himalayas, *Geology*, *34*(10), 801-804, doi:10.1130/G22648.1.

Herman, F., J. Braun, and W. J. Dunlap (2007), Tectonomorphic scenarios in the Southern Alps of New Zealand, *Journal of Geophysical Research*, *112*, B04201, doi:10.1029/2004JB003472.

Hurford, A. J. (1990), Standardization of fission-track dating calibration: recommendation by the Fission Track Working Group of the I.U.G.S. Subcommission on geochronology, *Chemical Geology*, *80*, 171-178.

Hurford, A. J., and P. F. Green (1983), The zeta age calibration of fission-track dating, *Isotope Geoscience*, *1*, 285-317.

Long, S. P., N. McQuarrie, T. Tobgay, I. Coutand, F. J. Cooper, P. W. Reiners, J.-A. Wartho, and K. V. Hodges (2012), Variable shortening rates in the eastern Himalayan thrust belt, Bhutan: Insights from multiple thermochronologic and geochronologic data sets tied to kinematic reconstructions, *Tectonics*, *31*(5), TC5004.

McQuarrie, N., T. Tobgay, S. P. Long, P. W. Reiners, and M. A. Cosca (2014), Variable exhumation rates and variable displacement rates: documenting a recent slowing of Himalayan shortening in western Bhutan, *Earth and Planetary Sciences Letters*, v. 386, p. 161-174, doi.org/10.1016/j.epsl.2013.10.045.

Miller, D. S., I. R. Duddy, P. F. Green, A. J. Hurford, and C. W. Naeser (1985), Results of interlaboratory comparison of fission-track age standards, *Nuclear Tracks and Radiation Measurements*, *10*, 381-391.

Naeser, N. D., P. K. Zeitler, C. W. Naeser, and P. F. Cerveny (1987), Provenance studies by fission track dating — etching and counting procedures, *Nuclear Tracks and Radiation Measurements*, *13*, 121-126.

Sambridge, M. (1999), Geophysical inversion with a neighbourhood algorithm—II. Appraising the ensemble, *138*(3), 727-746.

Whipp, D. M., T. A. Ehlers, J. Braun, and C. D. Spath (2009), Effects of exhumation kinematics and topographic evolution on detrital thermochronometer data, *Journal of Geophysical Research*, *114*, F04021, doi:10.1029/2008JF001195.